DEVELOPMENT AND SIMULATION-BASED VALIDATION OF PRACTICAL METHODS FOR ESTIMATING WHOLE-HEART BLOOD-FLOW USING PERFUSION TRACERS AND A DUAL CAMERA SPECT SYSTEM

by
Jakir Hossain

A dissertation submitted to Johns Hopkins University in conformity with the requirements for the degree of Doctor of Philosophy

Baltimore, Maryland

February, 2017

ABSTRACT

Dynamic changes in tracer uptake in the heart may be useful as early predictors of cardiovascular disease or heart failure [1]. Dynamic imaging can provide additional information to aid in diagnosis. Measuring the ratio of blood flow at stress (maximum flow) and rest (normal flow) can provide quantitative information about presence of either focal defects or microvessel disease. Knowing the state of microvasculature could provide an early indicator of cardiovascular disease before blockages of large arteries develop. Dynamic SPECT imaging has been proposed as a means to measure the kinetics of a tracer, and the resulting kinetic rate parameters represent underlying absolute physiological measures such as myocardial blood flow.

However, dynamic myocardial perfusion SPECT is complicated by a number of factors. First, SPECT acquires only small number (typically 2) of projection views of the patient at a time. Thus, dynamic SPECT must use fast rotation or complicated reconstruction methods that model the change of tracer distribution during acquisition. These reconstruction methods are complicated and computationally intensive, so the full physics is often not implemented. Thus the activity distribution estimates are degraded by a number of factors, resulting in the potential for biased kinetic parameters. In addition, the noise levels in SPECT images are high and voxel values are likely not estimable, in the sense that unbiased estimators do not exist, due to the ill-posed nature of the SPECT reconstruction problem. Thus, dynamic images are likely to be very noisy and regularization is required.

We propose a new approach to Dynamic SPECT based on the previously-developed QPlanar (Quantitative Planar) method for estimating values of activities in VOIs from a pair of projections. This allows estimating the activity in the myocardium, blood pool, and defects at each projection without requiring complicated acquisition protocols and time consuming, complex reconstructions. Kinetic analysis of these time-activity data could allow estimation of flow in a small number of VOIs in the heart from standard SPECT/CT instrumentation. In this work we performed computer simulation studies based on published literature of Thallium-201 (^{201}Tl) and ^{99m}Tc-teboroxime kinetics to validate the proposed method and to investigate several potential limitations. The results of these studies, demonstrate the potential advantages of this approach over the previous SPECT method, thus warranting it’s in vivo implementation for further validation.

ACKNOWLEDGEMENTS

There are numerous people that I need to thank for assisting me during my graduate studies at Johns Hopkins University. I would like to dedicate this thesis to my late mother, Shamsun Hafiz, my father, Hafiz Hossain and my uncle Dr. Fazle Hosain, who inspired me to pursue higher education. It’s due to their love, dedication and inspiration that I was able to be here today.

First and foremost, I would like to thank my advisor, Dr. Eric C. Frey for his patient guidance and diligent support. He has been an invaluable inspiration. He is a thoughtful advisor and a wonderful mentor. Without him, completing this thesis would not have been possible.

Secondly, I would like to thank my former advisor, Dr. Michael Jacobs for his continuous guidance, teaching, mentorship and support in pursuing my research. Without his help, I would not be at this stage of my graduate studies. I would also like to thank Dr. Yong Du for mentoring me from the start of my research, offering valuable feedback, as well as being the second reader of my thesis.

I would also like to thank Dr. Arman Rahmim for his mentorship as well as spiritual guidance during a personally challenging time in my life. His advice and encouragement helped both my research and personal growth. He continues to be a great influence in my life.

I would also like to thank Professor Trac Du Tran and Professor Jin Kang for seeing me through my PhD. completion. I also want to thank Dr. Benjamin M. W. Tsui for starting the Division of Medical Imaging Physics at Johns Hopkins University and providing an enriching environment to learn and grow. Special thanks also goes to Martin Stump for keeping the computer cluster running and helping me whenever I needed assistance.

Additionally I want to thank my supervisor, Raphe Reggie for his understanding of my research work and allowing me the flexibility to work around the time needed to continue to meet with my advisor. He provided continuous encouragement to complete my PhD at times when I was very discouraged. He provided me the flexibility to both financially support myself as well as maintain the commitment I needed to complete my research.

Many thanks to all members of the Division of Medical Imaging Physics who provided a friendly yet dedicated atmosphere. I especially want to thank Dr. George S. K. Fung, Dr. MinJae Park and Dr. Michael Ghaly for their support and valuable discussions. I would also like to thank both former and current students, Xing Rong, PhD, Xin Li, PhD, Lishui Cheng, PhD, Ahmed el Harouni, PhD, Na Song, PhD and

Andrew Rittenbach, PhD for all the memories we made together in the office, at conferences and retreats.

My sincere thanks go to my mentor, Alireza Akhbardeh, PhD, for his teaching, mentoring, and friendship. His joyful company with intelligent discussion of signal processing is something I immensely appreciated at a time when my research stalled. He is a sincere friend that I was very lucky to come across during my journey through higher education. I would also like to thank Nicolas Karakatsanis, PhD, for his advice, mentorship and teaching. He is someone I look up to for performing outstanding research. His humble and unbiased attitude is something I aspire to follow in my life when couching a junior colleague. My thanks also go to my fellow graduate student study and research partner Liheng Guo, PhD and Vishwa Parekh (PhD candidate, CS) for their input and friendship during my day to day struggle. I would like to thank Gai Yan, PhD, for his friendship and for making time to read and provide valuable feedback on my thesis. I would also like to thank Aliya Reich for reading my thesis with a close eye and providing valuable feedback.

Finally, I would like to thank my immediate friends and family for their love, care, and continuous encouragement over the years. I am very fortunate and thankful to have the support and love of my fiancée, Sarah Elizabeth Wright. She continues to show patience with my demanding work and help me live a happy and balanced life. Above all, I thank the beneficent and almighty God for His continuous presence, protection and guidance in my life.

Table of Contents

List of Tables

List of Figures

1. Introduction

1.1 Significance

Monitoring dynamic changes in tracer uptake in the heart may be useful as an early predictor of cardiovascular disease or heart failure [1]. A number of studies have reported that abnormalities in the function and structure of the coronary microcirculation occur in many clinical conditions, and, in some instances, these abnormalities may contribute to the pathogenesis of myocardial ischemia [2, 3]. Measuring the ratio of blood flow at stress and rest (whole-heart coronary flow reserve, CFR) can provide quantitative information about the presence of either focal defects or micro-vessel disease. Knowing the state of microvasculature could provide an early indicator of cardiovascular disease before blockages of large arteries develop, and may also be useful in detecting the presence of multi-vessel disease.

Flow reserve can be measured with PET using N-13 ammonia, Rb-82, or F-18 based PET flow tracers [4, 5]. PET has the advantage that it acquires full tomographic data at each time point without detector rotation. However, PET is expensive, and PET systems are not as widely available as gamma cameras. It would be clinically useful if dynamic flow reserve for the whole heart could be obtained using conventional SPECT instrumentation.

Quantification of flow using SPECT requires dynamic data acquisition and tracers, such as ^{99m}Tc-teboroxime. Ideally, these tracers accumulate in the myocardium in proportion to flow, and wash out rapidly, allowing potential measurement of coronary flow reserve (CFR) with dynamic SPECT [6]. Previous data have shown that ^{99m}Tc-teboroxime wash-in and wash-out in the left ventricular myocardium were significantly changed in response to coronary vasodilation [7]. However, ^{99m}Tc-teboroxime clears rapidly from the myocardium and has relatively high accumulation in the liver, making conventional SPECT challenging.

Dynamic studies are typically performed with either planar acquisition protocols or using SPECT acquisitions that involve multiple fast rotations [8, 9]. One of the limitations of standard planar acquisition approaches is that accurate activity quantification is difficult to achieve due to multiple overlying regions with different time activity curves (TACs) [10].

In dynamic SPECT acquisitions, there are a number of technical challenges in measuring flow reserve. Standard SPECT reconstruction methods assume time-invariant tracer distributions during acquisition of all the projection data views used for reconstruction. If the distribution changes during acquisition (e.g., due to dynamic changes in the tracer distribution), the resulting data will be inconsistent [10], giving rise to bias in estimating organ activities at each time point [11]. One way to overcome this obstacle is to acquire the data very rapidly (e.g., by rotating the gamma camera quickly). However, capturing the uptake phase for perfusion tracers requires rotation speeds that are not supported by many current commercial gamma cameras, especially given the trend away from slip-ring-based systems. New dedicated cardiac systems using non-rotating gamma cameras can also be used for dynamic SPECT acquisitions. However, these systems are not widely available.

Investigators have developed 4D dynamic SPECT reconstruction methods that model tracer dynamics in every voxel [12]. The dSPECT method [8, 13] uses the concept of fitting the TACs for each voxel directly from projections without any assumption regarding the location of the functional regions and constrains the TAC to be either strictly increasing or decreasing. This method was further refined by adding constraints to improve the smoothness of TACs [14].

A recent publication [15] proposed a conventional dynamic reconstruction method in which information from the segmentation of the functional regions from a static reconstructed image was used as a prior to construct a sparse matrix to represent the spatial distribution of the radioactive tracer. This method modeled the temporal distribution of the radioactive tracer with non-uniform B-spline basis functions.

All of the above dynamic SPECT reconstruction methods are 4D and, as a result, more computationally intensive than 3D reconstruction or even the set of 3D reconstructions at each time point. As a result, the full physics of the imaging process is often not modeled, and the activity distribution estimates are thus degraded by a number of factors, such as attenuation, scatter, and the collimator-detector response. In addition, the noise at the voxel level is very high and, due to fundamental limitations of SPECT imaging, voxel values are likely not estimable parameters in the sense that unbiased estimators of the voxel values do not exist [10].

Our proposed method simplifies the problem by estimating activity at the organ or volume-of-interest (VOI) level instead of at the voxel level. This greatly reduces the number of parameters that must be estimated, and thus allows estimation from a small number of projection views. This is clinically acceptable as it is often not of interest to know blood-flow at the voxel level, and, in many cases, knowing the global blood would provide important information.

In our case, we estimate the organ or VOI activities from a single pair of projection views that are obtained simultaneously using a dual-camera system with the cameras in cardiac acquisition mode (i.e., with the cameras at right angles to each other in a perpendicular orientation). However, unlike conventional planar quantification methods, the proposed method uses knowledge of the full 3D shape of the VOIs, an accurate model of the image formation process, and maximum-likelihood estimation techniques, allowing exact modeling of overlap of organs and compensation for physical image degrading factors. For some of the data presented in this work, a conventional slow-rotation SPECT/CT acquisition protocol is used; the requisite 3D VOIs could be estimated from conventional SPECT reconstructions or CT images. In principle, data could be acquired for all or part of the acquisition without rotation. One advantage of rotating throughout the acquisition is that the data could also be used for 4D reconstruction, with the TACs estimated by this method serving as initial estimates for the various reasons. However, we found that this slow-rotation gave rise to angular-dependent bias in estimating VOI activities. Thus in parts of the work we investigate the acquisition at a single camera position providing the optimal activity estimates. The proposed method allows estimation of regional TACs that could be used as inputs to estimate kinetic parameters of physiological interest, such as blood flow.

The method does not require extremely fast rotation in order to obtain good time resolution, as the time resolution is equal to the acquisition time at each projection. Although this method does require modeling of physics of the image detection system, the system matrix itself is very small. In particular, for each time point the projection matrix is two times the number of projection bins by the number of VOIs, which would typically be less than 10. Computing this matrix including models for attenuation, scatter, and the collimator-detector response takes less than two seconds on current computers. Since the matrix is small it can be stored in memory and the remainder of the calculations is extremely fast. The total time for estimating a typical TAC in this work was less than 3 minutes. Further, because the operations at each time point are completely independent, the TAC estimation can be trivially parallelized, further reducing the computation time by a factor equal to the number of processor cores available. The method thus provides information about dynamic tracer distribution in a small number of VOIs from standard SPECT/CT instrumentation and acquisitions in clinically feasible computation times on standard workstation computers.

To demonstrate and validate this method, we first performed a simulation study investigating the feasibility of quantifying time-activity curves for ^{99m}Tc-teboroxime using a sequence of pairs of projection views obtained from a simulated conventional SPECT acquisition. Our primary reason for choosing for ^{99m}Tc-teboroxime was that it provides outstanding characteristics for measuring coronary flow reserve. However, it is not currently commercially available. However, since ^{99m}Tc-teboroxime has been approved for human/animal studies, it could potentially be reintroduced if a market developed. In addition, the method could be applied to other tracers such as Tl-201 or one of a number of various other tracers with good flow imaging properties. Thus in this work we also validated the method for Tl-201.

1.2 Organization

This dissertation consists of a background chapter and a series of chapters based on manuscripts that have been or will be submitted to peer-viewed journals. Each chapter is largely independent and stands alone.

Chapter 2 briefly introduces nuclear medicine and the quantitative imaging methods for Dynamic SPECT. This chapter contains an introduction to Dynamic SPECT, activity estimation methods, and discussion of the nuclear medicine imaging process and kinetic tracer modeling.

Chapter 3 focuses on the quantitative planar (QPlanar) processing method applied to dynamic SPECT estimation of the time activity curve using ^{99m}Tc-teboroxime as a tracer. In that chapter, we evaluated the QPlanar method using a realistic simulation of ^{99m}Tc-teboroxime imaging. This method was then applied to estimate time activity curves (TACs) for a set of 3D VOIs directly from the projections. We evaluated the accuracy and precision of estimated TACs and studied the effects of the presence of perfusion defects that were and were not modeled in the estimation procedure.

Chapter 4 focuses on the quantitative planar (QPlanar) processing method applied to dynamic SPECT estimating time activity curve using Tl-201(^{201}Tl). In that chapter, we evaluated the QPlanar method using a realistic simulation of ^{201}Tl imaging. This method was then applied to estimate time activity curves (TACs) for a set of 3D VOIs directly from the projections. In that chapter we simulated continuous rotation acquisition protocols. That chapter further explores estimating kinetic parameters in both noisy and noise-free cases using a two-compartment model in order to access blood flow measurement.

The work presented in chapter 5 investigated real factors that were assumed ideal in chapters 3 and 4. In general, this can be called model mismatch, referring to assumptions embodied in the estimation process that are different from those actually present in the data. There are various kinds of mismatch investigated including model mismatch between the true and assumed object, in the data acquisition protocol (continuous vs. static) and in defining the VOIs. In particular, we investigated errors in defining the myocardial VOI such as the lack of a VOI containing the right ventricle, which is difficult to see in SPECT images, and errors in defining the boundaries of the left ventricle. We used static data acquisition protocols to improve the accuracy of activity estimation. In these static protocols, acquisition of all data from all time points was performed at a single fixed angular view. We chose this fixed-view approach because continuous rotation acquisition did not provide accurate estimates of TACs when various types of model mismatch were introduced in the data. Furthermore, we used a singular value decomposition (SVD) analysis based matrix inversion method to estimate time activity curves in order to reduce the computational requirements.

Chapter 6 summarizes the results from previous chapters and discusses contributions of this work. It also describes some possible areas for future work.

2.0 Background

2.1 Coronary artery disease

Diagnostic cardiac stress testing with radionuclide imaging is conducted in the United States yearly on approximately 10 million patients [16, 17]. There are also a significant number of patients who develop coronary artery disease (CAD) over their life time. Heart disease cause approximately 1 out of every 7 deaths in the United States in 2011 [18]. Thus improving radionuclide imaging and thus diagnosis of coronary artery disease is an important goal.

One cause of CAD is the damaged coronary arteries of the major blood vessels supplying the heart with blood, oxygen and nutrients. Cholesterol-containing deposits or plaques in the arteries are one culprit responsible for this disease. The build-up of plaque over time narrows the coronary arteries. As a result of this, blood flow is decreased to the heart leading to chest pain and shortness of breath etc. Furthermore, a complete blockage, thought to result in some instances from ruptured plaques, can cause a fatal heart attack.

Coronary flow reserve (CFR) is defined as the ratio of coronary flow under maximal drug-induced hyperemia (stress) to base line (rest) flow [19]. Whole-heart coronary CFR may be useful as an early predictor of cardiovascular disease or heart failure [20]. Measuring CFR is an important indicator of the physiologic significance of coronary stenosis and other pathophysiologic conditions [21].

CFR may allow early detection of arteriosclerosis both regionally and globally. Furthermore, CFR is an important physiologic parameter for detection and management of ischemic heart disease [19].

The relationship between coronary artery stenosis and the degree of impairment of myocardial blood flow has been shown to be inversely proportional [1]. Uren and colleagues reported that flow progressively decreases during hyperemia or stress when the degree of stenosis is 40%, and remained constant when the degree of stenosis approached 80% or greater regardless of the severity of coronary stenosis during rest.

To assess relative regional CFR, routine clinical SPECT imaging is sufficient [22] as it measures only relative blood flow. As a result, true quantitation of CFR has been limited to other modalities such as magnetic resonance imaging and PET. In these cases, the regional CFR is computed using the stress/rest ratio of flows calculated using quantitative compartmental analysis. Dynamic SPECT has also been shown to be effective for measuring relative CFR [23].

2.2 Perfusion defect

A stenosis is a condition where the arterial lumen becomes narrow due to plaque buildup resulting from factors such as aging, life style choices and diseases. Normal arteries will vasodilate more than a stenosed artery under conditions of hyperemia, increasing organ blood flow. This is the basis of perfusion imaging. The differential uptake of radiotracer between areas supplied by normal arteries and that supplied by stenosed arteries is the concept underlying rest-stress perfusion imaging. Knowledge of regional cardiac perfusion is essential for the control and management of coronary artery disease. Positron Emission Tomography (PET) is arguably the best noninvasive modality to evaluate myocardial perfusion [24]. However, PET suffers from poor availability [25] and high cost. Single Photon Emission Computed Tomography (SPECT) on the other hand, is widely available. A static imaging protocol is typically used in clinical cardiac SPECT perfusion studies, where projections are acquired at a single time point when the tracer kinetics is assumed not to be changing rapidly.

Clinical myocardial perfusion studies normally involve static imaging protocols, in the sense that the images are acquired at a single point in time when the tracer distribution is changing slowly and reflects perfusion status.. Many different SPECT tracers have been investigated for studying perfusion. ^{99m}Tc-Teboroxime and ^{201}Tl are a widely used tracer in clinical studies for evaluating myocardial perfusion as well as myocardial viability. The static ^{99m}Tc-Teboroxime and ^{201}T1 images, wherein a single three-dimensional image is obtained, are qualitative in nature and do not provide absolute quantification of myocardial blood flow.

Dynamic myocardial SPECT could potentially be used in myocardial perfusion imaging to obtain functional images showing myocardial blood flow. Dynamic SPECT is the acquisition and reconstruction of a series images over time. These dynamics images can be analyzed to estimate global blood flow. Dynamic SPECT can be performed at both rest and stress, though stress protocols are practically challenging. Dynamic cardiac SPECT imaging with tracers like thallium-201 chloride [26] and ^{99m}Tc-Teboroxime [27] could be used to quantitatively assess perfusion in myocardial tissue.

2.3 Principles of Tracer Kinetic Modeling

In dynamic SPECT the main goal is to obtain parameters of kinetic models that represent the underlying physiology. In dynamic SPECT, a acquired time-series of projection images are used to estimate a time-series of 3D activity distributions. Extracting activities from organ volumes-of-interest (VOIs) produces a time activity curve (TAC) for each organ. This represents the kinetics of the regions of the corresponding region, e.g. myocardium, blood pool, liver etc. These TACs are then analyzed using kinetic models to estimate kinetic parameters. This section describes these models and the methods used to estimate the kinetic parameters.

Dynamic SPECT enables the radiotracer concentration to be measured as a function of time. The variation over time can be modeled using tracer kinetic modeling. It is possible to construct mathematical models with a set of one or more parameters that can be fit to explain the observed time-activity curves. Model parameters can be, in some, cases related directly to physiological or biological quantities. The mathematical models that describe the time-varying distribution of radiopharmaceuticals in the body are known as tracer kinetic models. Zierler [28] developed model equations formulated to estimate flow using tracers for both wash-in and wash-out rates describing the time-varying distribution of radiopharmaceuticals.

In the model equations, the concentration of the tracer in a tissue is considered to be dependent on the concentration of the tracer in the blood or plasma and the physiology of the organ. However, poor spatial and temporal resolution as well as the high statistical noise in the data may produce unreliable results with these models. Thus estimation of model parameters requires taking into account noise and various non-idealities in the data.

Most PET and SPECT dynamic imaging, the kinetics of the tracer is typically modeled using compartmental models. Compartmental models represent a tradeoff between the complexity of distributed and stochastic models [29]. A compartmental model defines a relationship between measured data and physiological parameters involving one or more compartments (i.e., organs) that define the kinetics of the tracer. A compartmental model is comprised of a set of compartments connected by an arrow to abstractly show inflows and outflows of materials. In the model the tracer and its metabolites can flow from one compartment to another.

The following assumptions are made in a compartmental model: (1), each compartment is well mixed; (2), the underlying physiological process is in a steady state; and (3) the amount of tracer is negligible with respect to the natural biological substrate [30]. In this work, a two-compartment model was used. This is because kinetics of the tracer could be approximated by exchange of the radiotracer between the blood and myocardium. Here, the movement of the tracer from the blood to the tissue reflects the local blood flow. The rate constants can thus be used to quantitatively estimate physiological parameters such as blood flow.

Figure 2-1, shows a two-compartment model consisting of a blood compartment and a tissue compartment. An essential input for the estimation of kinetic rate parameters is the blood input function. This can be obtained from tracer concentration measurement in blood input function. The blood flow depends on the flux of the tracer into the tissue compartment and the rate of transport of the tracer from the capillaries into the tissue. The myocardial blood flow is defined as the volume of blood passing through a given mass of tissue (i.e., the myocardium) per unit time (ml/min/g).

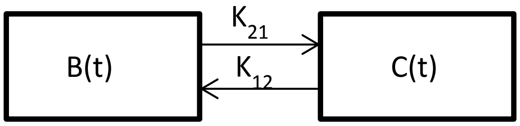

Figure 2- 1: Block diagram two-compartment model.

Fick's principle is the starting point for the computation of myocardial blood flow in a two-compartment model. It states that the net flux, J, of the tracer into or out of the tissue is given by:

$$J = J_{in} - J_{out} = FC_a - FC_v, \tag{2.1}$$

where, J_{in} is the total flux into the tissue and J_{out} is the total flux out of the tissue. The influx, J_{in}, is the product of the blood flow (F) and arterial concentration (C_a), and the outflux, J_{out}, is the product of the blood flow and venous concentration (C_v).

The extraction fraction, *E,* is the fraction of the tracer that exits the blood and enters the tissue.

$$E = \frac{(C_a - C_v)}{C_a}. \tag{2.2}$$

From eq. (2.1) and (2.2),

$$J = F * E * C_a. \tag{2.3}$$

In eq. 2.3, the product of blood flow *F* and the extraction fraction *E* is defined as the rate constant *k.* Rewriting eq. 2.3 and substituting k for F*E gives

$$J = (F.E)C_a = k * C_a. \tag{2.4}$$

The extraction of the tracer was further modeled by Kety [31], Renkin [32] and Crone [33] using a cylindrical model as follows:

$$E = 1 - e^{\frac{-PS}{F}}, \tag{2.5}$$

where, *P* is the permeability of the tracer and *S* is the surface area per gram of the tissue. In the case of highly permeable tracers, the product *PS,* referred to as the permeability surface-area product, is much greater than the flow, thus making *E* =1. In this case that the rate constant, k_{12} is equal to the blood flow.

$$\therefore k_{21} = F. \tag{2.6}$$

Solving the compartment model determines the exact relationship between the tracer concentrations and the rate constants. In case of a two-compartment model, the net flux of the tracer into the tissue compartment can also be defined as the time rate of change of concentration, $\frac{dC(t)}{dt}$, in the tissue.

Using Equation (2.5), we can compute the rate of change of the concentration in the tissue in the case of two-compartment model as:

$$\frac{dC(t)}{dt} = k_{21}B(t) - k_{12}C(t), \tag{2.7}$$

where, $B(t)$ is the tracer concentration in the blood and k_{21} is he wash-in and k_{12} is the wash-out rate parameters. After solving Equation (2.7) for tissue concentration $C(t)$, assuming that at $t = 0$, $B(t) = 0$ and $C(t) = 0$, the following equation is be obtained:

$$C(t) = B(t) \otimes k_{21}e^{-k_{12}(t)}, \tag{2.8}$$

where, $\otimes$ is the symbol of convolution operation.

From eq. 2.8, the tissue activity jumps from 0 to a level of K_{21} B(t) and then drops towards zero exponentially with a rate k_{12} per unit time or a half-life of $0.693/k_{12}$. The tissue time-activity curve, $C(t)$, can be obtained from the image data. For example, using a VOI over the tissue of interest and the QPlanar method to estimate the TAC in the organ from the time series of projections.

B(t) can either be obtained either by arterial sampling of blood or from image-derived time-activity curves in VOIs placed over a volume in the image containing only blood, such as in the aorta or the cardiac chamber. Once the tissue and blood time activity curves are obtained, they can be used to estimate k_{21} and k_{12}. This parameter estimation procedure is an inverse problem where the kinetic rate parameters are estimated by fitting the measured tissue time-activity curve to the model.

There are many methods available for estimating the kinetic rate parameters. However, many considerations such as sampling rate and duration and statistical quality of the measurements are important for successfully estimating the parameters. In this work we used a nonlinear least squares method for parameter estimation [34]. Non-linear least-squares methods are used to obtain estimates of parameters fits by minimizing the least squares objective function expressed as

$$\sum_{i=1}^{N}(C_i - C(T_i))^2, \tag{2.9}$$

where, i is the index of the measurements over time, C_i at time point T_i is the modeled uptake and $C(T_i)$ is the measured tracer uptake at time T_i. These represent maximum likelihood solutions to the parameter estimation problem under the assumption that the TAC data is normally distributed.

There are uncertainties with the measured activity measurements due to quantum noise. To account for this in the parameter estimation process it is common to weight the residual terms by a weighting factor W_i, which is typically the inverse of the variance in the measurements at time T_i. To account for the variance of the measurements from one scan to next, a weighting factor W_i used in the minimization expression [35].

$$\arg\ \min\ \{\sum_{i=1}^{N} W_i (C_i - C(T_i))^2\}. \tag{2.10}$$

A Matlab implementation of the Levenberg-Marquardt algorithm [36, 37] was used to estimate both K_{21} and $K_{12.}$ The Levenberg-Marquardt method uses a search direction that is a cross between the Gauss-Newton direction and the steepest descent direction.

2.4 Myocardial Perfusion SPECT

Presently, myocardial perfusion imaging with SPECT, i.e., myocardial perfusion SPECT (MPS), is the most widely [38] employed noninvasive method for diagnosis of patients with known or suspected coronary artery disease. This method provides a practical, inexpensive and noninvasive measure of myocardial perfusion. Thus, SPECT's three-dimensional (3D) visualization of tracer distributions in the body provides a method for diagnosis of coronary artery disease. One problem with the current method of interpreting MPS is that it is visual and qualitative in nature. However, the current method does provides some quantitative information about quantitative uptake, But this information is relative rather than absolute in nature.

Quantifying the changes in flow from rest to stress requires absolute flow at rest and stress. One way to obtain this is to take advantage of the dynamic tracer behavior (i.e., wash-out and wash-in) to estimate the absolute flow. Dynamic SPECT takes advantage of changing radiotracer distribution in the body and provides absolute quantification of dynamic process in the body, potentially improving patient diagnosis in the future. Dynamic single photon emission computed tomography (SPECT) is a technique used to obtain images that reflect fundamental bio physiologic functions of perfusion and metabolism in body organs [10].

This dissertation focuses on extracting information about the changes in biodistribution of myocardial perfusion tracers over time with the ultimate goal of extracting absolute blood flow. It focuses on two MPS tracers, ^{99m}Tc-teboroxime and ^{201}Tl, due to their status as FDA approved agents and their properties in terms of measuring flow.

The following sections of this dissertation discuss specifics of SPECT system in including various hardware components, image processing algorithms, image degrading factors and compensation methods for image degrading factors.

2.4.1 Gamma Camera

Most commercially available SPECT systems are based on gamma camera. To create a tomographic image, one or more gamma cameras mounted on a rotating gantry are used to acquire projections at multiple views around the patient. A conventional gamma camera consists of a collimator, scintillation crystal, light-guide, PM tube array, positioning circuits, pulse height analyzer, and a computer, as illustrated in Figure 2-2. The basic functions of each individual component will be described below:

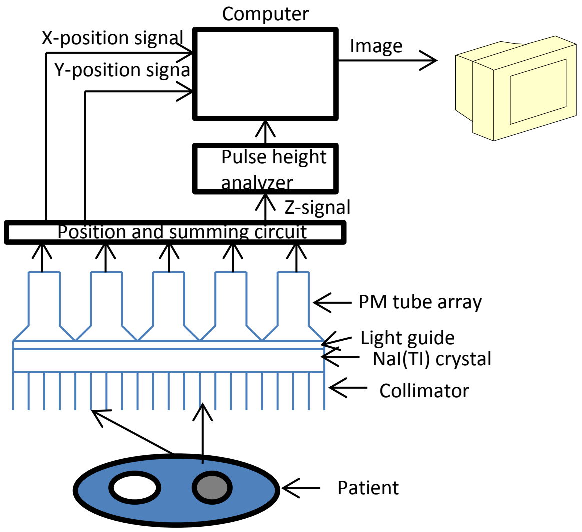

Figure 2- 2: Block diagram of individual components of gamma camera.

2.4.1.1 Collimator

An image is obtained with a gamma camera by measuring photons that exit the body, thus forming an image projection of the distribution of radioactive sources in the body. This projection of the sources onto the detector is formed by allowing only those gamma rays travelling along certain directions to reach the detector. Since gamma rays cannot be focused, a collimator is used to define a relationship between positions in the image and lines through the object. The collimators used in myocardial perfusion SPECT (MPS) systems typically have many parallel holes. Ideally, gamma rays not passing through the parallel holes are absorbed and would not contribute to the image. Gamma rays that are not absorbed by the collimator interact with the crystal and can, as described below, contribute to the image. A desirable characteristic of the collimator is to absorb the gamma rays intersecting the septa, i.e., the walls of the collimator holes. To accomplish this, collimators are made of a high Z material (e.g., Pb or W) so that photons incident on the septa have a high chance of being absorbed.

However, high-energy photons can penetrate the collimator septa and can be detected; resulting in degradation of image contrast and complicating image quantification. One solution is to use thick septa that reduce the chance of penetration through the collimator. However, this decreases the efficiency of the collimator, resulting in unacceptable levels of image noise. Various other factors besides septal thickness, primarily the desired resolution and efficiency tradeoff, which is determined by the hole length, the size and shape of the hole and collimator geometry, need to be taken into consideration in designing collimators. In this dissertation we concentrate on parallel-hole collimators. This type of collimator consists of parallel holes, which are formed by casting lead or stacking thin lead foils stamped in such a way as to create the holes. The thickness of the septa is chosen so that it reduces the probability of gamma rays penetrating through the septa to an acceptable level, often 5%.

2.4.1.2 Scintillation Crystal

Radiation from radioactive decay interacts with matter by causing ionization or excitation of atoms and molecules. As the ionized atoms and molecules relax to the ground state, energy is released. In typical materials much of this energy is dissipated as thermal energy such as molecular vibrations in a crystal or by breaking chemical bonds. However, in some materials a portion of this energy is released as visible light. These materials are called scintillators. Detectors that use scintillating crystals are called scintillation detectors. In such detectors, the number of light photons produced per incident gamma ray photon is proportional to the gamma ray's energy. Thus, the detector system measures the incident photon's energy by measuring the total number of scintillation photons. The number of scintillation photons produced for a given interaction is a random process governed by Poisson statistics. Thus, the larger the number of scintillation photons produced and collected, the more precise the estimate of the photon's incident energy. After the scintillation photons are emitted, they are collected and converted to electrical signals whose amplitude is proportional to the intensity of the scintillation light, and thus the energy deposited in the crystal. These electrical signals are used to estimate the photon’s energy and the incident position.

2.4.1.3 Photomultiplier Tube (PM tubes)

The light signal from the scintillator is not very strong, typically being comprised of several hundred photons. As a result, it is necessary to amplify this signal and to turn it into an electrical signal that can be measured. However, the electrical signal must be proportional to the number of scintillation photons. In conventional gamma cameras this is done by photomultiplier (PM) tubes. PM tubes are vacuum tubes that produce a pulse of electrical current when stimulated by very weak light signals, such as scintillation photons produced by ϒ rays in a scintillation detector. When scintillation light photons escape from the crystal, they are collected by light guides or exit windows. Light guides or exit windows are transparent and are used to seal the crystal, preventing humidity from destroying it, and match the index of refraction of the scintillator to that of the photodetectors in order to reduce internal reflections and maximize transmission of the scintillation light. The light photons are transmitted through the light guide to the PM tubes. These photons are then incident on the PM tube’s photocathode. A fraction of these incident photoelectrons exit the photocathode into the vacuum. These photoelectrons are amplified by a series of dynodes that create a field to amplify the charge signal. Preamplifiers and amplifiers attached to the outputs of the PM tubes further amplify and shape the current pulse in such a way that its height is proportional to the amplified charge signal, and thus to the number of scintillation photons incident on the PM tube.

2.4.1.4 Positioning Circuit

To form an image it is necessary to estimate the position where incident gamma rays interact with the crystal. This is done using an array of PMTs connected to positioning circuits. In a conventional Anger camera, the output current signals from PMTs are divided and summed with a weighted resistive network. This network has 4 outputs referred to as *X+*, *X-*, *Y+,* and *Y-*. Total output of the PMTs is referred to as the Z signal, which is the sum of *X+*, *X-*, *Y+*, and *Y-*, and is proportional to the total charge created in all the PMTs, and thus to the energy deposited in the crystal. The resistors in the network are chosen so that the interaction positions of the photons can be calculated using the simple relationships below.

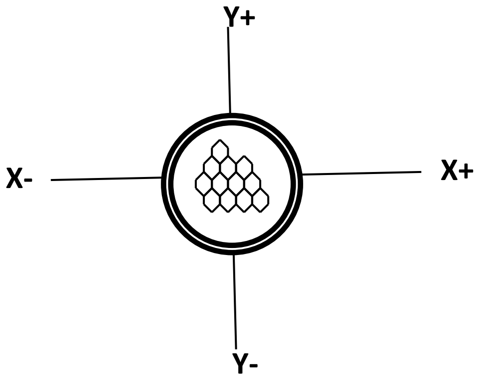

Figure 2- 3: Layout of photomultiplier on the face of gamma camera

To obtain X-position and Y-position signals, the *X+, X-, Y+* and *Y-* are combined. The X-position is given by difference in the *X+* and *X-* signals, divided by total Z signal.

$$X = \frac{X^{+} - X^{-}}{Z}. \tag{2.13}$$

Similarly, the Y-position can be obtained as follows:

$$Y = \frac{Y^{+} - Y^{-}}{Z}. \tag{2.14}$$

In modern gamma cameras, the estimation of the positions, and even the shaping of the signals, is done digitally.

2.4.1.5 Pulse Height Analyzer (PHA)

As photons pass through the body and detector, they interact with the various tissues. Some of these interactions are Compton scatter events where both the direction and energy of the photon are changed. Since the direction is changed, scattered photons carry poor information about their point of emission, and inclusion of scattered photons in the image results in a loss of image contrast and quantitative accuracy. An obvious way to discriminate between scattered and unscattered photons is to use the fact that scattering results in a reduction of photon energy. A Pulse Height Analyzer (PHA) circuit is thus used in a gamma camera system to aid in rejection of scattered photons. The PHA analyzes the summed output pulse signal from the PM tube array. Since the Z signal from PM tubes is proportional to the deposited energy, the discrimination between scattered and unscattered photons is done by selecting Z signals with heights that fall into a range that represents an energy window around the energy of the emitted gamma ray.

One of the problems with using energy discrimination is that it can have problems with very high count rates. In this case, two or more gamma photons could interact with the camera at essentially the same time. The gamma camera would detect this as a single simultaneous event. Consider a situation where two separate events occur simultaneously. The total pulse height will be larger than the output from a single event and lies outside the energy window. The energy discrimination process would thus reject this simultaneous event.

However, when two photons deposit only a portion of their initial energy in the crystal (e.g., if they were scattered in the body) at the same time, it is possible for the total pulse height to still lie in the energy window. This event would thus be counted as a single event. Similarly, the position signals used to estimate the position are also the sums of the incident photon, and the estimated position of the photon is a combination of the positions of the two incident photons. This pulse-pileup phenomenon results in distortions in both the energy and position.

2.4.2 Interaction of Photons with Matter

There are four basic types of interactions in nuclear medicine when photons interact with matter. These are the photoelectric effect, Compton and coherent scattering, and pair production [39]. The photoelectric effect is an atomic absorption process in which an atom absorbs the total energy of the incident photon. During this interaction, the photon disappears and the energy absorbed is used to eject an orbital electron from the atom; the ejected electron is called a photoelectron and receives a kinetic energy, E_{pe}, equal to the difference between the incident photon energy, E_o, and the binding energy of the electron shell from which it was ejected. This can be described by the following equation for a K-shell electron ejection.

The ejected electron receives kinetic energy E_{pe}, equal to the difference between the incident photon energy E_o and the binding energy of the electron shell from which it was ejected. This can be described by the following equation for a K-shell electron ejection.

$$E_{PE} = E_o - K_B, \tag{2.15}$$

where, K_B is the binding energy for the atom from which it is ejected.

This is illustrated in Figure 2-4.

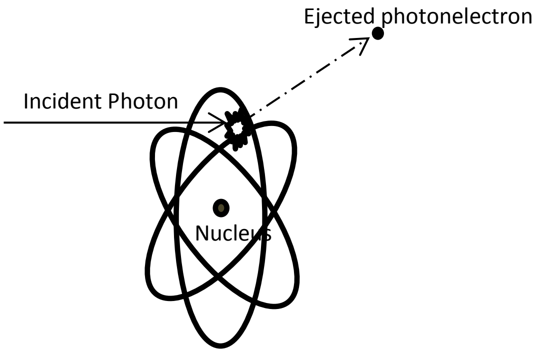

Figure 2- 4: Schematic of incident photon transferring its energy to a photoelectron and disappearing.

Compton scattering is a collision between the incident photon and a free electron. In nuclear medicine imaging, the energies of the bound electrons in atoms in the body are very small compared to the energies of gamma rays, and thus can be considered to be free electrons. In case of Compton scatter, the incident photon transfers part of its energy to the electron and changes its direction. The process is illustrated in Figure 2-5.

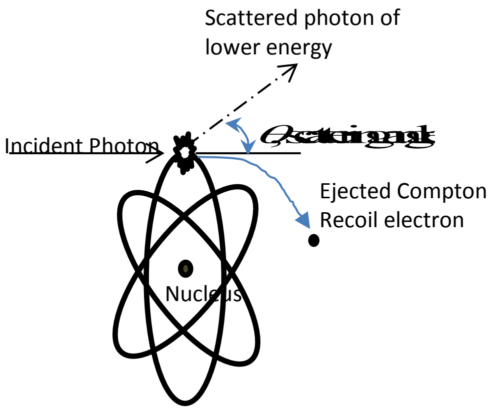

Figure 2- 5: Schematic of incident photon transferring part of its energy to a Compton recoil electron and is scattered in another direction of travel with Ѳ scattering angle

The energy of the scattered photon, E_s, is given by the Compton equation:

$$E_{sca} = \frac{E_{inc}}{[1+\frac{E_{inc}(1+\cos\theta}{m_e c^2}]}, \qquad (2.16)$$

where, E_{inc} is the energy of the incident photon, E_{sca} is the energy of scattered photon in MeV, m_e is the rest mass of electron, c is the speed of light and θ is the scattering angle.

The likelihood of photoelectric absorption and Compton scattering is a function of the incident photon's energy. For photoelectric absorption the probability is a rapidly increasing function of the atomic number; however, in Compton scatter the probability is a function of the electron density in the material and is independent of the atomic number. At low energies and for high atomic numbers photoelectric absorption is the more important interaction; at high energies and for lower atomic number materials Compton scatter tends to dominate.

2.4.3 Physical Degrading Factors for Affecting Image Quantification

Various physical processes resulting from the interaction between gamma rays and matter were described above. Gamma photons can interact in these ways with the collimator-detector system or the patient's body. The number and distribution of detected photons is thus affected by the collimator and the patient. Thus in estimating the 3D activity distribution it is necessary to take into account these effects' failure to do so results in degradations in image quality and quantitative accuracy of the activity distribution estimates. Below, are discussions of various degrading factors that affect the estimated activity distribution.

2.4.3.1 Attenuation

Photon attenuation is due to the loss of photons through interactions with the patient by absorption or scattering. As a photon passes through a thickness of an absorber material, the likelihood that it will experience an interaction depends on its energy and on the composition and thickness of the absorber. This phenomenon is referred to as photon attenuation. The effect of attenuation on the SPECT image depends on body size, the radionuclide used, and the distribution of the radioactivity in the body.

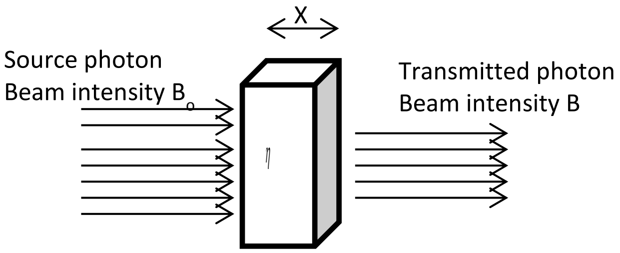

Figure 2- 6: Schematic of incident photon beam passing through an object

Consider a monoenergetic beam of photons incident on a homogeneous object with thickness *x.* Let the intensity of non-interacting photon after passing through the object be *B*. This transmitted intensity can be described by the following equation:

$$B = B_o \text{ x } e^{-\mu x}, \tag{2.17}$$

where, B_0 is the intensity of the source beam, μ is the linear attenuation coefficient and x is the thickness of the object. The linear attenuation coefficient depends on the atomic composition and density of the object and the energy of the incident beam.

2.4.3.2 Photon Scatter

Scatter causes a change in the photon’s energy and direction. The change in direction after scatter means that the photon’s direction, and thus whether it passes through a collimator whole, does not contain the same quality of information about the location of the source of the photon as for an unscattered photon. The loss of energy can be used to reject scattered photons, but is of limited use due to finite resolution of the detector. Thus some scattered photons will be detected, and the relationship between the detected intensity of a beam and the incident intensity is no longer described by eq. 2.17. Thus scatter causes degradation of both quantitative and position information carried by detected photons. One type of scatter is called the coherent scatter, and one type of coherent scatter is Rayleigh scattering. In coherent scatter the energy of the photon does not change because the scattering is with an object that has a sufficiently large mass that it can balance the change in relativistic momentum that the photon experiences when it changes direction without carrying measurable amounts of energy. Rayleigh scatter is a type of scattering interaction between a photon and bound atomic electron. In contrast to Compton scatter, the momentum and energy transferred during scatter is imparted to the entire atom rather than the electron. Due to the great mass of atom, little recoil energy is absorbed by the atom. This causes the photon to be deflected with little loss of energy. These events are illustrated in Figure 2-7. Coherent scattering is significant at relatively low energies (<< 50 keV) or for high Z material such as Pb.

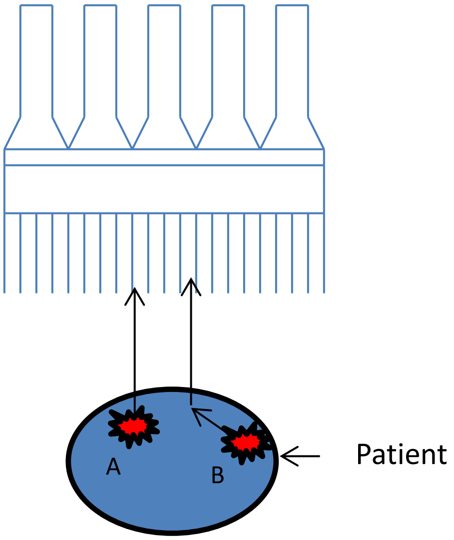

Figure 2- 7: Schematic of detecting emitted photons

2.4.3.2 Collimator Detector Response (CDR)

A well designed collimator detector system needs to have many desirable characteristics. Ideally, only photons traveling in a path parallel to the axes of the collimator holes passing through and interacting with the crystal. The second is that crystal should be able to completely absorb all incident photons at the exact position the photon intersects the face of the crystal. Unfortunately, due to mechanical and material limits, the above properties require a compromise when the parameters for the hole size and length, septal thickness and crystal thickness, etc. are selected. This leads to detection of photons incident within a small acceptance angle or incident on the septa. The collimator detector response (CDR) function (CDRF) characterizes these effects [40]. The ideal CDRF would be a delta function, but due to the effects discussed above, the real CDRFs have a degraded shape, as illustrated in Figure 2-8.

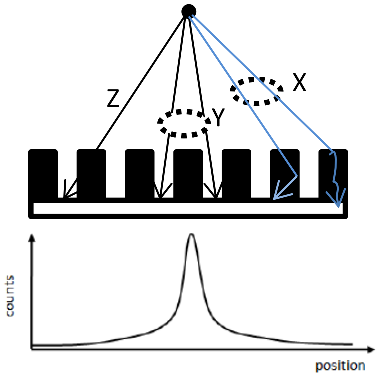

Figure 2- 8: Schematic of components of collimator detector response

Collimator detector response is the result of 4 major components: the septal penetration, septal scatter, geometric and intrinsic responses. In all cases the response function refers to the probability distribution for detecting photons emitted by a point source that pass through the collimator in various ways. The septal scatter response function (SSRF) and septal penetration response function (SPRF) describe the distribution of photons that are scattered inside or penetrate through the septa, respectively. The geometric response function (GRF) describes the distribution of photons that pass through the collimator holes without interacting with the septa. The intrinsic response function (IRF) is the response of the imaging system to a point source without collimator.

Septa are effectively opaque for low energy photons. Most photons with large incident angles are absorbed in the septa. However, for medium and high energy photons, penetration of photons through or scatter in the septa can significantly contribute to the projection images.

2.4.3.3 Partial Volume effects

Ideally the intensity of each pixel in a SPECT image would be proportional to the amount of radioactivity within the corresponding volume of tissue in the patient. However, there are errors in the estimated values of the tissue activity concentration values for small tissue volumes due to the resolution effects described above. These errors are more prevalent in areas where the activities are changing rapidly in space. The errors in the activity estimates in volumes of interest due to resolution effects is referred to as partial volume effects (PVE). There are two types of PVEs: “spill-out” and “spill-in”. “Spill-out” refers to loss of voxel image intensities from a target to the background due to finite resolution effects; “spill-in” refers to intensity in an image voxel due to activity in nearby voxels. These effects are most apparent when the Therefore, spill-in increases the activity estimate in a region of interest. When considering the magnitude of PVE for a particular volume-of-interest, its size, relative activities in surrounding regions and system resolution is important.

In SPECT, PVEs are manifested as both a loss of counts in structures smaller than 2-3 times the system FWHM (partial volume) that are surrounded by regions with lower activity concentration and an increase of counts in regions of low activity concentration relative to its surroundings. PVEs can be a dominant source of quantitative errors in for small objects, e.g., tumors. Although CDRF compensation can reduce PVEs, explicit PVE compensation may still be needed.

2.4.4 Planar Quantitation methods

Planar scintigraphic imaging using gamma cameras is widely used in routine clinical practice and research studies. This imaging method can provide quantitative and qualitative information about activity distribution. In order to accurately quantify an object's activity from planar images, compensations for the degrading factors described above are essential. The following section will discuss background information about the planar quantification in light of compensation for degrading factors discussed earlier.

2.4.4.1 Conventional Planar Processing Methods

Perhaps the major effect degrading quantification of all nuclear medicine images is attenuation. Geometric mean (GM) of counts in conjugates still the most commonly used compensation method in planar imaging [41]. This method uses the following equation to account for the effects of attenuation on a point source in an attenuating medium.

$$N = \sqrt{N_1 * N_2} = N_o e^{-\mu T/2}. \tag{2.18}$$

In eq. 2.18, N_1 and N_2 are the counts in the voxels or image that view the objects from opposing directions, N_0 is the unattenuated count rate from the source, T is the thickness of the body at the location of the source, μ is the linear attenuation coefficient, and N is the GM of the counts from the two views. Note that the GM value is independent of the source depth and depends only on object thickness. Given the object thickness, attenuation, and the GM counts it is straightforward to estimate the un-attenuated count.

However, eq. 2.18 will not be sufficient for a more complicated situation where the source is not a point source and where non-uniform attenuation is present. The effect of non-uniform attenuation can be taken into account by measuring the transmission factor using a transmission or CT scan. More complicated expressions are available for sources with finite thickness, but no completely general formulas are available. It is important to note that GM method is only valid for unscattered photons.

Since nuclear medicine images contain scatter, it is crucial to compensate for this before applying the GM method. One way to perform this is to subtract the scattered component of the projecton in from the total counts recorded in the primary energy window to get an estimate of the unscattered counts, as shown in eq. 2.19:

$$C_{prim} = C_{total} - C_{scat}. \tag{2.19}$$

The key to this method is obtaining an accurate estimate of the scatter component. Two common methods for obtaining this estimate are the Dual-energy window (DEW) and triple-energy window (TEW) methods [42-44]. The DEW method consists of subtracting a fraction of the image or projection obtained in a lower energy window from an upper energy window. However, this assumes a spatially constant proportionality between the counts in the lower window and scatter counts in the upper window. Also, the choice of the proportionality constant requires a calibration procedure.

The TEW method uses three energy windows: a photopeak window and two scatter windows. The photopeak window is normally centered over the photo peak energy and two scatter windows are on each side and adjacent to the photopeak window. A trapezoidal approximation, eq. 2.20, is used to estimate the scattered counts in the main window.

$$C_{scat} = (\frac{C_{down}}{W_{down}} + \frac{C_{up}}{W_{up}}) * \frac{W_m}{2}, \tag{2.20}$$

where, C_{down} and C_{up} are the total recorded counts in the down and up scatter energy windows, W_m is the width of the photopeak window, W_{down} and W_{up} are the widths of the two scatter energy windows.

One limitation of the planar processing method is the overlap of an organ's projection with the projections of other organs or background regions. A variety of ad hoc methods are used, but there is no general and theoretically rigorous method. One method is to use 3D information from registered CT or MRI scans to provide 3D information about the size and spatial relationship. In this case, the volume of organs and the organ to background ratio are used to scale the estimated organ activity and estimate the activity in the overlapped background region. However, this method makes implicit assumptions about the uniformity of the activity concentration in the various regions and does not rigorously take into account the effects of attenuation [45, 46].

2.4.4.2 Quantitative Planar (QPlanar) Methods

We have previously developed a processing method for quantifying organ activities from planar scans, the Quantitative Planar (QPlanar) method [47]. This method is theoretically rigorous, allows rigorous modeling of all image degrading factors, and provides very good accuracy and precision compared to conventional planar processing techniques. In addition, it is very robust to noise, and allows estimating VOI activity even with very low count data [48, 49]. The reason for this is that there are far fewer parameters to estimate, one for each compartment, as compared to SPECT reconstruction, where the number of parameters is the number of reconstructed voxel values and is thus very large. The limitation of this method is the assumption that the activity in the compartments is constant or has some known spatial distribution.

The QPlanar method is based on maximum likelihood estimation [50], an accurate model of the image formation process, and a set of 3D VOIs comprising the object. While still using data from conjugate view planar scans, it allows both accurate and theoretically rigorous compensation for image degrading factors including attenuation (A), scatter (S), the collimator detector response (CDR), partial volume effect (PVE), and background and organ overlap. The 3D VOIs of organs are typically obtained from 3D SPECT/CT images. The 2D projections of the VOIs are estimated using an analytic projector that accurately models the effects of A, S and the CDR. The forward model is given by

$$P_i = \sum_{r=0}^{N} A_r C_{ir}. \qquad (2.21)$$

In eq. (2.21), P_i is the counts in the projection bin i, A_r is the total activity in the rth VOI, C_{ir} is the projection matrix describing the probability that a photon emitted in the rth VOI will be detected in projection bin i, and N is the number of VOIs. This is directly analogous to the projection model in voxelized reconstruction with voxels being replaced by VOIs.

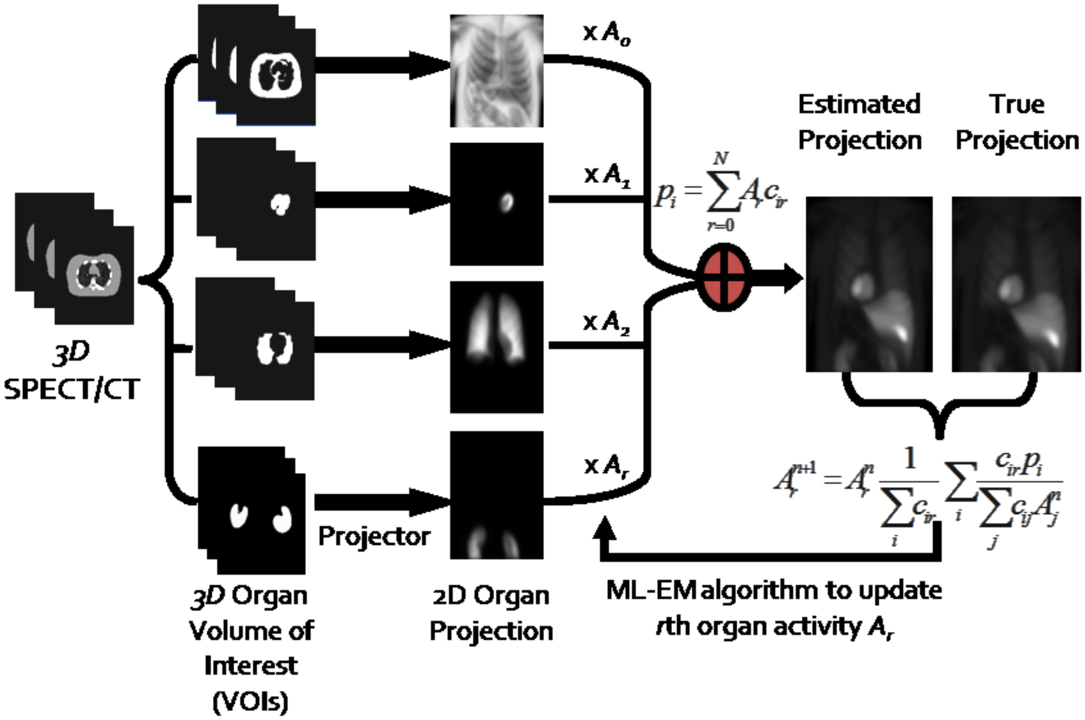

Figure 2- 9: Block diagram of QPlanar algorithm

The update equation for the QPlanar algorithm is as follows:

$$A_r^{n+1} = \frac{A_r^n}{\sum_{i=0}^{M} C_{ir}} \sum_{i=0}^{M} \frac{C_{ir} P_i}{\sum_{j=0}^{N} A_j^n C_{ij}}, \tag{2.22}$$

where, A_r^n is the estimated total activity concentration in region *r* after the *n*-th iteration, *M* is the total number of projection bins in the two projection images, and the remainder of the symbols have the same meaning as in eq. 2.21. Note that this update equation is the same as that used for ML-EM reconstruction except that voxels are replaced by VOIs. The update equation is applied iteratively until the activity estimates converge. Since the number of parameters is small (equal to the number of VOIs), noise amplification in the parameters is not a major issue and early termination is unnecessary. In addition, because the matrix C is small because of the small number of parameters, it can be pre-computed, and the calculations in (2.22) are very rapid. This method inherently and rigorously addresses the problem of organ and background overlap.

2.4.5 SPECT Quantitation methods

SPECT imaging is a method which allows direct estimation of the 3D distribution of activity and thus avoids the problems of organ and background overlap faced by conventional planar quantification. A brief discussion of various SPECT quantitation methods are introduced in the following sections.

2.4.5.1 Image Reconstruction Algorithms

In SPECT imaging, tomographic information from the projection data is obtained either through analytical or iterative image reconstruction techniques. The most widely used analytical reconstruction method is filtered backprojection (FBP)[51]. However, the disadvantage is that it lacks methods to exactly compensate for the image degrading factors discussed earlier. Additionally, FBP does not take into account noise in the data. Therefore, the SPECT images reconstructed using FBP do not provide quantitatively accurate images. Iterative image reconstruction techniques are an alternative to analytical reconstruction method. Iterative methods are based on estimating the reconstructed image by producing series of approximations. Ideally each iteration reduces the value of some measure of the difference between the measured data and the current estimate of the activity distribution. There are several different types of iterative algorithms [52-54]. However, in this section, we limit our discussion to a well-known method of iterative reconstruction, namely “maximum likelihood expectation maximization” (ML-EM) reconstruction method [54] and the closely related OS-EM algorithm.

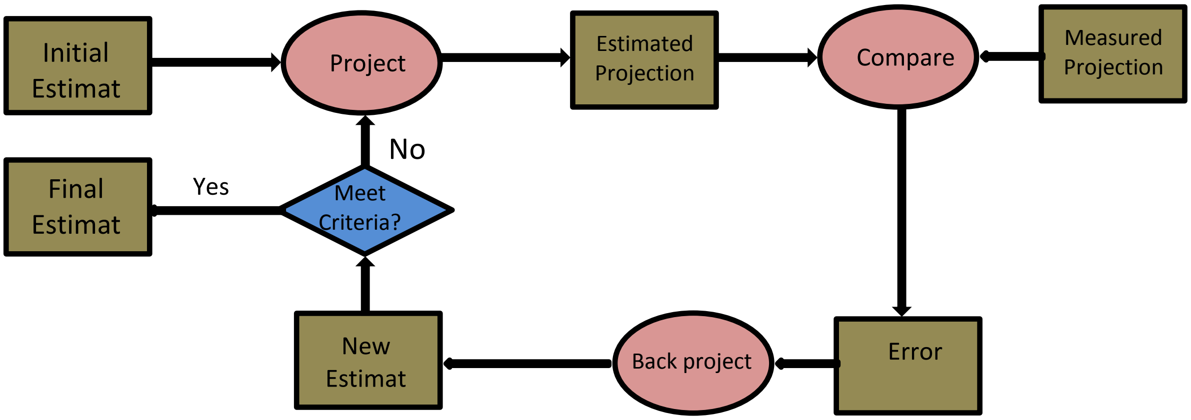

Figure 2- 10: Block diagram of Iterative reconstruction algorithm

Iterative reconstruction is a process of successive approximations where the current estimate approaches, at least ideally, the true activity distribution. The process starts with an assumed initial estimate of an image and computes the projections of the estimated image. This estimated projection is sometimes called the forward projection or reprojection. These estimated projections are then compared to the actual measured projections. In ML-EM and OS-EM this comparison is via a ratio. The outcome of this step is then used to adjust the current estimate. In ML-EM and OS-EM this update involves the backprojection of the ratio image. Ultimately a convergence criterion, typically a fixed number of iterations, is used to terminate the iterative process.

Compared to analytical methods, OS-EM and ML-EM have a number of advantages. One advantage of iterative reconstruction methods is that the underlying physics of imaging process can be modeled in the reconstruction process, thus allowing better compensation for physical degrading factors. Therefore, iterative methods such as OS-EM or ML-EM generally provide better image quality and quantitative accuracy compared to analytical methods. One advantage of OS-EM or ML-EM iterative reconstruction algorithm is the ability to model noise in the projection images by using statistical criterion to find the optimal solution. These advantages result in iterative reconstruction algorithm providing improved noise characteristics and reduced streak artifacts compared to analytical reconstruction.

ML-EM belongs to the category of statistical reconstruction algorithms. The In ML-EM, measured data can be expressed as $p = Ax,$ where, A is an MxN matrix referred to as the transfer matrix and models the image formation process. In MLEM, the measured data are assumed to have a Poisson distribution. The Poisson likelihood function P(p|x) for the measured projection data, p, p given the mean activity distribution x, is given by

$$P\left(p_i \mid x\right)=\prod_{i=1}^{M}\left[e^{-(Ax)_i}\,\frac{(Ax)_i^{p_i}}{p_i\,!}\right]. \tag{2.23}$$

Note, in eq. 2.23, Ax is a matrix vector multiplication. Using the expectation maximization algorithm, eq. 2.23, the Poisson likelihood function is maximized. The expression for the new image estimate y_i^{m+1} as related to the previous or old image estimate y_i^{m} is given by

$$y_i^{m+1} = \frac{y_i^m}{\sum_{j=1}^{M} A_{ji}} \sum_{j=1}^{M} A_{ji} \frac{p_j}{\sum_{k=1}^{N} A_{jk} y_k^m}. \tag{2.24}$$

where, y_i^{m+1} are the elements of the estimated image vector updated after each new updates, p_j is the jth element of the measured projection vector. The element of the projection matrix A_{jk} is the probability that a photon emitted in boxes k is detected in jth projection bin.

The ML-EM algorithm consists of following steps: (1) start with an estimate the reconstructed image *y,* (2)compute the projection of the current estimate *y,* (3) compare this estimated projection data to the measured projection data, (4) backproject the ratio of the measured and estimated projection and (5) update the image estimate by multiplying by this ratio. Note that the update also includes a normalization that consists of voxel-by-voxel division by the image obtained by backprojecting projection data where all elements are equal to unity. Steps 2 to 5 are repeated until a predetermined number of iterations are performed or some stopping criterion is reached.

An improvement of ML-EM in terms of speed is a new modified form of ML-EM called “ordered subsets expectation maximization” (OS-EM) [53]. OS-EM divides the projection data into several subsets and the ML-EM algorithm is applied to each set sequentially. OSEM converges faster than ML-EM. A single iteration of OSEM involves updating the image once for each of the subsets. The computational effort of a full iteration of OS-EM is approximately equivalent to that of an iteration of ML-EM. However, the number of updates is larger by a factor equal to the number of subsets, and the algorithm converges at a speed that is faster by approximately this same factor.

2.4.5.2 Attenuation Compensation

A number of analytical methods have been proposed for attenuation compensation in SPECT. Most of these methods assume uniform attenuation in regions of the body where the media is non-uniform [55-58]. However, the assumption of uniform attenuation in the body degrades the diagnostic and quantitative accuracy leading to artifacts in non-uniform regions such as the thorax. Analytical method using non-uniform attenuation have been proposed recently [59-62]. These methods tend to have poor noise properties and are unable to rigorously compensate for other image degrading factors.

The most common method to compensate for non-uniform attenuation clinically is via statistical iterative reconstruction methods. In this method, the attenuation is modeled in the projection matrix. The key to the accuracy of these methods is having a sufficiently good estimate of the attenuation distribution in the body, known as the attenuation map. One method for obtaining the attenuation map is to estimate them from 3D CT or MR images registered to the SPECT data The key problem with this approach is obtaining accurate registrations and, for MR, estimating attenuation coefficients in each voxel from the MRI images. Censor [63] proposed computing attenuation maps directly from emission data. However, this approach is fundamentally ill-posed, resulting in crosstalk between the attenuation maps and emission images.

In recent years, other emergence of hybrid SPECT/CT scanners [64, 65] has solved this problem by providing well registered attenuation maps from CT scans.

2.4.5.3 Scatter Compensation

Scatter has a smaller effect on quantitative accuracy than attenuation [39]. Scatter also results in reduced contrast in the reconstructed SPECT images. Hence, scatter compensation is desirable to improve both image quality and quantitative accuracy. Scatter compensation can be divided into several categories. These fall into pre-reconstruction methods, post-reconstruction methods, and iterative reconstruction-based methods. An example of pre-reconstruction methods is subtraction-based compensation. In subtraction-based compensation, the scatter components can be estimated using, for example, the DEW or TEW methods described earlier.

In addition, scatter components can be estimated by convolving the scatter response function (SRF) with the measured projections [66]. However, one of the drawbacks of subtraction-based methods is noise amplification approximation of scattering component [67, 68]. An example of a post-reconstruction method is deconvolution of the reconstructed images with the source response function SRF [69, 70]. However, since the SRF is spatially varying, this method involves some level of approximation. This can be done either by explicit scatter models, or via the use of scatter estimates obtained from energy windows as in the TEW method.

To achieve more accurate scatter compensation, explicitly models of the SRF can be used that take into account the spatial variation and object-dependence. This modeling has been accomplished in several ways. One method uses the non-stochastic numerical integration [71, 72]. Another approach uses conventional or fast Monte Carlo simulation [73, 74]. A final approach is with approximate scatter models such as the Effective Source Scatter Estimation method (ESSE) [75, 76]. The disadvantage of Non-stochastic numerical integration method is the need, for the sake of computational complexity, to make simplifications such as modeling only first order scatter [77-79].

Monte Carlo simulation methods are commonly used to model photon scatter with high accuracy. However, for reconstruction they tend to be too computationally demanding. Methods of approximating some aspects of the radiation transport process have been developed to allow their use in image reconstruction. However, the computational burden can still be high. In this work, model-based scatter compensation using the ESSE method was used to compensate scatter effects.

The ESSE method uses the pre-calculated effective scatter sources (ESS) estimated via scatter kernels. The scatter kernels are calculated using Monte Carlo simulation. The kernels are independent of the patient, and thus can be precalculated.

2.4.5.4 CDR Compensation

Since image resolution is largely determined by the spatially-varying collimator detector response function (CDRF), it is an important compensation to be considered. The CDRF is simply the image of a point source in air.

CDRF compensation methods can be categorized into two types. These are analytical-based and iterative reconstruction-based methods. Analytical methods all involve approximations about the shape or spatial variation of the CDRF. In SPECT, the CDRF is spatially invariant [70, 80]. An example of such an analytic method is deconvolution using a restoration filter. In this method the CDRF is assumed to be spatially invariant.

A more rigorous method to compensate for the CDRF compensation is to model the spatially varying CDRF in an iterative reconstruction method. This result in a general improvement in image resolution, but the resulting images still have finite spatial resolution, and CDRF compensation can produce Gibbs-effect-like ringing artifacts in the images. Nevertheless, CDRF compensation general reduces PVEs and improves quantification of activity in small organs and objects of interest like tumors [81, 82].

2.4.5.5 PVC Compensation

In SPECT, partial volume effects (PVEs) result from finite spatial resolution of the imaging system, as described above. Even after CDRF compensation, PVEs reduce the quantitative accuracy of SPECT images in the cases of high energy photon. PVE compensation methods are well established in PET. Some examples are recovery coefficient methods [83, 84], post-reconstruction correction method using anatomical information provided by the high-resolution CT or MRI images [85-87] and iterative reconstruction-based methods [87-89].

2.4.6 Dynamic SPECT

Dynamic SPECT is an imaging procedure where series of SPECT images are generated as a function of time in order to assess the change in spatial distribution of the tracer over time. Dynamic SPECT requires both special acquisition protocols, and, because of the fact that SPECT acquisition involves the use of rotating detectors, 4D reconstruction methods must often be used. [10].

Dynamic imaging can provide additional information to aid in diagnosis. Measuring the ratio of blood flow at stress (maximum flow) and rest (normal flow) can provide quantitative information about presence of either focal defects or microvessel disease. Knowing the state of microvasculature could provide an early indicator of cardiovascular disease before blockages of large arteries develop.

In a static SPECT scan, data are acquired using multiple planar projections obtained at multiple viewing angles. These are typically obtained by rotating a gamma camera around a patient. The rotation can be either continuous or in steps and shot. In step and shot acquisition, the camera is stopped for a specific, and typically constant, duration at each location. The SPECT scanner could consist of either single or multiple cameras. Multiple cameras reduce the total scan time and increases the sensitivity of the SPECT system [90, 91]. Typical SPECT systems have 2 gamma cameras, and these can usually be positioned either directly opposing each other or at near right angles. The latter geometry has advantages for MPS as views from the back of the body tend to be dominated by noise and scatter.

A typical dynamic SPECT scan comprises a series of complete rotations around the body with projection images acquired at a set of equally spaced projection views. In order to obtain high temporally resolution, continuous, fast rotation is typically used. This provides the potential to measure rapid changes in the tracer distribution.

Dynamic SPECT is complicated by the fact that conventional SPECT systems acquire only small number of views of patient at a time. Typical 3D reconstruction methods assume that the projections are of a static activity distribution. However, because of the need to rotate, in dynamic SPECT the projections will be inconsistent with this data model. Thus fast rotation and complicated 4D reconstruction methods that model changes in tracer distribution during acquisition have been proposed to reduce the impact of this effect. The 4D reconstruction methods are complicated and time consuming, so the full physics is often not implemented, and the activity distribution estimates are thus degraded by the factors described above. In addition, the noise levels are very high and voxel values in the reconstruction are likely not estimable in the sense that unbiased estimators do not exist. Thus, dynamic images are likely to be very noisy and regularization will be required.

Knowledge of regional myocardial perfusion is important for the diagnosis and management of coronary artery disease. Currently, Positron Emission Tomography (PET) is arguably the best noninvasive modality for evaluation of myocardial perfusion. However, due to scanner availability in the hospitals PET is not currently used widely to assess Cardiac perfusion. Single Photon Emission Computed Tomography (SPECT) on the other hand, is widely available. Myocardial perfusion studies with SPECT are performed clinically on millions of patients each year. A static imaging protocol is typically used in clinical cardiac SPECT perfusion studies. Many different SPECT tracers have been investigated for studying perfusion. ^{99m}Tc-Teboroxime and ^{201}Tl is a widely used tracer in clinical studies for evaluating myocardial perfusion as well as myocardial viability. The static ^{99m}Tc-Teboroxime and ^{201}T1 images, wherein a single three-dimensional image is obtained, are qualitative in nature but do not provide absolute quantification of myocardial blood flow.

Dynamic imaging has been shown to have promise in obtaining quantitative measures of myocardial blood flows [27, 92, 93]. There has been a significant amount of work investigating dynamic SPECT imaging using ^{99m}Tc labeled teboroxime [7, 27, 93]. Teboroxime has very rapid kinetics that necessitates very fast temporal sampling, making it difficult to image with conventional rotating SPECT systems. However, ^{99m}Tc -labeled teboroxime is a sensitive indicator for changes in response to adenosine-induced coronary vasodilation [7]. Although it is not currently commercially available, it is FDA approved and there is a potential it could be marketed again.

Thallium-201 is a potassium analog and works in conjunction with the Na-K Adenosine Triphosphatase pump. It undergoes high transcapillary extraction during the early uptake phase immediately following administration. Moreover, ^{210}Tl has very slow washout kinetics, which facilitates acquisition of MPS images on conventional rotating gamma cameras. There is evidence that wash-in rate parameters estimated from dynamic thallium SPECT may provide accurate quantitative measures of myocardial blood flow [92]. In this work, we investigate dynamic SPECT imaging with both ^{99m}Tc -labeled teboroxime and ^{210}Tl.

3.0 Investigating the feasibility of whole-heart dynamic myocardial perfusion imaging from pairs of planar views

3.1 Introduction

The purpose of the work in this chapter was to investigate the feasibility of dynamically imaging organ or VOI activities from a single pair of projection views that are obtained simultaneously using a dual-camera system with the cameras in cardiac acquisition mode (i.e., with the cameras at right angles to each other in a perpendicular orientation). However, unlike conventional planar quantification methods, the proposed method uses knowledge of the full 3D shape of the VOIs, an accurate model of the image formation process, and maximum-likelihood estimation techniques, allowing exact modeling of overlap of organs and compensation for physical image degrading factors.

In the data presented here, a conventional slow-rotation SPECT/CT acquisition protocol is used; the requisite 3D VOIs could be estimated from conventional SPECT reconstructions or CT images. In principle, data could be acquired for all or part of the acquisition without rotation. One advantage of rotating throughout the acquisition is that the data could also be used for 4D reconstruction, with the TACs estimated by this method serving as initial estimates for the various reasons. The proposed method allows estimation of regional TACs that could be used as inputs to estimate kinetic parameters of physiological interest, such as blood flow.

The method does not require extremely fast rotation in order to obtain good time resolution, as the time resolution is equal to the acquisition time at each projection. Although this method does require modeling of physics of the image detection system, the system matrix itself is very small. In particular, for each time point the projection matrix is two times the number of projection bins by the number of VOIs, which would typically be less than 10. Computing this matrix including models for attenuation, scatter, and the collimator-detector response takes less than two seconds on current computers. Since the matrix is small it can be stored in memory and the remainder of the calculations is extremely fast. The total time for estimating a typical TAC in this work was less than 3 minutes. Further, because the operations at each time point are completely independent, the TAC estimation can be trivially parallelized, further reducing the computation time by a factor equal to the number of processor cores available. It provides information about dynamic tracer distribution in a small number of VOIs from standard SPECT/CT instrumentation and acquisitions.

To demonstrate and validate this method, we performed a simulation study investigating the feasibility of quantifying time-activity curves for ^{99m}Tc-teboroxime using a sequence of pairs of projection views obtained from a simulated conventional SPECT acquisition. Our primary reason for choosing for ^{99m}Tc-teboroxime was that it provides outstanding characteristics for measuring coronary flow reserve. However, it is not currently available from any manufacturer. However, since it ^{99m}Tc-teboroxime has been approved for human/animal studies, it could potentially be reintroduced if a market developed. In addition, the method could be applied to other traces such as Tl-201 or one of a number of various other tracers with good flow imaging properties.

In this work, patient anatomy was modeled using the realistic 3D NCAT phantom [94]. A realistic patient activity distribution was generated by modeling the kinetics of ^{99m}Tc-Teboroxime based on TAC data from the literature [7]. Projection data were generated using an analytic projector that accurately models the imaging physics [75, 95].

3.2 Perfusion tracer kinetics

We modeled the kinetics of ^{99m}Tc-Teboroxime based on published TAC data [7] for the myocardium and plasma under stress. The data from the paper were extracted from the figures and interpolated using cubic spline interpolation. Kinetics for other organs were unavailable and were thus approximated. We assumed that the activity in the liver, lungs, kidneys and background would reach an equilibrium activity concentration equal to that observed in Tc-99m sestamibi patient scans. We assumed that the shape of the TAC during the uptake phase in these organs was the same as in the myocardium, and that the equilibrium value would be reached at the same time that the myocardial activity reached its maximum value. While this assumption may not be physiologically realistic, after the peak myocardial activity was reached, it gave a different uptake ratio relative to the myocardium for each of these organs and thus provided a test of whether the QPlanar method works for a variety of TACs and in the challenging case where myocardial activity is substantially lower than in surrounding organs such as the liver. Figure 1 shows the TACs for all the organs modeled.

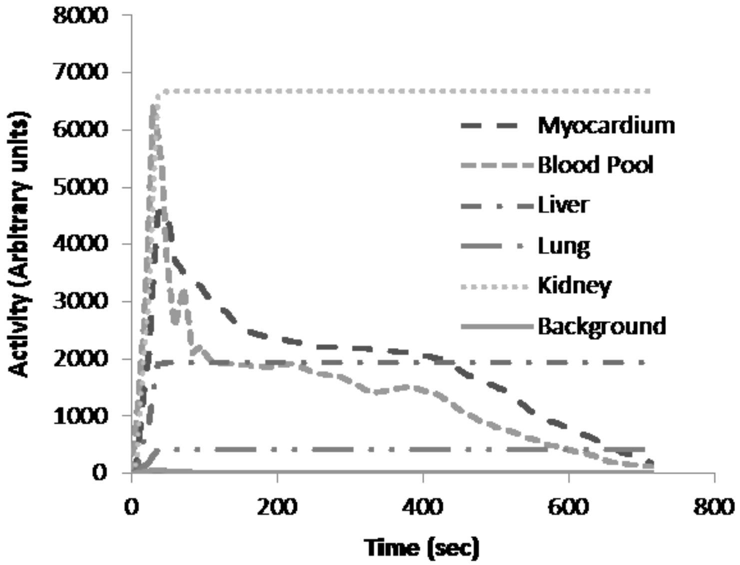

Figure 3- 1: Time activity curves of ^{99m}Tc-teboroxime used in this experiment for various organs. The myocardium and blood pool curves are based on literature TAC data [7].

3.3 Dynamic SPECT projection data modeling

3.2.1 Phantom

Patient anatomy was modeled using the realistic 3D NCAT phantom [94]. In particular, we modeled six organs: the myocardium, blood pool, lungs, liver, kidneys, gall bladder, and background (i.e., body remainder). The activity distribution in each organ was assumed to be uniform except in the lungs, where activity was zero in airways, and in the myocardium, where, as described below, some simulations included a myocardial perfusion defect. In those simulations, perfusion defects were placed in the anterior wall of the mid left ventricle myocardium with extents ranging from 5% to 25% of the myocardial volume. All simulated defects were transmural, and the angular extent around the short axis slice and the length in the long-axis direction were set so that the defect had similar physical lengths in both directions. The corresponding range of short axis angular extents was 30 to 64^{o} and the extents along the long axis ranged from 3 to 6 cm. Defect severities ranged from 25% to 100% reduction in myocardial activity concentration in the defect region. Sample phantom images containing defects with 100% severity and samples of the extents are shown in Figure 3-2. Cubic voxels with a side length of 0.1562 cm were used in generating the voxelized phantom and defects.

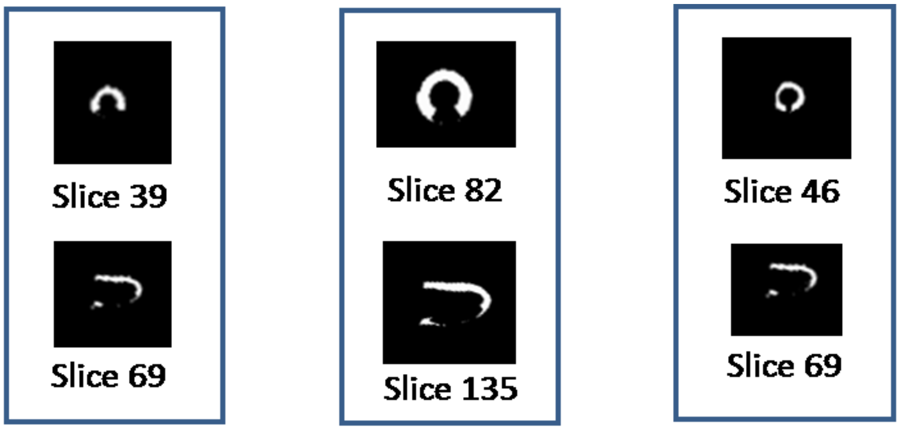

Ext. 25%, sev. 100%

Ext. 16%, sev. 100%

Ext. 5%, sev. 100%

Figure 3- 2: Horizontal short axis vertical long axis images of the myocardium with perfusion defect of extents 5%, 16%, and 25% and severity of 100% in the anterior wall of left ventricle.

3.2.2 Projection data generation

Noise free-projection data were generated for the six organs modeled including the background using an analytic projector that models attenuation, scatter and the collimator-detector response [75, 76, 95-97] . Projection data were generated in 128×128 bins at 120 views over 360° with a 0.1562 cm bin size. Projection data modeled acquisition with a two-camera system in a right angle configuration over 360° of camera rotation, a 20% wide energy window and a 9% energy resolution, a 4 mm intrinsic resolution, and a LEHR collimator. Phantom projection data were first generated using an analytic projector with a small projection bin size (.1562 cm) and then collapsed to the assumed acquisition bin size of 0.312 cm to model the continuous nature of the activity distribution in the body. We modeled fixed rotation with distance from center of rotation to collimator face 25 cm since body contouring orbits might not be feasible with acquisition durations used in this work.

To allow capture of the rapid uptake phase, we simulated a projection acquisition duration of six-seconds. Step-and-shoot acquisition using such a short acquisition duration would be inefficient, so we modeled continuous rotation. To model continuous rotation, projections were generated at an angular increment of 3 degree and summed over a 9 degree range that correspond to a single projection. We modeled the variation in tracer uptake during each six-second acquisition by sampling the TAC at 6 second intervals for these three projections so that the summed projection corresponded to a 9 degree angular rotation and a eighteen second acquisition duration. This provided modeling of both change in viewing angle and redistribution of the tracer during the acquisition of data for one six-second projection view.

To generate a series of dynamic images, a projection data set for each organ was first created assuming unit activity in the organ using the model-based analytical projector. These sets of projection data were then scaled by the TAC value at the time of the projection, and the projections for all the organs were summed to produce noise-free measured projection data.

For experiments requiring noisy projections, noise was added to noise-free simulated data using a Poison generated pseudo-random number generator. Since the simulation realistically modeled sensitivity of the gamma camera and the activity in the various organs, the count levels in the simulation were appropriate for the specified acquisition duration and tracer kinetics. A total of 300 sets of noisy projection data were generated using independent sequences of random numbers in order to study both the mean bias and variance of the TAC estimates.

3.2.3 Application of QPlanar to estimate organ activity

The experiment was carried out in four parts in order to assess various aspects of the estimation process. In all 4 parts, the QPlanar method was applied to estimate the activity concentration in each organ in a set of 3D VOIs at each time point, thus creating estimated TACs directly from the projections. Part one involved assessing the activities over time in the myocardium and blood pool when the activity concentration inside each organ was uniform and Poisson noise was not simulated. In part two, we added Poisson noise to the projection data from part 1 to assess the effect of noise on the bias and precision of the estimated activities over time in the myocardium and blood pool. As mentioned above, the QPlanar method assumes that the activity distributions in the VOIs are uniform. In clinical application the activity distribution may not be uniform due to the presence of perfusion defects. Thus, in parts 3 and 4 we applied the QPlanar method to cases where the activity distribution in the myocardial VOI was not uniform by introducing perfusion defects with various extents and severities into the left ventricular myocardium. In all cases, the activity concentration inside the perfusion defect was assumed constant. Using these data, we investigated two scenarios. In the first scenario, corresponding to part 3 of the experiment, it was assumed that the perfusion defect, though present in the data, was not known in the QPlanar process. In other words, a single myocardial VOI was used during QPlanar estimation with the assumption of uniform activity in the entire myocardial VOI. In the second scenario, corresponding to part 4 of the experiment, we assumed that the boundaries of the perfusion defect were known, and that the defect was treated as an additional VOI whose activity was estimated. This scenario modeled the case where the defect was large enough that it could be detected in conventional myocardial perfusion SPECT images and thus could be treated as a separate VOI in TAC estimation.

3.2.4 Evaluation of QPlanar method

To evaluate the utility of the QPlanar method in estimating organ TACs, we computed the mean and standard deviation of the activity estimate for each organ obtained at each time point over the 300 noise realizations. For each of these TACs including both noise free and noisy data, we computed the average percent bias compared to the ground truth TAC and calculated average weighted bias for the VOI as:

$$\text{Weighted average absolute bias} = \frac{\sum | A_i - \tilde{A}}{\sum A_i} \times 100\%, \quad \text{..........(3)}$$

where, A_i is true activity at time point *i*, and $\tilde{A}$ is the estimated activity at time point *i*. Note that this is equivalent to weighting the relative bias at each time point by its activity. This weighting was used so that errors at time points with very small activity values did not have undue influence on the average biases reported. For the noisy data we computed the weighted average of the coefficient of variation (COV) using

$$\%\text{weighted COV (VOI)} = \frac{\sum_i \sqrt{\sum_n \left(TAC_{i,n}^{est}(VOI) - \overline{TAC_i^{est}}(VOI) \right)^2}}{\sum_i \overline{TAC_i^{est}}(VOI)} \times 100\%, \text{ ....(4)}$$

where, $TAC_{i,n}^{est}\left(VOI\right)$ is the estimated TAC at time point *i* for the VOI from the *n*th noise realization and $\overline{TAC_i^{est}}\left(VOI\right)$ is the mean over noise realizations. Again, this is equal to the average of the COV weighted by the mean value of the TAC at each time point.

3.4 Results

We first investigated the bias in TACs using noise-free data for the ideal case where the myocardial activity distribution was uniform. Figures 3-3 and 3-4 show plots of the estimated and true TACs of the myocardium and blood pool from noise-free data. The difference between these two TACs is also shown. Note that, for the myocardium, the bias was consistently low. For the blood pool, there was a somewhat larger bias at early time points due to the rapid change of tracer concentration in the region relative to the acquisition duration. However, the bias was very low at times where the TAC was changing slowly relative to the projection duration of 6 seconds. An optimized time interval appropriate for the tracer used would likely reduce this early bias. The average weighted absolute biases for heart and blood pool were 4.7% and 5%, respectively. The maximum percent biases for heart and blood were 16% and 23%, respectively. In both cases the minimum percent bias was approximately 0%. These data demonstrate that the task of estimating the activity from 2 orthogonal planar projections given the exact 3D VOIs and assuming uniform activity in the VOIs is feasible and provides accurate estimates.

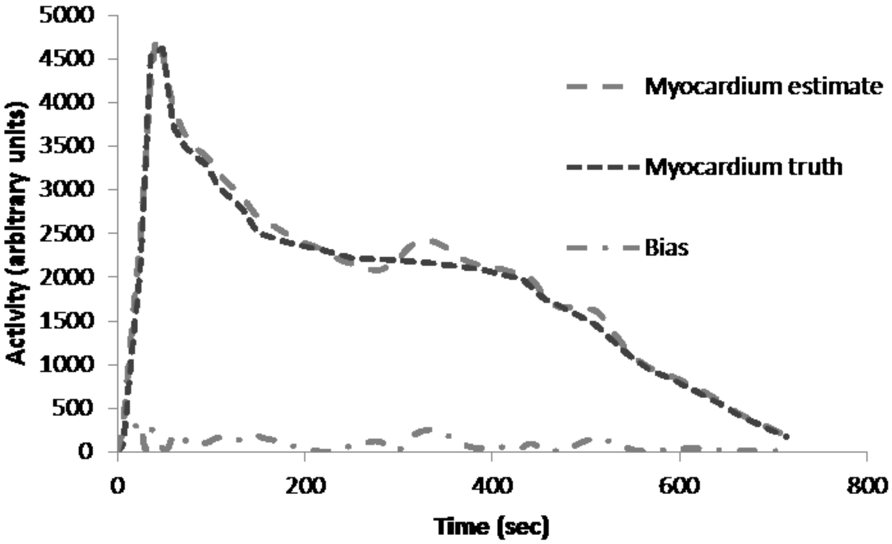

Figure 3- 3: Comparison of the ground-truth TAC and TAC estimated from noise-free data for the myocardium. Bias is the difference between the TAC estimated from noise-free data and the ground truth TAC.

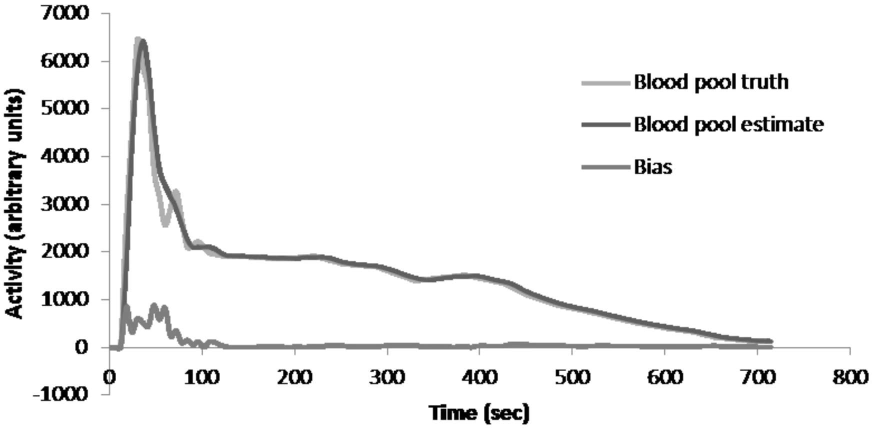

Figure 3- 4: Plot of TAC of the blood pool estimated from noise-free data compared to the true blood TAC. Bias is the difference between the TAC estimated from noise-free data and ground truth TAC.

To investigate the noise characteristics, we analyzed data corrupted by Poisson noise. Figures 3-5 and 3-6, show plots of the mean and standard deviation of the TACs of the blood pool and myocardium from 300 noise realizations compared to the TAC from noise-free data. The difference between the mean and noise-free TACs is also shown. These data demonstrate that using noise-free data is a suitable proxy for investigating bias. The weighted average absolute bias for heart and blood pool were 4.7% and 5%, very similar to the values obtained from the noise-free data .In combination, the data from Figures (3) and (4), which were the bias estimated from noise-free data, and Figures 3-5 and 3-6 demonstrate that the method produces relatively unbiased TACS when the assumptions of the method are met, i.e., the ideal VOI boundaries are known and the activity distributions inside the VOIs are uniform. The magnitude of the standard deviations in Figures 3-5 and 3-6 indicate the sensitivity of the method to noise. The average weighted COVs were 11.7% and 35% for the heart and blood-pool TACS, respectively.

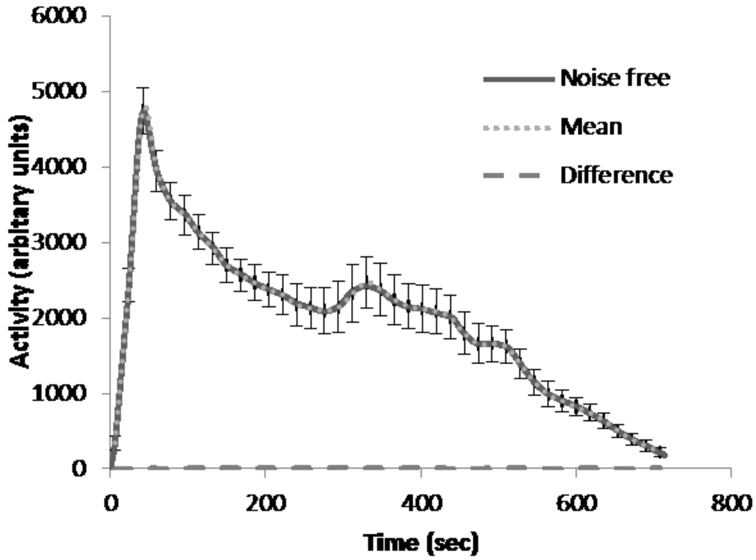

Figure 3- 5: Plot of the mean of 300 estimates of the myocardial TAC from noisy data compared to the TAC estimated from noise-free data. The difference in these curves is also plotted. The error bars represent the standard deviation of the TAC values.

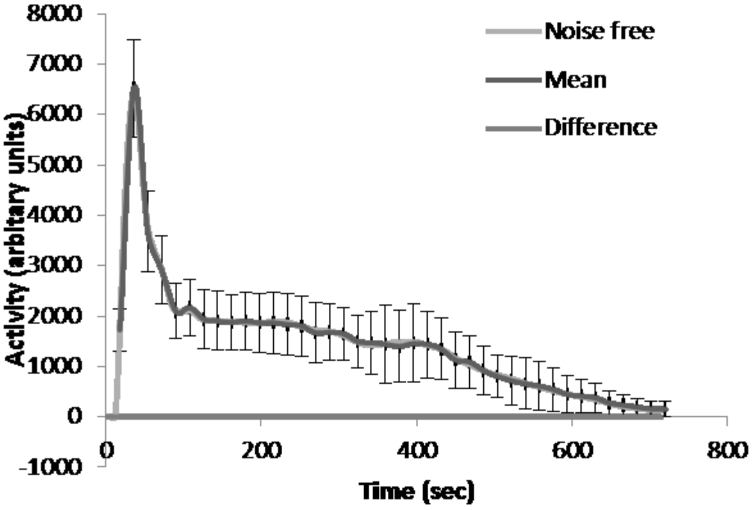

Figure 3- 6: Plot of the mean of 300 estimates of the blood pool TAC from noisy data compared to the TAC estimated from noise-free data. The difference in these curves is also plotted. The error bars represent the standard deviation of the TAC values.

In the previous figures, we showed that when the activity distribution in the myocardium was uniform, as assumed by the object model, we obtained low-bias estimates of the TACs in the myocardium and blood pool. However, in practice there may be perfusion defects in the myocardium resulting in violation of this assumption. As a result, we investigated the possibility of estimating the activity distribution in the presence of perfusion defects of various sizes and extents as described above. We investigated both the case where the perfusion defect position was not known and was assumed in the estimation procedure to have the same activity as the rest of the myocardium, and where the boundaries of the perfusion defect were known and the activity in the defect was estimated. Since we demonstrated above that the bias from noise-free data was a good proxy for the mean bias from multiple realizations of noisy data, in these studies we used noise-free data to investigate the bias introduced by this object model mismatch.

To investigate the effects of unknown defects we investigated defect extents of 0, 5, 16, and 25%, each with severities of 25, 50, 75, and 100%. Figure 3-7, shows a plot of the TAC estimated from noise-free data compared to the true TAC for the case of a defect with 5% extent and a severity of 100%. The weighted average absolute bias for heart was 8%. The maximum percent bias for heart was 29% and minimum bias was approximately 0. Figure 3-7 shows the average weighted biases for each of the other cases. These data demonstrate that the average weighted bias was less than 30% in all cases and less than 10% for cases where the total reduction in myocardial activity (product of defect extent and severity) was less than 5%, i.e., for all the defects with 5% extent and the 25% severity defects with 16 and 25% extents.

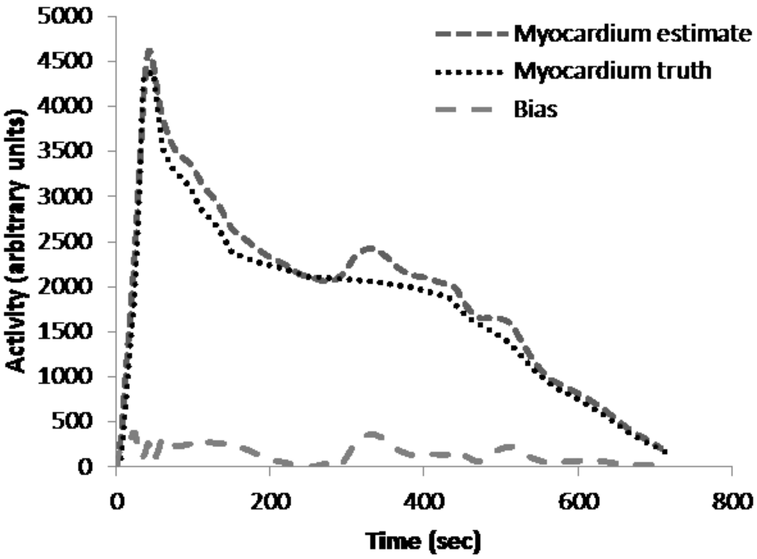

Figure 3- 7: Plot showing estimate of the myocardium TAC from noise-free data with a perfusion defect size of 5% and severity of 100% in left ventricle of the myocardium. In this case the perfusion defect VOI was not included in the estimation procedure. Bias is the difference between the TAC estimated from noise-free data and ground truth TAC.

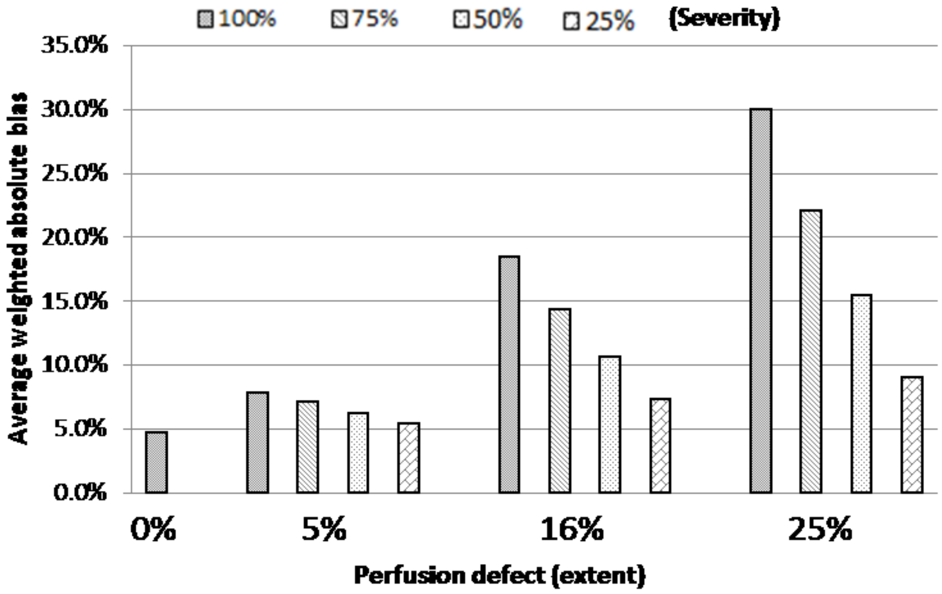

Figure 3- 8: Average weighted absolute percent bias in the estimated myocardial TAC in the presence of perfusion defects with various extent and severity combinations when the defect was not modeled during the QPlanar estimation procedure. The estimates were from noise-free data.

The above results indicate that the presence of a large unknown perfusion defect (extent of 25%) degraded the fidelity of the myocardial TACs. However, in the case of a large defect, the defect could be visualized in SPECT images, and thus defining a defect VOI would be possible. To explore this, we introduced a defect with a 25% extent and 100% severity into the myocardium. In the QPlanar estimation procedure we included VOIs both for the normal myocardium and the defect.

Figure 3-9 shows the true and estimated TACs for the case when the true VOI for the defect was included in the QPlanar estimation procedure. The resulting TACs were relatively unbiased, indicating that, given the defect VOI, it is still possible to estimate the myocardial TAC with good accuracy. The average weighted absolute bias for the heart was 1.44%, very similar to the case of no defect. The maximum percent bias for heart was 14% and minimum percent bias was approximately 0%. The maximum percent bias for the defect was 1% and minimum percent bias was approximately 0%.

Figure 3-10 show the average weighted absolute bias for the range of severities studied with fixed extent (25%) when the true VOI for the defect was included in the QPlanar estimation procedure. The resulting TACs were relatively unbiased, indicating that, given the defect VOI, it is possible to estimate the myocardial TAC with good accuracy.

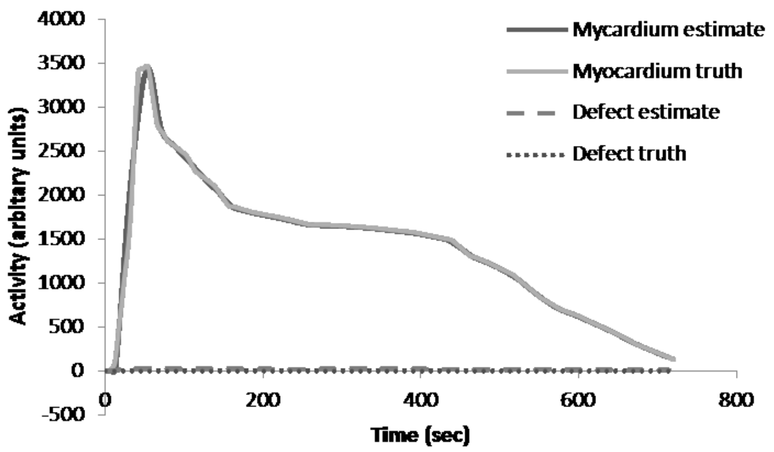

Figure 3- 9: Plot of the myocardial TACs obtained for a defect with 100% severity and 25% extent. The myocardial and defect activity estimates were obtained using the proposed method with the defect VOI included in the QPlanar estimation procedure. The true and estimated defect and myocardial TACs are shown. The defect truth overlaps the x axis reference line since it is zero at each time point. The estimates were from noise-free data.

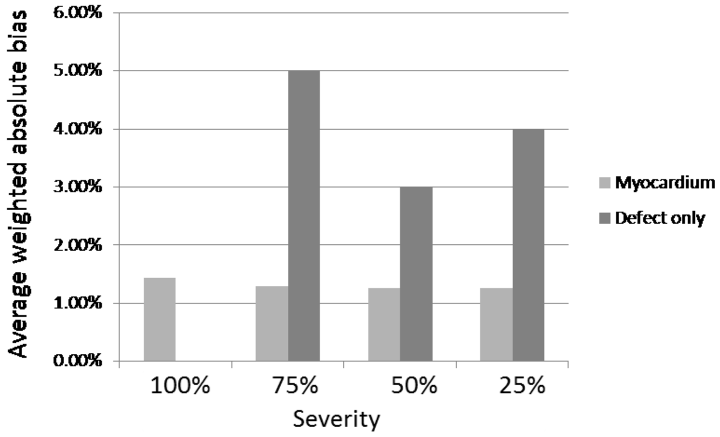

Figure 3- 10: Average weighted absolute percent bias in the estimated myocardial TAC in the presence of perfusion defects with fixed 25% extent and various severity combinations when the defect was modeled during the QPlanar estimation procedure. The estimates were from noise-free data.

3.5 Discussion

Measuring dynamic processes with conventional SPECT systems is complicated by the need to rotate the gantry to acquire sufficient projection data for tomographic reconstruction and the time-varying nature of the radionuclide distributions being imaged, resulting in inconsistent projection data sets. Previous methods required very fast rotation or 4D dynamic SPECT reconstruction methods. We have proposed a method to extract the time-activity curve for a small number of compartments in the body, such as the normal myocardium, blood pool, and ischemic regions, from SPECT data acquired with conventional cameras using slow rotation and without requiring fully 4D reconstruction. Note that rotation during the entire acquisition is not a prerequisite for the method. However, rotation provides the flexibility to use appropriate subsets of the data for 3D or 4D SPECT reconstruction. In particular, images reconstructed from data at later time points when the activity is not changing rapidly could be used to define organ VOIs. This method adapts recently-developed methods for quantitatively estimating activity in 3D volumes-of-interest (VOIs) from planar projections and a registered CT image. The method uses pairs of projections that are obtained concurrently from a dual-camera SPECT system where the two gamma cameras are arranged at right angles, the orientation commonly used for myocardial imaging, to estimate the activity in myocardial, blood pool, and, if needed, hypo-perfused regions of the heart. The definitions of these regions could be obtained from a conventional static SPECT/CT scan.

The feasibility of the method was demonstrated in this paper using a realistic simulation. Our method for estimating organ TACs from pairs of orthogonal projections and a 3D model of the object that is based on Maximum Likelihood (ML) estimation using the QPlanar method originally developed for opposing planar views. We investigated the feasibility of estimating TACs in the myocardium and blood pool using this method and in the context of dynamic imaging of Tc-99m teboroxime using simulated data based on published organ kinetics [7]. We found that when the object model and object agreed well, i.e., the exact organ VOIs were known and the activity distribution in each VOI was uniform, the method estimated TACs that agreed well with the true TACs (average weighted absolute bias ≈ 5% for the myocardium and ≈ 10% for the blood pool).

When the myocardium included an unknown perfusion defect, it was still possible to estimate TACs with good fidelity (average weighted absolute bias less than 10%) as long as the product of defect extent and severity, corresponding to the total fractional reduction of myocardial uptake, was less than or equal to 5%. This suggests that the model is robust to moderate non-uniformities in myocardial uptake. For larger defects, the average weighted absolute bias was greater than 9% but less than 30% in the estimated myocardial activity for all the defect extents and severities investigated. However, if the object model included VOIs encompassing the normal myocardium and the defect, estimated TACs in both the normal myocardium and defect (25% extent and 100% severity) were very similar to the true TACs (average weighted absolute bias ≈ 5%). Furthermore, severities of 75%, 50% and 25% with 25% extent showed similar bias with regards to estimating the TAC for the defect and normal myocardium regions.

The major practical advantage of the proposed method is that the number of unknown parameters is substantially reduced compared to full dynamic SPECT reconstruction. This reduction of unknown parameters is due to the fact that the number of VOIs is much smaller than the number of reconstructed voxels. Also, due to the small number of parameters, the matrix relating the measured projection data to the VOI activities is small and can be stored in memory. In addition, because of the small number of parameters, the inverse problem is better conditioned than the problem of estimating the TAC in each voxel and additional regularization was not essential.

Despite the promise indicated by this study, there remain a number of technical challenges. First, the method requires accurately delimited VOIs for the various organs and compartment. We envision obtaining these from SPECT images acquired at later time points when the activity distribution is changing relatively slowly. We have previously used a SPECT study acquired at a different time point to define VOIs for use with the QPlanar method and obtained good results in patient studies[98]. CT images may also be useful in defining VOIs for some organs. Other areas that require additional investigation are the acquisition protocol, including the acquisition duration per view and number of rotations, the effects of imperfect VOI definition, and the bias and variance properties of kinetic parameters estimated from the TACs.

We have previously studied the effects of VOI misdefinition on the accuracy of organ activity estimates obtained using the QPlanar method [99]. That study investigated misdefinition by randomly perturbing control points that defined organ VOIs. Perturbations with equal probabilities in all directions and with probabilities that led to net increase or decrease of the VOI volume were investigated. For small organs such as the kidneys we observed errors less than 1% for perturbations that did not result in a volume change, and of 5 and -8% for perturbations that resulted in a volume increase or decrease, respectively. Those results suggest that, while VOI definition is important, modest errors in VOIs lead to modest errors in activity estimates.

Finally, for some application, it might be useful to obtain regional flow. While we restricted the demonstration of the proof of principle to the myocardium and an optimal defect region, the method could, in principle, be extended to multiple regions, for example, regions corresponding to vascular territories. However, we have not investigated that potential in this paper

3.6 Conclusion

There has been a great deal of recent interest in estimating cardiac flow reserve and other parameters that require dynamic imaging. This chapter presents a new approach for estimating the time-activity curves for the myocardium and blood pool, which are requisites for kinetic analysis needed to calculate myocardial flow. The method is based on planar projections obtained from orthogonal projections acquired by a conventional gamma camera with perpendicular cameras.

The method uses 3D VOIs that could be obtained by segmenting static SPECT/CT acquisitions or registered contrast CT images, a method for realistically modeling image-degrading effects including scatter, attenuation, and the collimator-detector response, and a maximum-likelihood estimation procedure. In a simulation study modeling the kinetics of Tc-99m teboroxime, we showed that it was possible to obtain good estimates of the myocardial (average weighted absolute bias of ≈ 5 %) and blood-pool (average weighted absolute bias of ≈ 10 %) TACs when the true organ VOIs were known and the activity distributions in the organ were uniform. In the presence of unknown perfusion defects, the myocardial TAC was still estimated well (average weighted absolute bias < 10%) as long as the total reduction in myocardial activity was ≤5%. This indicates that the method is robust to modest model mismatch. In the case of larger defects where the defect VOI was included in the estimation procedure, the estimated normal myocardial and defect TACs were accurate (average weighted absolute bias ≈ 5% for a defect with 25% extent and 100% severity). These data suggest that this is a promising method for obtaining dynamic information about the myocardium from relatively slow SPECT scans without the use of 4D dynamic SPECT reconstruction methods.

4.0 Accuracy and precision of kinetic parameters

4.1 Introduction

According to the AHA, cardiovascular disease resulted in an overall rate of death of 222.9 per 100,000 Americans in 2013 [100]. Myocardial perfusion SPECT is often used in the diagnosis of cardiovascular disease. However, a limitation of existing SPECT methods is that they provide information only about relative differences in regional perfusion, and changes in relative regional perfusion from rest to stress. That is, quantitative information about the absolute blood flow is not provided. The addition of quantitative information about flow is desirable for diagnosing triple vessel disease, where stenoses in all three major coronary arteries cause a reduction in blood uptake in the entire heart. A quantitative assessment of flow would also allow the calculation of flow reserve, which measures the ability of the vasculature to provide additional blood flow when the heart is stressed.

A number of SPECT tracers have been investigated for studying perfusion. However, one tracer that is currently commercially available and used clinically in studies for evaluating myocardial perfusion is ^{201}Tl. A static imaging method is typically used in clinical cardiac SPECT studies. Static or gated imaging protocols and analysis are typically used in clinical cardiac SPECT studies. These protocols do not provide information about dynamic tracer distribution in the myocardium, and thus cannot be used to estimate absolute blood flow.

Furthermore, because the measurements performed with a static imaging method may not reflect the true underlying physiological changes in a region of interest, a dynamic imaging method allows for the extraction of TACs and a post processing method to estimate kinetic parameters and provide information about the temporal distribution of the tracer. Dynamic imaging using ^{201}Tl has been used in obtaining quantitative measures of myocardial blood flows [26, 92, 101].

In dynamic SPECT, parameter estimation is used to mathematically extract physiological information about cardiac function from dynamically measured data. In this chapter, data are collected with a rotating camera. Kinetic analysis requires a blood input function, which can be obtained either by drawing an VOI over the myocardial blood pool in the reconstructed images or by withdrawing blood samples at various times during the image acquisition and counting the samples in a well counter. In this chapter, the blood input function is obtained by withdrawing blood samples at various times during the image acquisition and counting the samples in a well counter. Blood pool and myocardial VOI TACs are then fitted with a Matlab based Levenberg-Marquardt [36, 37] implementation of a two-compartment model that represents the tracer kinetics.

The parameters thus obtained may represent physiological parameters (chapter 2, sec. 2.3) such as myocardial blood flow, thereby providing an objective analysis of the underlying physiological function. The quantitative measurements obtained with a dynamic imaging method such as this may be particularly useful during evaluation of myocardial perfusion in two cases. (1) Evaluation of cardiac viability and in risk stratification of patients after infarction [102], and (2) evaluation of flow reserve. Cardiac viability can be evaluated using quantification of distribution volumes [101]. Distribution volume is the ratio of the rate of wash-in (k_{21}) to the rate of wash-out (k_{12}). It has been shown previously that reductions in global flow reserve may be early indicators of cardiovascular disease [103].

In Chapter 3, we evaluated the accuracy of estimating TACs using a new approach for estimating the time-activity curves for the myocardium and blood pool, which are requisites for the kinetic analysis needed to calculate myocardial flow [104]. The method was based on planar projections obtained from orthogonal views acquired by a conventional SPECT system with perpendicular cameras. It used 3D VOIs that could be obtained by segmenting static SPECT/CT acquisitions or registered contrast CT images, a method for realistically modeling image-degrading effects including scatter, attenuation, and the collimator-detector response, and a maximum-likelihood estimation procedure. In a simulation study modeling the kinetics of Tc-99m teboroxime, we showed that it was possible to obtain good estimates of the myocardial TACs when the true organ VOIs were known and the activity distributions in the organ were uniform.

The work of this chapter differs from the previous work in two principal ways. In the previous work we found that there was some bias when compared to the true TACs. However, bias in the TACs results in bias of kinetic parameters, and thus bias in the estimated flow reserve. In this work we studied the effects of bias in TACs on the estimated kinetic parameters.

Additionally, in the previous work we simulated Tc-99m teboroxime. While it is a good flow tracer, it is not commercially available because its rapid redistribution in the heart makes static SPECT challenging [7]. Therefore, we chose to investigate ^{201}Tl instead, which has good flow characteristics and is currently used in clinical practice. Tracers that are good for myocardial perfusion imaging are blood-flow dependent. ^{201}Tl is a potassium analog that is acted on by the Na-K Adenosine Triphosphatase pump [105]. During the early uptake, it undergoes high transcapillary extraction. ^{201}Tl also has slow wash-out kinetics. Iida and colleagues provided evidence that estimation of wash-in parameters from dynamic ^{201}Tl studies could provide accurate quantitative measures of myocardial blood flow [101]. Good tracers must also retain in the myocardium long enough to allow imaging. However, ^{201}Tl is not as good as Tc-99m in terms of its imaging performance due to its multiple emission peaks and lower energy, resulting in larger attenuation artifacts, higher noise, and larger scatter effects.

In the work presented in this chapter, we first investigated the bias in TACs using noise-free data for the ideal case where the myocardial activity distribution was uniform. This provides information on the bias of the method because, as demonstrated in Chapter 3, the estimates from noise-free data are a good proxy for the mean of estimates from noisy data. Following this, we investigated the results for an ensemble of noisy data in order to estimate the precision of the method. In both cases, we examined the effects of errors in the estimates of the TAC on the global kinetic parameters.

This chapter is organized into three sections. First the methods section provides a brief introduction to kinetic parameter estimation. More detailed discussion on kinetic parameter estimation was presented earlier in this thesis (chapter 2, sec. 2.3). The method section further discusses the methods used to obtain the ground truth kinetic parameters. Next, the imaging simulation section discusses relevant imaging parameters, phantom generation and application of the QPlanar method. The imaging section is followed by the results section and a brief discussion section to summarize the work described in this chapter.

4.2 Methods

To evaluate flow reserve we used the following two-compartment model consisting of a blood compartment and a tissue compartment (Figure 4-1).

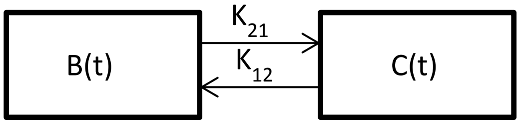

Figure 4- 1: Block diagram two compartment model.

The exchange of the tracer between the two compartments can be described by the following equation:

$$\frac{dC(t)}{dt} = k_{21}B(t) - k_{12}C(t), \tag{4.1}$$

where, *B(t)* is the tracer concentration in the blood, k_{21} and k_{12} are the wash-in and wash-out rate parameters, respectively. Solving Equation (4.1) for the tissue concentration, *C(t),* assuming that *B(t)* = 0 and *C(t)* = 0 at t=0, gives:

$$C(t) = B(t) \otimes k_{21}e^{-k_{12}(t)}, \tag{4.2}$$

where, $\otimes$ is the symbol of convolution operation.

Eq. 4.2 depicts tracer flow through the heart in which tissue activity is k_{21} at t=0 and then exponentially drops with a rate of k_{12} per unit time or a half-life of $0.693/k_{12}$. The tissue time-activity curves can be obtained from the tissue region, and the blood input function *B(t)* can either be obtained by arterial sampling of blood or from image-derived time-activity curves.

Once the measured tissue time-activity curve is obtained, it can be fit to eq. 4.2 to estimate k_{21} and k_{12}. This parameter estimation process is an inverse problem, where the kinetic rate parameters are estimated by fitting the measured tissue time-activity curves to the model.

There are many methods available for estimating the kinetic rate parameters. Many considerations such as sampling and statistical quality of the measurements are important for successfully estimating the parameters. We chose to apply least-squares method of parameter estimation [34] due to its modest computational burden and robustness to noise. Least-squares methods attempt to obtain fits by minimizing the least squares objective function expressed as

$$\sum_{i=1}^{N}(C_i - C(T_i))^2, \tag{4.3}$$

where, i is the index of the measurements over time, C_i is the modeled uptake and $C(T_i)$ is the measured tracer uptake at time T_i.

To account for the uncertainties of the measurements of C_i from one scan to the next, a weighting factor W_i is used in the minimization expression [35].

$$\arg\ \min\ \{\sum_{i=1}^{N} W_i (C_i - C(T_i))^2\}. \tag{4.4}$$

A Matlab implementation of the Levenberg-Marquardt algorithm [36, 37] to estimate both K_{21} and K_{12}.

4.2.1 Kinetic model and parameters for ^{201}Tl

In the simulation, we modeled the kinetics of ^{201}Tl based on published TAC data [101] for the myocardium and blood pool under stress. These data were extracted from the figures and interpolated using cubic spline interpolation.

In order to establish the ground truth, we performed following steps.

1. Extract blood pool TAC data under stress from blood pool data provided in publication [101].
2. Use of the value of k_{21} from data provided as a function of MBF (eq.4.5) and k_{12} in publication [101].

$$k_{21} = -.022 + (.804 * MBF). \tag{4.5}$$

3. Use the stress MBF value provided in publication [101].

Table 4-1 below provides values used for k_{21}, k_{12} and MBF used to generate ground the truth TAC.

Table 4- 1: The values of k_{21} (wash-in), k_{12} (Wash-out) and MBF used to construct ground truth TACs.

k_{21} (ml/min/gm)	k_{12}(ml/min)	MBF (ml/min/gm)
.5	.11	.65

Predicted myocardium tissue TAC is shown in Figure 4-1.

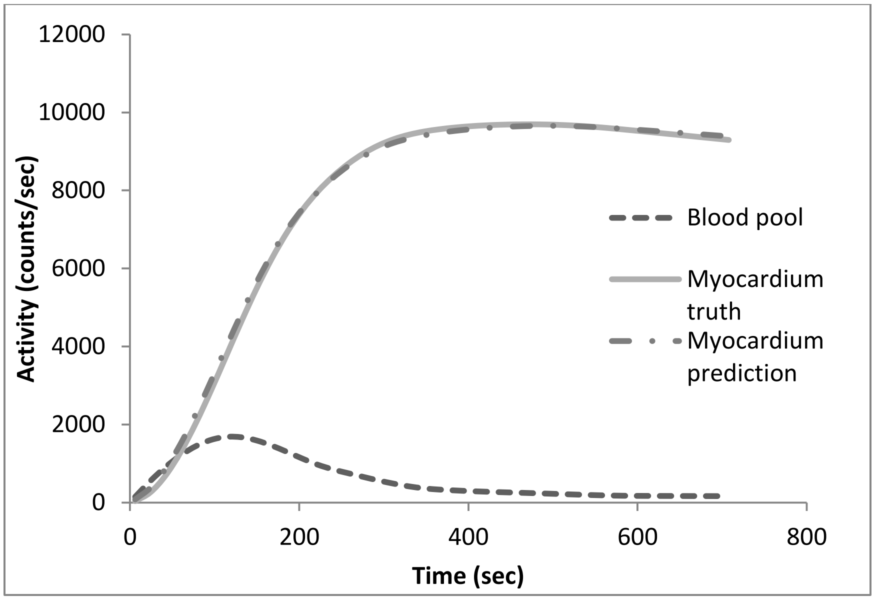

Figure 4-1: Plots of ground truth TACs and predicted myocardium TAC using a two-compartment model fit.

Using the myocardium tissue TAC calculated from values in Table 4-1 as the new ground truth myocardium TAC and stress blood pool data provided in publication [101], we again fitted a two-compartment model to obtain k_{21} and k_{12} depicted in Table 4-2 below.

Table 4- 2: The values of k_{21} (wash-in), k_{12} (Wash-out) as ground truth from a two-compartment model fit.

k_{21} (ml/min/gm)	k_{12}(ml/min)
.5538	.1265

Since kinetics for other organs were unavailable, they were approximated assuming the activity in the liver, lungs, kidneys and background would reach an equilibrium activity concentration equal to that observed in Tc-99m sestamibi patient scans. We assumed that the shape of the TAC during the uptake phase in these organs was the same as in the myocardium, and that the equilibrium value would be reached at the same time when the myocardial activity reached its maximum value. While this assumption may not be physiologically realistic, it produced a different uptake ratio relative to the myocardium for each of these organs after the peak myocardial activity was reached. Thus this assumption made it possible to determine whether the QPlanar method is applicable for a variety of different relative organ activities, including the challenging case where myocardial activity is substantially lower than in surrounding organs such as the liver. Figures 4-2 and 4-3 show the ground-truth TACs for all the organs modeled.

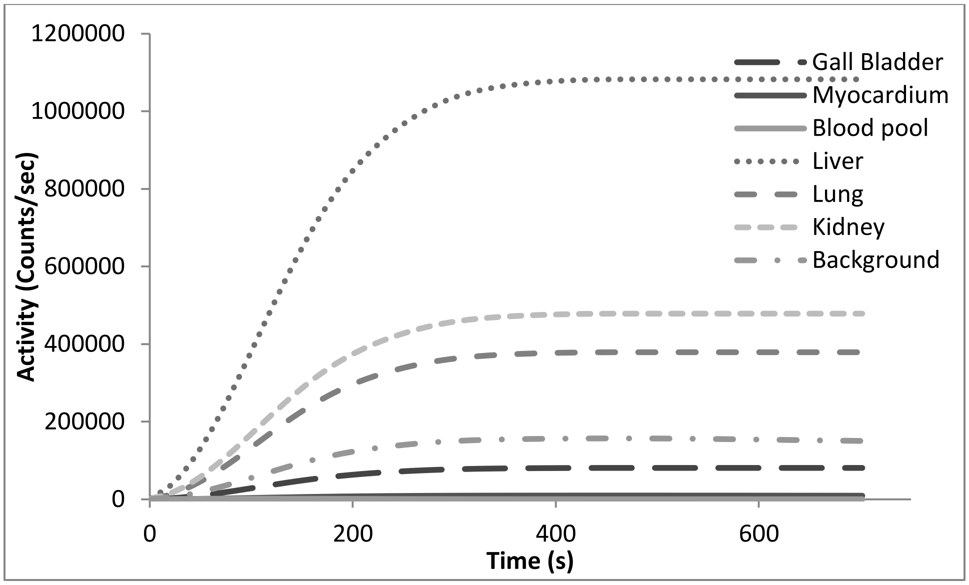

Figure 4- 2: Ground truth time activity curves of ^{201}TL used in this experiment of various organs.

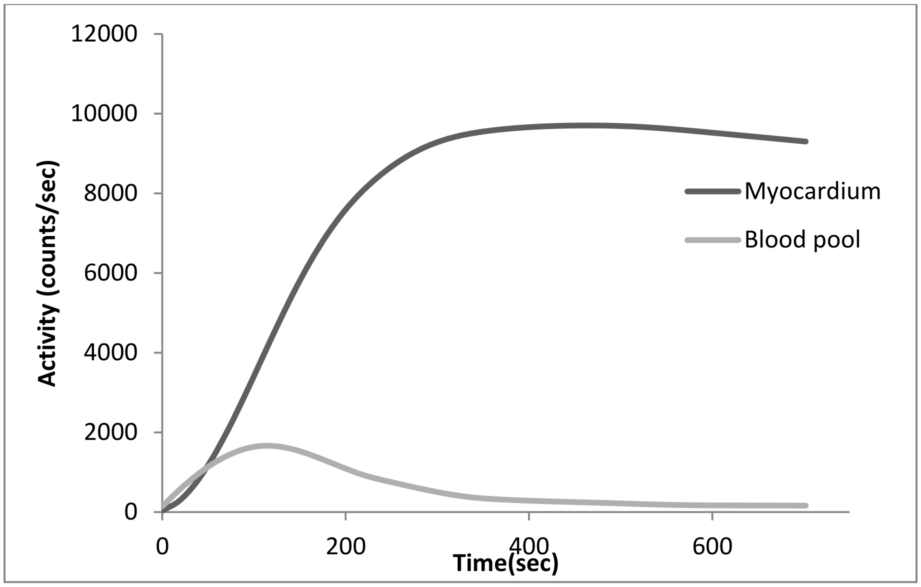

Figure 4- 3: Ground truth time activity curves for ^{201}TL for the myocardium and blood pool. These are the same blood pool and myocardium TACs as in Figure 4-2, but plotted with an expanded vertical scale.

4.2.2 Imaging Simulation

4.2.2.1 Phantom

Patient anatomy was modeled using the realistic 3D NCAT phantom [94]. In particular, we modeled the myocardium, blood pool, lungs, liver, kidneys, gall bladder, and background (i.e., body remainder). The activity distribution in each organ was assumed to be uniform except in the lungs, where activity was zero in airways.

4.2.2.2 Projection data generation

Noise free-projection data were generated for each of the six organs modeled including the background using an analytic projector that models attenuation, scatter and the collimator-detector response [75, 76, 95-97]. In these simulations the digitized representation of each organ was filled with unit total activity and a separate projection for each organ was generated. Projection data modeled acquisition with a two-camera system in a right angle configuration, a 20% wide energy window, 9% energy resolution, 4-mm intrinsic resolution, and LEHR collimators. Phantom projection data were generated using an analytic projector with a small projection bin size (.1562 cm) and a 256x256 matrix size and then collapsed to the assumed acquisition bin size of 0.312 cm and a 128x128 matrix size to model the continuous nature of the activity distribution in the body. We modeled fixed rotation with a distance from the center of rotation to the collimator face of 25 cm since body contouring orbits might not be feasible with the short acquisition durations used in this work.

A series of dynamic projection images were generated from the unit-activity projection data set for each organ described above. To do this, the unit-activity projections for each organ were scaled by the total organ activity for the corresponding organ at the time of the projection, and the projections for all the organs were summed to produce noise-free measured projection data.

To allow capture of the rapid uptake phase, we simulated a projection acquisition duration of 18-seconds. Step-and-shoot acquisition using such a short acquisition duration would result in a significant fraction of time being wasted on motion. As a result, we modeled continuous rotation instead. To model continuous rotation, projections were first generated at an angular increment of 3°. We modeled the variation in tracer uptake during projection acquisition by sampling the TACs at 6-second intervals for each such projection. Summing groups of 3 consecutive projections produced the final projections that corresponded to a 9°-angular increment between projections and an 18-second acquisition duration.

For experiments requiring noisy projections, noise was added to noise-free simulated data using a Poisson generated pseudo-random number generator. Since the simulation realistically modeled the sensitivity of the gamma camera and the activity in the various organs, the count levels in the simulation were appropriate for the specified acquisition duration and tracer kinetics. A total of 30 sets of noisy projection data were generated using independent sequences of random numbers in order to study both the bias and variance of estimates.

4.3.3 Estimation of activity from planar images

We used the previously developed the QPlanar method for estimating the activity in the organs or VOIs from planar projections. This method uses Poisson maximum-likelihood estimation techniques and accurate models of image formation to estimate the total activity in a set of 3D VOIs. In this study, we adapted this methodology to extract dynamic information, in the form of the time activity curves for the myocardium, blood pool and the other organs listed above, from a conventional SPECT acquisition.

4.3.3.1 QPlanar method

Given that the SPECT data are corrupted by noise that has a Poisson distribution, the use of the Poisson ML estimator in QPlanar method gives the minimum variance solution assuming that an unbiased solution exists. The QPlanar method was already introduced in Chapter 2 (section 2.2.4.2) of this thesis.

In this chapter, we once again adopted QPlanar methodology to extract dynamic information, in the form of the time activity curves for the myocardium, blood pool, lungs, liver, kidneys, gall bladder, and background (i.e., body remainder) from a conventional SPECT acquisition. Of particular importance is the application to pairs of planar projections acquired simultaneously in a perpendicular camera orientation.

In the QPlanar method, we used analytically generated projections (sec. 4.2.2.2) of the VOIs to form the projection matrix elements. The matrix elements in the QPlanar method included the effects of continuous rotation acquisition using the same method described above to generate the organ projections. In particular, we generated projections at an angular increment of 3° and summed over a 9 degree range to a single projection for a full camera rotation of 360°.

In this work, we assumed that the activity inside the VOIs was uniform, but this assumption is not essential [106]. For example, if a non-uniform background activity distribution were available at one time point from a SPECT image, it could be used in generating the projection matrix used in QPlanar. The assumption would then be that the activity distribution at other time points was proportional on a voxel-by-voxel basis to the activity distribution.

4.3.3.2 QPlanar method application

The experiment was carried out in 3 parts in order to assess various aspects of the estimation process. In all parts, the QPlanar method was applied to estimate the activity concentration in each organ in a set of 3D VOIs at each time point, thus creating estimated TACs directly from the projections. Part one involved assessing the activities over time in the myocardium and blood pool when the activity concentration inside each organ was uniform and Poisson noise was not simulated. In part two, we added Poisson noise to the projection data from part 1 to assess the effect of noise on the bias and precision of the estimated activities over time in the myocardium and blood pool. In part three, kinetic parameters were estimated from the TACs using the two-compartment model described above to assess blood flow in both noise-free and noisy cases.

4.5 Results

4.5.1 Accuracy

We first investigated the bias in TACs using noise-free data for the ideal case where the myocardial activity distribution was uniform. Figure 4-4 shows plots of the estimated and true TACs of the myocardium and blood pool from noise-free data using the QPlanar estimation method. The difference between these two TACs is also shown. Note that, for the myocardium, the bias was consistently low compared to blood pool. For the blood pool, there was a somewhat larger bias at early time points due to the rapid change of tracer concentration in the region relative to the acquisition duration as a result of dynamic changes in tracer uptake during the acquisition. However, the bias was very low at times where the TAC was changing slowly relative to the projection duration of 18 seconds. An optimized time interval appropriate for the tracer used would likely reduce this early bias. The maximum percent biases for the heart and blood were 2.8% and 1.3%, respectively. In both cases the minimum percent bias was approximately 0%.

These data demonstrate that the task of estimating the activity from 2 orthogonal planar projections, given the exact 3D VOIs and assuming uniform activity in the VOIs, is feasible and provides accurate estimates using continuous rotation and reduces biases in the case of both myocardium and blood pool when compared to continuous rotation modeling.

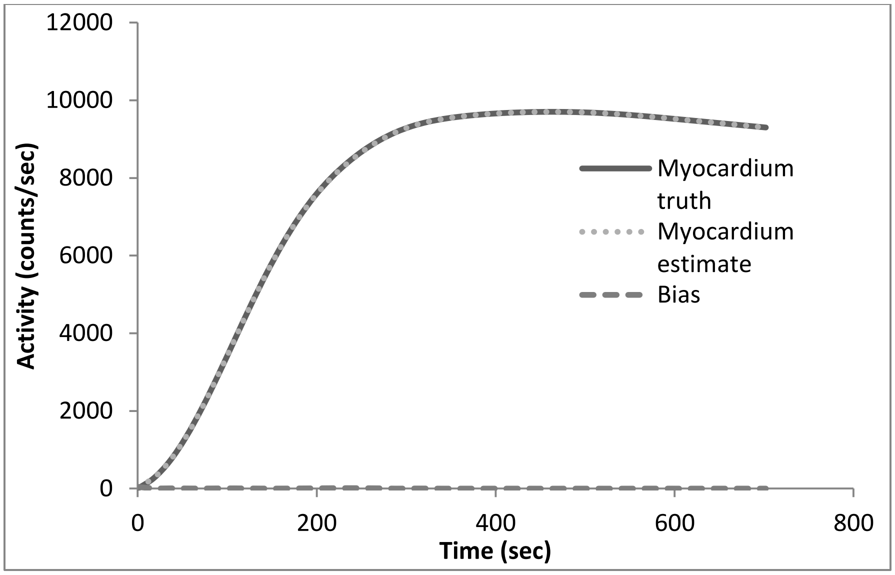

Figure 4- 4: Comparison of the ground-truth TAC and TAC estimated from noise-free data for the myocardium. Bias is the difference between the TAC estimated from noise-free data and the ground truth TAC.

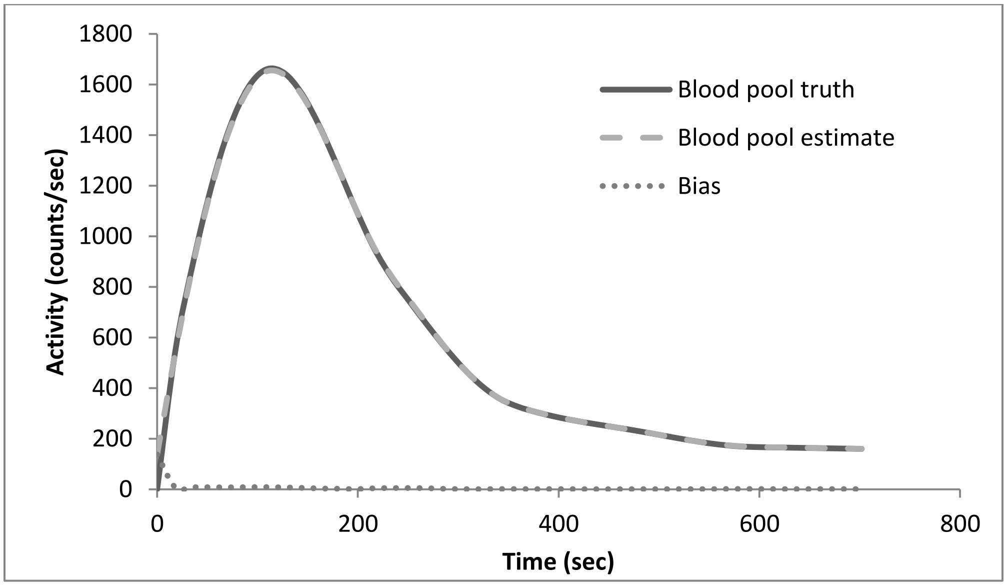

Figure 4- 5: Plot of TAC of the blood pool estimated from noise-free data compared to the true blood TAC. Bias is the difference between the TAC estimated from noise-free data and ground truth TAC.

4.5.2 Precision

To investigate the noise characteristics, we estimated TACs from 30 sets of projection data with simulated Poisson noise. Figures 4-6 and 4-7 show plots of the means and standard deviations of the TACs of the blood pool and myocardium compared to the TAC from noise-free data. The difference between the mean and noise-free TACs is also shown.

These data demonstrate that using noise-free data is a suitable proxy for investigating bias. The weighted average absolute biases (defined in chapter 3, sec. 3.2.4, eq.3) for the myocardium and blood pool were 1.5% and 14.7%, similar to the values obtained from the noise-free data. In combination, the data from Figures 4-4 and 4-5, which showed the biases estimated from noise-free data, and Figures 4-6 and 4-7 demonstrate that the method produces relatively unbiased TACs when the assumptions of the method are met, i.e., the ideal VOI boundaries are known and the activity distributions inside the VOIs are uniform. The magnitude of the standard deviations in Figures 4-6 and 4-7 indicate the sensitivity of the TAC estimates to noise. The average weighted COVs were <1% and <3.5% for the heart and blood-pool TACs, respectively. Here the COVs at each time point were weighted by the mean value of the TAC at that time point. The comparison of the TACs estimated from noise-free data to the mean illustrates that fact that the TACs estimated from the noise-free data is a good proxy for the mean. Figure 4-8 shows examples of myocardial and blood pool TACs from a single noise realization. It can be seen that the later time points show less activity as the tracer washes out but the noise at later time points result in larger relative variations in the activity estimates.

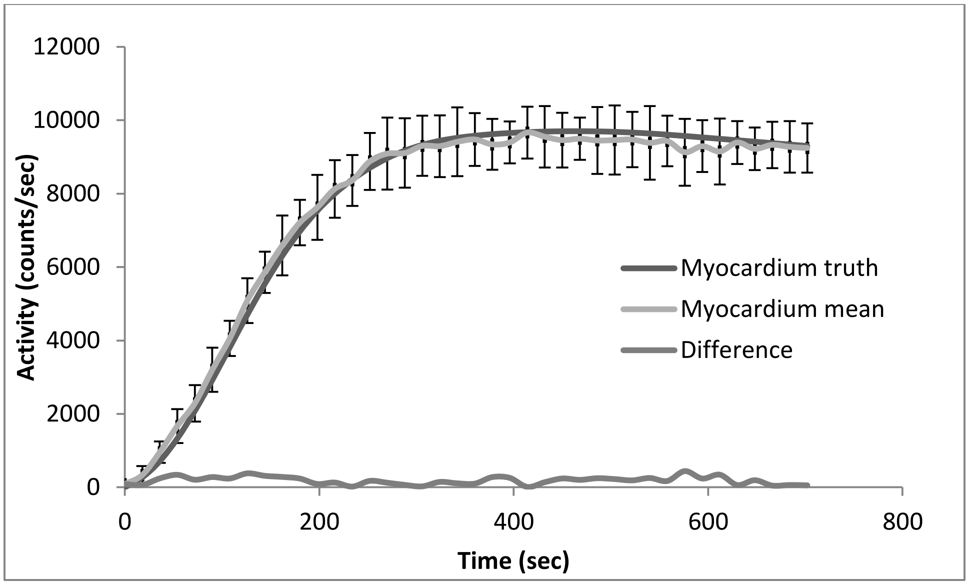

Figure 4- 6: Plot of TAC of myocardium estimated from noisy data compared to the noise-free myocardium estimate.

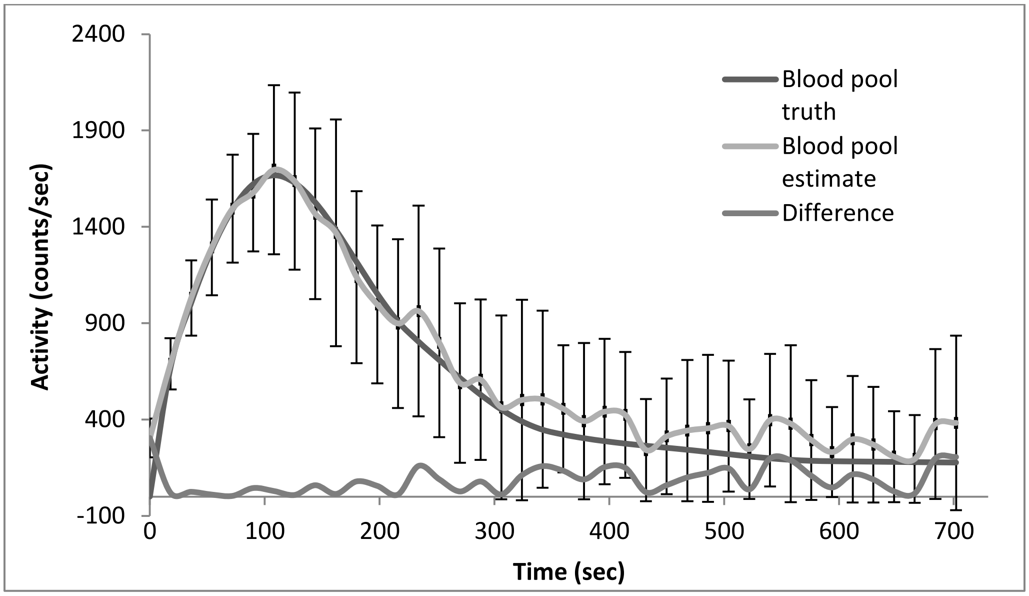

Figure 4- 7: Plot of TAC of blood pool estimated from noisy data compared to the noise-free blood pool estimate.

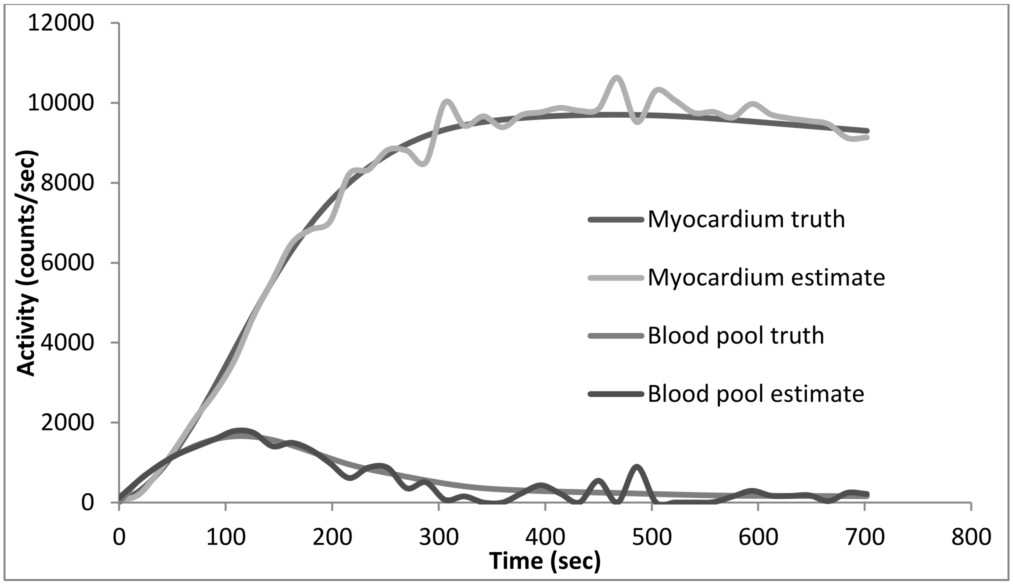

Figure 4- 8: Plot of TAC of blood pool estimated from noisy data compared to the true blood pool.

4.5.3 Estimation of global kinetic parameters

Table 4-3 shows comparisons of the values of k_{21} and k_{12} estimated for the myocardial VOI obtained from the TAC estimated from noise-free data. Gold-standard parameters were obtained from fitting the ground-truth TACs of the myocardium and blood pool.

The Levenberg-Marquardt [36, 37] least squares fitting routine from the Matlab signal processing toolbox was used to estimate k_{21} and k_{12}. The estimated values for both parameters are shown in Table 4-3, and both differed from the gold standard by <1%.

Table 4- 3: Estimates of k_{21} (wash-in) and k_{12} (wash-out) estimates from noise-free data.

Parameters	Gold	Estimated	% bias	Units
k_{21}	.5538	.5561	.4	ml/min/gm
k_{12}	.1265	.1277	.9	ml/min

Figure 4-9 is a box and whisker plot of the estimates of k_{21} and k_{12} for the noise-added case. Again, the Levenberg-Marquardt [36, 37] implementation of the fitting program using Matlab signal processing toolbox produced k_{21} estimates with a bias of 3% and k_{12} estimates with a bias of 47%. The large bias of k_{12} could be possibly due to parameter estimation local minima problem. Table 4-4 summarizes the data from Figure 4-9 by providing percent errors of the parameter values compared to ground truth.

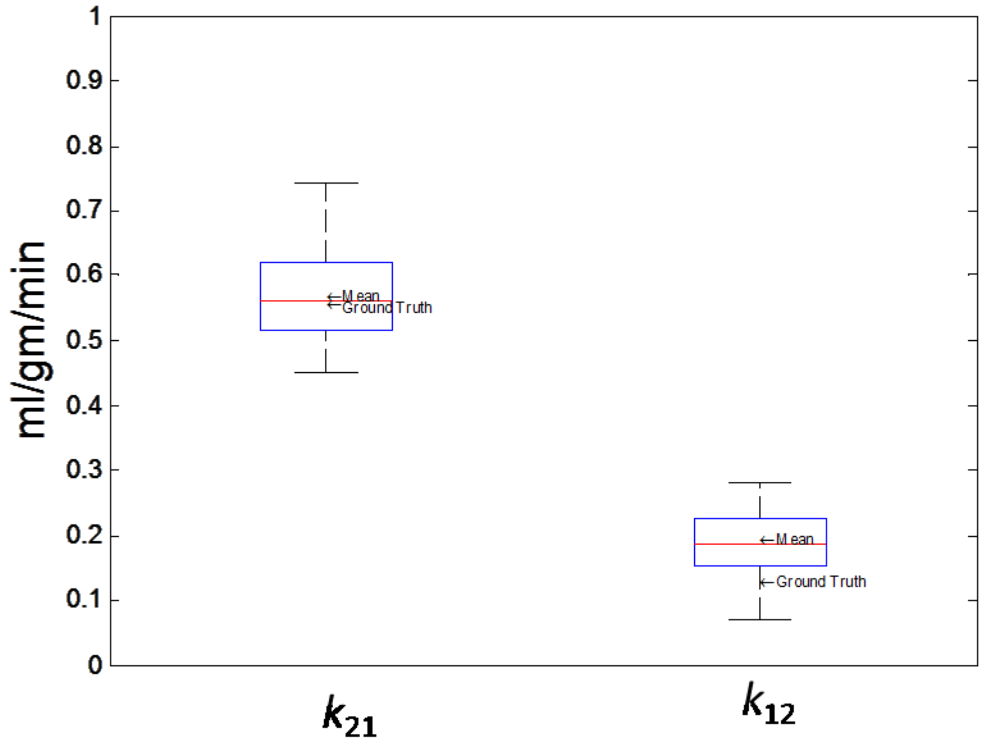

Figure 4- 9: Box plot of mean wash-in (k_{21}) and wash-out (k_{12}) values estimated from 30 noise realization of myocardium and blood pool TACs.

Table 4- 4: Estimates of k_{21} (wash-in) and k_{12} (wash-out) estimates from noise-free data.

Parameters	Gold	Estimated mean	% bias	COV
k_{21}	.5538	.5699	2.9	.0051
k_{12}	.1265	.1862	47	.0034

4.6 Discussion

One of the advantages of acquiring the data while rotating is that it allows for reconstruction of SPECT images at later time points when the activity distribution is not changing rapidly. These images could be useful in defining VOIs necessary for the QPlanar activity estimation.

Continuous rotation acquisition also allowed us to obtain accurate global kinetic parameters, given that exact VOI location is known and activities in the VOIs are uniformly distributed in the noise free case. Kinetic parameters of wash-in rate or global flow (k_{21}) and wash-out rate (k_{12}) were estimated to a bias of 1% in the noise-free data.

For the case of the noise added data, we observed the mean myocardium TACs showed a slight bias in post uptake phases of the TACs. One possible reason for this is simply not having a large enough number of noise realizations. If true, the estimate of the bias could be simply reduced by averaging a higher number of estimates (>300). The mean TACs in the myocardium and blood pool showed good agreement with the truth (the weighted average absolute biases, weighted by total activity in the VOIs, for heart and blood pool were 1.5% and 14.7%). These data demonstrate that it is possible to obtain good estimates of the myocardial TACs when the true organ VOIs were known and the activity distributions in the organ were uniform in noisy data.

In the noise added case, the global kinetic parameters of wash-in rate (k_{21}) were estimated to be to have a bias of 3%. However, the wash-out rate (k_{12}) parameters had a bias of 47%. The large inaccuracies for the wash-out were likely due to the large noise fluctuations in the estimated TACs, especially at later times. This could be exacerbated by failure to reach the global minimum of the least squares objective function. One way to avoid local minima is to simply start with a set of different initial estimates and perform the parameter estimation a number of times, using the parameter value that gave the overall lowest value as the global minimum. This could potentially the decrease the large bias of k_{12}. However, since the goal of this work was to estimate flow, the large errors in the wash-out rate parameters may not be as important. This is evident by the fact that, regardless of a large bias in k_{12}, the mean estimated MBF was0.73 (ml/min/gm). When compared to ground truth MBF (0.71 (ml/min/gm) this is equivalent to a % bias of <3%. What about the precision. I would give the mean and standard deviation of the estimated MBF (might give the COV of the MBF).

A significant limitation of the study presented in this chapter is that there was no object model mismatch. In other words, it was assumed that the true, high-resolution VOIs were known. In practice these would not be known. The effects of model mismatch will be addressed in Chapter 5.

5.0 Effects of model mismatch

5.1 Introduction

In this chapter, we will be introducing a concept known as object model mismatch. In the previous simulations, the VOIs used in the estimation were the same as the actual organ volumes. However, in practice, it would be impossible to know the true VOIs. The difference between the assumed and true VOIs is a kind of object model mismatch. In the work in this chapter, we model various kinds of object model mismatch and explore the effects of object model mismatch on estimated TACs and kinetic parameters. Because of object model mismatch, bias of the estimated TACs compared to truth is likely to be increased. Object model mismatch should be considered in realistic simulations as it will be present to some degree for real patient scans.

In the previous chapters, we assumed the ideal case where the true VOIs were known. With this assumption, we found that the use of continuous rotation acquisition protocols resulted in a very accurate estimate of the kinetic parameters in the case of noise-free data and in absence of object model mismatch. However, in a realistic situation, various kinds of model mismatch will occur due to non-uniformty of the activity distribution in VOIs, and especially the background, the inability to include all VOIS, such as the right ventricle, as part of the object model for the SPECT images.

There are various types of object model mismatch. In the context of this work, object model mismatch refers to differences in the true and assumed VOIs as well as the assumed uniform activity distribution inside the VOIs. We will explore object model mismatch, i.e., using a VOI in the estimation process that differs from the true VOI. This kind of mismatch can, as will be shown below, result in bias in activity estimates. Other kinds of model mismatch include the assumption that the activity distribution is static during the acquisition of each projection view.

One source of object model mismatch includes violation of the assumption of uniform activity distribution in one or more VOIs. Because the QPlanar method assumes activity distributions in the VOIs are uniform, the presence of non-uniform uptake in a VOI violates this assumption and is a form of object model mismatch [104]. In this chapter we investigated three specific types of object model mismatch. First, the myocardial VOI did not include the right ventricle, which was not accounted for previously in background. Instead of including the RV VOI as part of the myocardial VOI (comprised of the Left Ventricle and Right Ventricle VOIs), it was included in the background VOI when estimating the VOI activities. We will call this type of object model mismatch **RV VOI mismatch**. Second, we dilated the left ventricle (DLV) (and modified the liver, lung, and blood pool, and background VOIs to account for this.. We will call this type of object model mismatch **DLV VOI mismatch**. In the third case of object model mismatch, we introduced randomly sampled errors in the dilated portion of the DLV VOIs. This models random errors in defining VOIs and demonstrates the effect of such errors on the accuracy of activity estimation. We will call this type of object model mismatch **Random Error DLV VOI mismatch**. In this chapter, we investigated the effects of RV VOI, DLV VOI and

Random Error DLV VOI mismatch on the estimation of TACs and global kinetic parameters in terms of bias and variances.

5.2 Methods

We applied two methods to estimate VOI activities in the presence of object model mismatch: the QPlanar method, which has been previous described in Chapter 2, section 2.2.4.2, and a Direct Matrix Inversion (DMI) method. Details of the DMI method and its strengths and weakness compared to the QPlanar method are discussed below.

5.2.1 Direct Matrix Inversion (DMI)

The need for DMI results from computational limitations of the QPlanar method when applied to very large numbers of images. The QPlanar method requires a much longer time than DMI to estimate the activity accurately because it requires many iterations to converge. In some cases, we observed that >10,000 iterations were required. While this still takes a relatively modest amount of time (approximately 1 sec. per sample), when investigating multiple noise realizations and a large number of time points it is computationally very challenging to use.

However, the QPlanar method is desirable as it explicitly takes into account the Poisson distribution of the projection data, which results in a natural non-negativity constraint on the estimated VOI activities. As an ML method it is also guaranteed to find the minimum variance solution if an unbiased solution exists. In contrast, the DMI method implicitly assumes a Gaussian distribution of the data and does not enforce non-negativity. However, DMI is substantially faster, and this is particularly useful when estimating TAC values for a large number of noise realizations or various kinds of model mismatch. The following is a description of the DMI method.

Let the measured projection data be defined as

$$\boldsymbol{Y} = [y_1, y_2, \ldots, y_M] \in \mathbf{N}^{M\,X1}, \tag{5.1}$$

where, y_i is the counts in the *i*th projection bin. The elements of $\boldsymbol{Y}$ follow independent Poisson distributions, and *M* is the number of projection bins.

Let $\mathbf{a}_{\mathrm{t}} \in \mathbf{R}^{\mathrm{N\,X1}}$ be a vector defining the true mean number of decays in the VOIs, where the j^{th} element of $\boldsymbol{a_t}$ is the true expected number of decays in the j^{th} VOI, and the subscript 't' denotes the true number of decays.

The mean projection data are given by

$$\mathbf{E}[\boldsymbol{y}] = \mathbf{P_t a_t}, \tag{5.2}$$

where, E[·] denotes ensemble mean and $\mathbf{P}_t \in \mathbf{R}^{N\,X1}$ denotes the true system matrix. For the simulation presented here, the true system matrix $\boldsymbol{P}_{\mathrm{t}}$, contains projections of the true unit-activity VOIs. The element in the i^{th} row and the j^{th} column of the true system matrix is the probability that a photon is detected in projection bin *i* for a single decay in the j^{th} VOI. Thus the true system matrix also exactly represents all of the effects of the image formation process including photon abundance, system sensitivity, object scatter and attenuation, and collimator–detector interactions.

Estimating the vector of activities requires an estimate of the system matrix. The matrix, $\boldsymbol{P}_{\mathrm{e}}$, is the estimated system matrix, which contains the projections of the VOIs used in the estimation process. Also in practice, the system matrix is not precisely known, and a model of the image formation process is incorporated into a forward projection code to model various image degrading effects. This forward projection process implicitly involves a system matrix, $\boldsymbol{P}_{\mathrm{e}}$. Because computation time is of concern in practice, some approximations and simplifications are typically made in the model and the forward projection code to speed up the computation [107].

In the case under consideration here, the mistmatch between the true and estimated system matrix is due to mismatch in the true VOIs and the VOIs used in the estimation process, which are used in the generation of $\boldsymbol{P}_{\mathrm{e}}$.

We define the model-mismatch between the true and estimated system matrix as follows:

$$\Delta\mathbf{P} = \mathbf{P}_e - \mathbf{P}_t. \tag{5.3}$$

In the following section we will investigate how this model-mismatch affects the activity estimates. Suppose $\boldsymbol{a} \in \mathbf{R}^{NX1}$ denotes the expected number of decays in the VOIs, the maximum likelihood estimate of $\boldsymbol{a}$ is found by maximizing the following log-likelihood function, where Pr is the probability:

$$\mathbf{a}_e = \arg\ \max\ \{\ln[\Pr(\mathrm{y}|\mathbf{a})]\}. \tag{5.4}$$

Since the projection data, $\boldsymbol{y}$, follow an independent Poisson distribution, we have

$$\ln[\Pr(\mathrm{y}|\mathbf{a})]=\sum_{j=1}^{M}\{y_i \ln[(\mathbf{P_e a})_j] - (\mathbf{P_e a})_j - \ln(y_j!)\}, \tag{5.5}$$

where, y_j and $(\boldsymbol{P_e a})_j$ denote the j^{th} element of y and $\boldsymbol{P_e}\,\boldsymbol{a}$, respectively. Here note that we use the model-estimated system matrix, $\boldsymbol{P}_e$, in the estimation process. A closed form solution to equation (5.5) is not available. However, when the number of photon counts per projection data bin is larger than 10, it is an excellent approximation to assume that $\boldsymbol{y}$ follows a Gaussian distribution with variance equal to the mean. Thus, finding the maximum likelihood estimator is equivalent to solving a weighted least-squares problem [108-110]. This can be solved in matrix form using:

$$\mathbf{P}_e^T \mathbf{B} \mathbf{P}_e a_e = \mathbf{P_e}^T \mathbf{B} y, \tag{5.6}$$

where, the diagonal matrix $\mathbf{B} = diag\{\frac{1}{E[y_i]}\} \in \mathbf{R}^{MXM}$,

is the inverse of the covariance matrix of the projection data [111]. To avoid division by a small number, we set $\frac{1}{E[y_i]}$ to be 0 if $E[y_i] < 1$.

Note that, by definition and the linearity of the projection process given in eq. 5.2, and eq. 5.6, we can derive equations for calculating the bias and the covariance matrix of $\boldsymbol{a}_e$ as follows:

$$
\begin{aligned}
Bias(\mathbf{a}_e) &= E[\mathbf{a}_e] - \mathbf{a}_t \\
&= (\mathbf{P}_e^T \mathbf{B} \mathbf{P}_\mathbf{e})^{-1}.\mathbf{P}_e^T \mathbf{B}.E[y] - \mathbf{a}_t
\end{aligned}
$$

Substituing E[y]:

$$
\begin{aligned}
(\mathbf{P}_\mathbf{e}^\mathbf{T} \mathbf{B} \mathbf{P}_\mathbf{e})^{-1}.\mathbf{P}_e^T \mathbf{B}.\mathbf{P}_t \mathbf{a}_t - \mathbf{a}_t &= (\mathbf{P}_e^T \mathbf{B} \mathbf{P}_e)^{-1}.\mathbf{P}_e^T \mathbf{B}.\mathbf{P}_t \mathbf{a}_t - (\mathbf{P}_e^T \mathbf{B} \mathbf{P}_e)^{-1}.\mathbf{P}_e^T \mathbf{B}.\mathbf{P}_e \mathbf{a}_t \\
(\mathbf{P}_e^T \mathbf{B} \mathbf{P}_e)^{-1}.\mathbf{P}_e^T \mathbf{B}.(\mathbf{P}_t - \mathbf{P}_e)\mathbf{a}_t &= -(\mathbf{P}_e^T \mathbf{B} \mathbf{P}_e)^{-1}.\mathbf{P}_e^T \mathbf{B}.\Delta \mathbf{P} \mathbf{a}_t
\end{aligned}
$$

$$
\begin{aligned}
Cov(\mathbf{a}_e) &\equiv E[(\mathbf{a}_e - E[\mathbf{a}_e])(\mathbf{a}_e - E[\mathbf{a}_e])^T] \\
&= (\mathbf{P}_e^T \mathbf{B} \mathbf{P}_e)^{-1}.\mathbf{P}_e^T \mathbf{B}.Cov(y).\mathbf{B} \mathbf{P}_e (\mathbf{P}_e^T \mathbf{B} \mathbf{P}_e)^{-1} \\
&= (\mathbf{P}_e^T \mathbf{B} \mathbf{P}_e)^{-1}.\mathbf{P}_e^T \mathbf{B}.\mathbf{B}^{-1} \mathbf{B} \mathbf{P}_e (\mathbf{P}_e^T \mathbf{B} \mathbf{P}_e)^{-1} \\
&= (\mathbf{P}_e^T \mathbf{B} \mathbf{P}_e)^{-1}.
\end{aligned}
$$

Note the direct effect of the model-mismatch, ΔP, on the bias of the estimates. When $\mathbf{P}_e^T \mathbf{B} \mathbf{P}_e$ is not invertible, singular value decomposition can be used to calculate its pseudo-inverse [112]. Noting that $\mathbf{a}_e = [\mathbf{A}_t.t] \in R^{N\,X1}$, where, *t* is the imaging time per projection view, we have

$$Bias(\mathbf{A}_i) = \frac{1}{t}.[Bias(\mathbf{a}_e)]_i, \tag{5.7}$$

$$Variance\ (\mathbf{A}_i) = \frac{1}{t^2}.[Cov(\mathbf{a}_e)]_{ii}, \tag{5.8}$$

where, $[\text{Bias}(\boldsymbol{a}_\text{e})]_i$ is the *i*th element of Bias($\boldsymbol{a}_\text{e}$) and $[\text{Cov}(\boldsymbol{a}_\text{e})]_{ii}$ is the *i*th diagonal element of Cov($\boldsymbol{a}_\text{e}$).

5.2.2 Model-mismatched projection data generation

Earlier we introduced three types of object model mismatch referred to as RV VOI mismatch, DLV VOI mismatch and Random Error DLV VOI mismatch. Here we will briefly discuss generating projection data for each case. In all cases, when generating projection data, it is assumed that the activity concentration in the RV (right ventricle) should be the same as in the LV (left ventricle) of the myocardium. In case of the DLV VOI mismatch, we dilated the left ventricle by one pixel before the projections of the VOIs were generated. In the case of Random Error DLV VOI mismatch, we modeled random variation of the VOI as follows.

First, the left ventricle was dilated by 1 voxel. Voxels in the region outside the true myocardial VOI were in the dilated VOI and were randomly included in the VOI used to estimate activities in order to simulate random manual or semi-automatic segmentation errors.

The amount of mismatch between the true and perturbed VOIs was controlled by the fraction of voxels in the dilated region that were randomly included in the VOI, referred to as the inclusion fraction. This was implemented by first dilating the myocardial VOI by 1 pixel in all direction. Each voxel in the dilated region was randomly sampled for inclusion into the final VOI. The probability that each voxel was included was defined by an inclusion factor: an inclusion factor of 0 indicates that the final VOI is equal to the true VOI; an inclusion factor of 100% indicates that all of the voxels in the dilated region would be included in the final VOI, and thus that model mismatch would be the largest.

5.3 Results

5.3.1 Effects of model mismatch on accuracy

We investigated the bias in TACs using noise-free data in the case of RV VOI object model-mismatch with continuous rotation where the right ventricle was modeled in the data but included in the background VOI (and not the myocardial VOI). Figures 5-1 and 5-2 show plots of the estimated and true TACs of the myocardium and blood pool from noise-free data. The difference between these two TACs is also shown.

The average weighted absolute biases for heart and blood pool were 5% and 162%, respectively over all time points. The maximum percent biases over all time points for heart and blood were 12% and over 100%, respectively. The minimum absolute (absolute value) percent bias over all time points for heart and blood were approximately 0% and 10%, respectively. One effect of object model mismatch is that there were large biases in the blood pool estimate evident during the uptake phase. One possible cause is that the bias due to object model mismatch is angular dependent. Since time and projection angle are correlated for a continuous rotation acquisition, the angle-dependent bias will result in time-dependent bias when kinetic parameters are estimated from the TAC. This could have a negative effect on the accuracy of these parameters.

The data above suggested that the bias depended on the projection angle. Thus, we looked for the projection views that had the lowest bias and variance, with the intent of acquiring the complete dynamic data with the cameras fixed at that pair of views. The right ventricle was again not included in the myocardial VOI for this analysis. Figure 5-3 shows the RMSE value as a function of the view angle for the first camera over all time points; the second camera had a view angle 90° greater than this. The pair of orthogonal view angles that gave the lowest RMSE over all time points are illustrated in Figure 5-4. This set of angles was selected to use for static (non-rotating) acquisition in order to eliminate the potential for angular-dependent bias, variance and provide the minimum overall bias and variance.

Figures 5-5 and 5-6 show plots of the estimated and true TACs of the myocardium and blood pool from noise-free data for the pair of angles that gave the lowest RMSE over all time points. The difference between these two TACs is also shown. For the myocardium, the bias was consistently low for all time points. For the blood pool, there was a somewhat larger bias at later time points, likely due to the activity in the blood pool. The average weighted absolute biases for heart and blood pool were 1% and 22.8%, respectively, in the case of static acquisition with this pair of projection angles. The maximum percent biases over all time points for heart and blood were 1% and 104%, respectively. In both cases the minimum percent bias was approximately 0%. Note that while there is some bias, and this bias does depend on time, it changes slowly compared to the case of continuous rotation. These data demonstrate that estimating activity from two orthogonal planar projections is desirable in the presence of RV VOI model mismatch. Further, it suggests that the acquiring data at this fixed angle will be superior in terms of the accuracy of the estimated kinetic parameters.

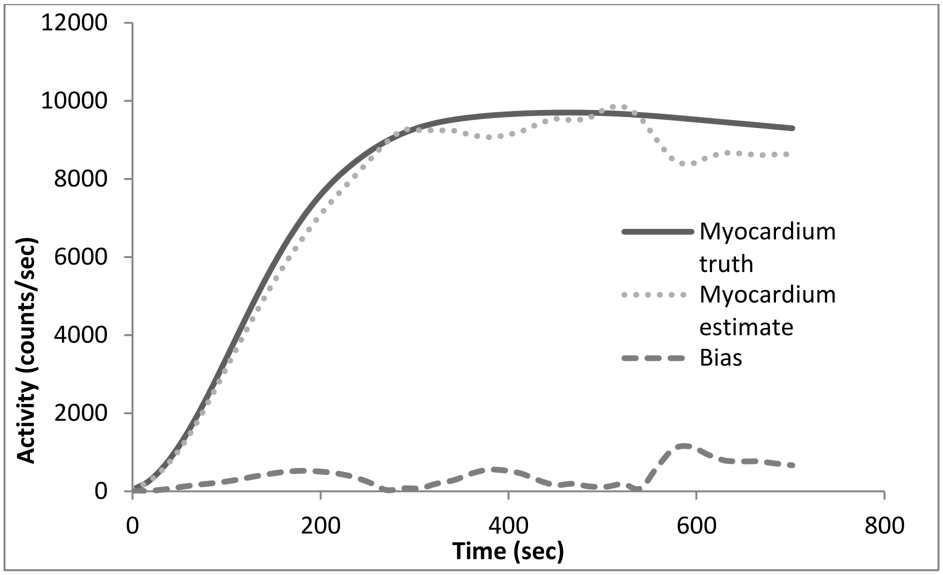

Figure 5- 1: Plots of the estimated and true TACs of the myocardium from noise-free data with continuous rotation data acquisition with RV VOI mismatch.

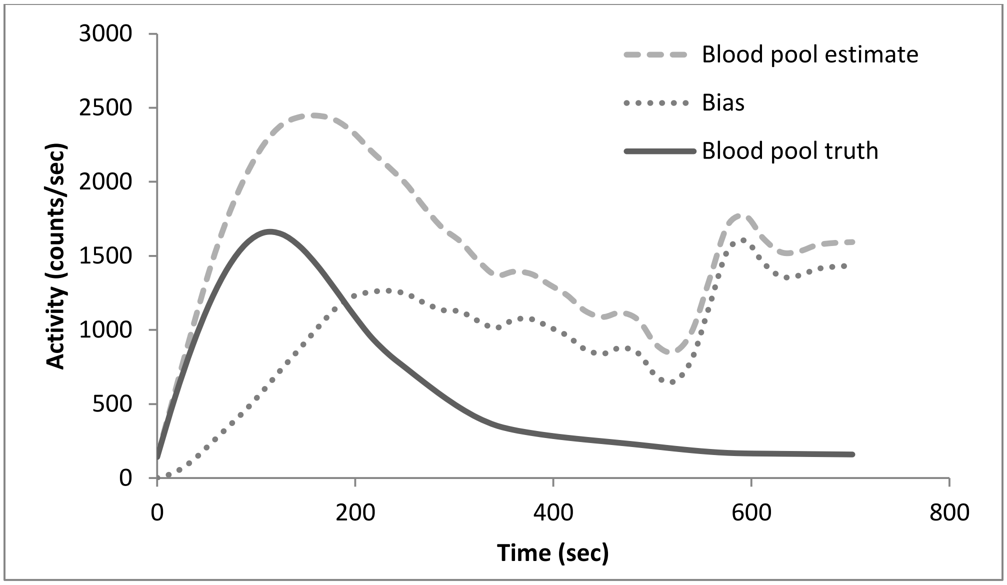

Figure 5- 2: Plots of the estimated and true TACs of the blood pool from noise-free data with continuous rotation data acquisition with RV VOI mismatch.

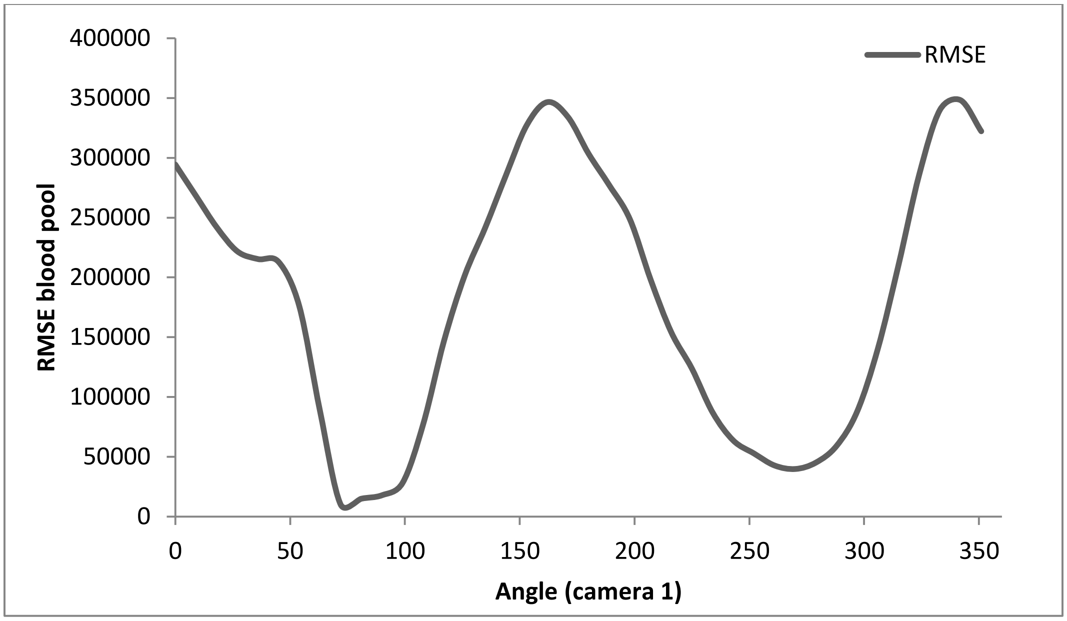

Figure 5- 3: Plots of the RMSE of the blood pool TAC from noise-free data with static data acquisition over all time points.

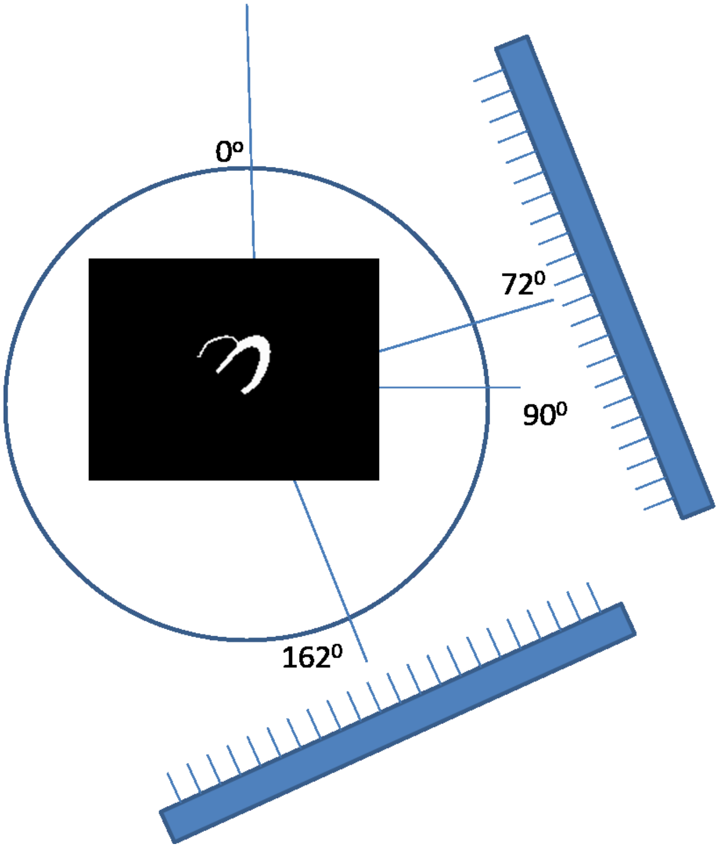

Figure 5- 4: Diagram of optimal view angle (72⁰,162⁰) for static data acquisition determined by RMSE plot.

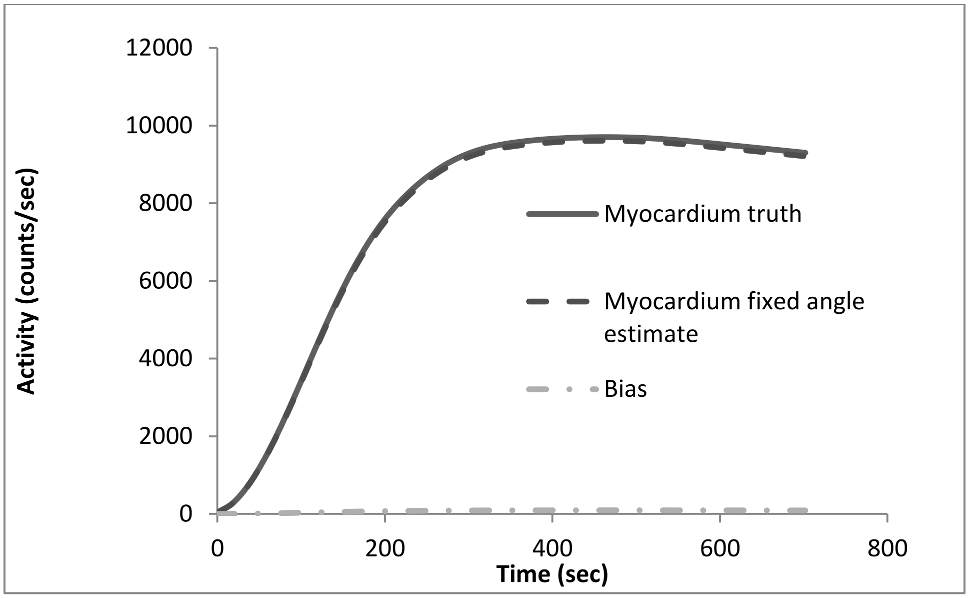

Figure 5- 5: Plots of the estimated and true TACs of the myocardium from noise-free data with static data acquisition with RV VOI mismatch where all projections are acquired at the optimal projection angle.

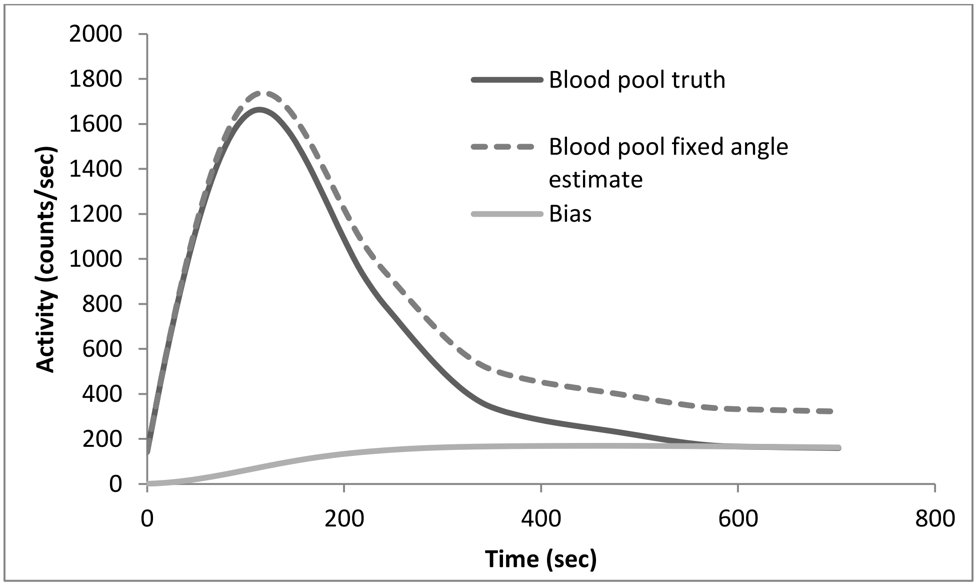

Figure 5- 6: Plots of the estimated and true TACs of the blood pool from noise-free data with static data acquisition with RV VOI mismatch where all projections are acquired at the optimal projection angle.

In the case of Random Error DLV mismatch, we investigated five different inclusions fractions: 0% (corresponding to use of the true VOI), 25%, 50%, 75%, and 100%. The 100% case represented the largest error in the VOI, i.e., when all the voxels in the dilated volume were included from the dilated VOI. The 100% case is also known as DLV ROI object model mismatch and was discussed above.

Acquisition at the fixed pair of orthogonal view angles described above (72°, 162°) was modeled to investigate effects of Random Error DLV mismatch. Figures 5-7 and -8 show plots of the estimated and true TACs of the myocardium and blood pool from noise-free data in the case of a 0% inclusion fraction, which is equivalent to the true VOI. The difference between these two TACs is also shown. Figures 5-9, -10, -11, -12, -13, -14, -15 and -16 show plots of the estimated TACs for the myocardium and blood pool corresponding to inclusion fractions of 0, 25, 50, 75 and 100%, respectively. Table 5-1, below shows the average weighted absolute biases for heart and blood pool for the above cases of inclusion fraction.

Table 5- 1: Average weighted absolute bias of heart and blood pool corresponding to inclusion fractions (IF) of 0, 25, 50, 75 and 100%.

Model mismatch type	Average weighted abs. bias	
	Heart	Blood pool
Random Error DLV, IF= 0%	0%	0%
Random Error DLV, IF=25%	.2%	1.5%
Random Error DLV, IF=50%	.4%	3.4%
Random Error DLV, IF=75%	.6%	5%
Random Error DLV IF=100%	.9%	6.8%

The data in Table 5-1 demonstrates that the task of estimating activity from 2 orthogonal planar projections is very feasible and provides accurate estimates if VOIs can be defined to within 1 voxel larger than the true boundary.

Figure 5.17, shows the RMSE for the blood pool with static data acquisition at the optimal angle as a function of the inclusion fraction for voxels in the dilated myocardial region. An inclusion factor of 100% represents the maximum model mismatch and is the case where the VOI used in estimation is the true VOI dilated by 1 voxel in all directions. We show the blood pool RMSE since, ultimately, accurate estimation of kinetic parameters are dependent on accuracy of blood pool activity estimation. As expected, we observed that the highest RMSE value was attained when 100% of the voxels in the dilated region were included in the myocardial VOI used for activity estimation. Figure 5.18, shows the average percent bias for the blood pool, and shows a similar trend as the RMSE.

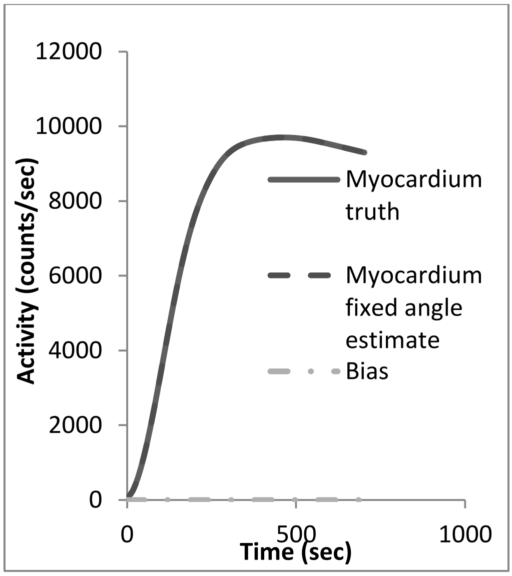

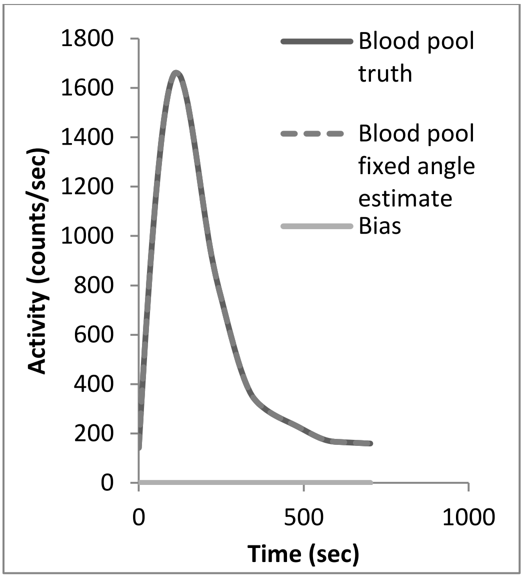

Figure 5- 7: Plots (left side) of the estimated and true TACs of the myocardium from noise-free data with static data acquisition of the dilated heart in the case of 0% inclusion.

Figure 5- 8: Plots (right side) of the estimated and true TACs of the blood pool from noise-free data with static data acquisition of the dilated blood pool in the case of 0% inclusion.

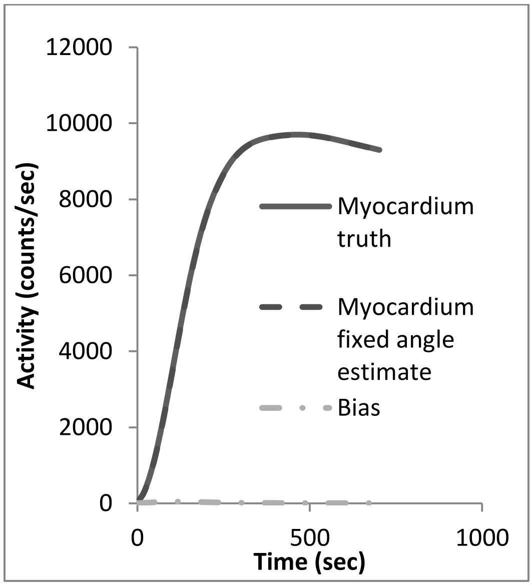

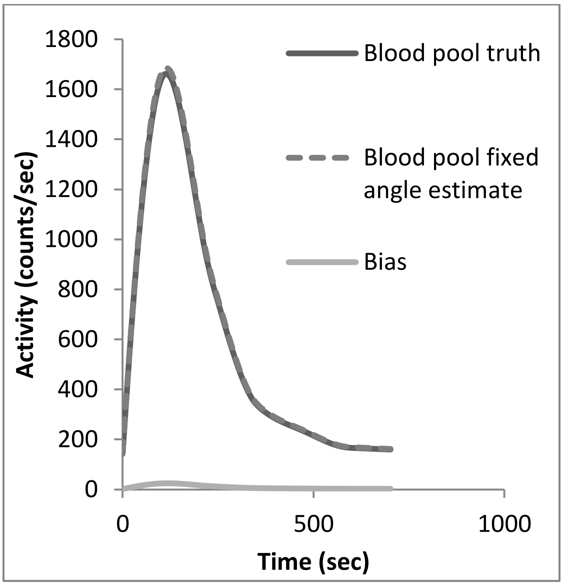

Figure 5- 9: Plots (left side) of the estimated and true TACs of the myocardium from noise-free data with static data acquisition of the dilated myocardium in the case of 25% inclusion.

Figure 5- 10: Plots (right side) of the estimated and true TACs of the blood pool from noise-free data with static data acquisition of the dilated blood pool in the case of 25% inclusion.

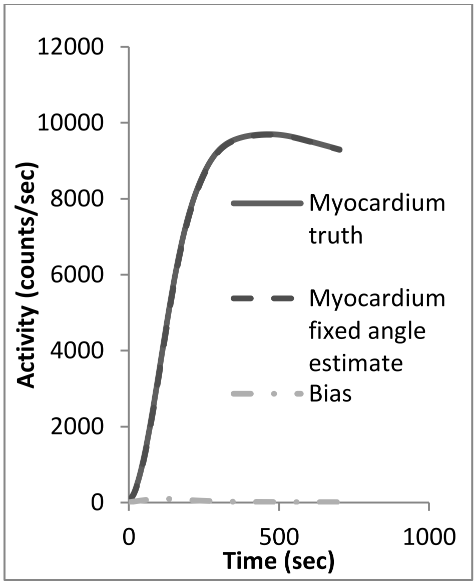

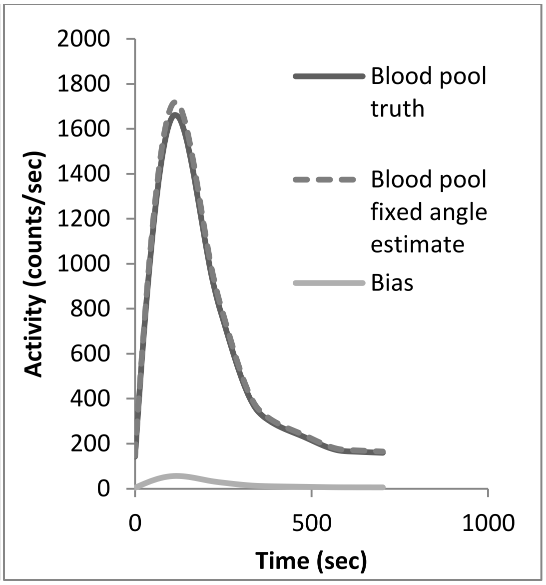

Figure 5- 11: Plots (left side) of the estimated and true TACs of the myocardium from noise-free data with static data acquisition of the dilated myocardium in the case of 50% inclusion.

Figure 5- 12: Plots (right side) of the estimated and true TACs of the blood pool from noise-free data with static data acquisition of the dilated blood pool in the case of 50% inclusion.

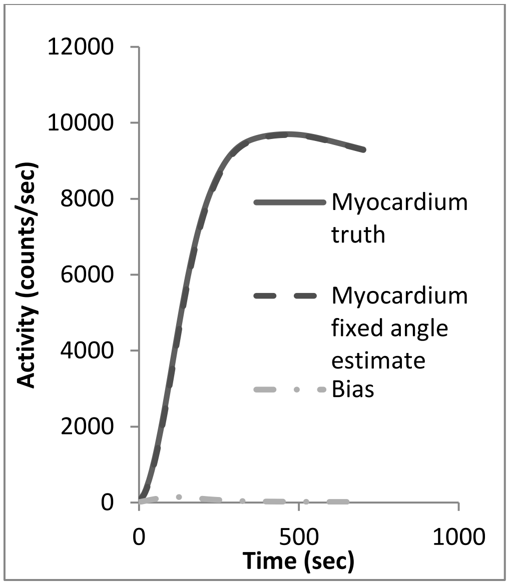

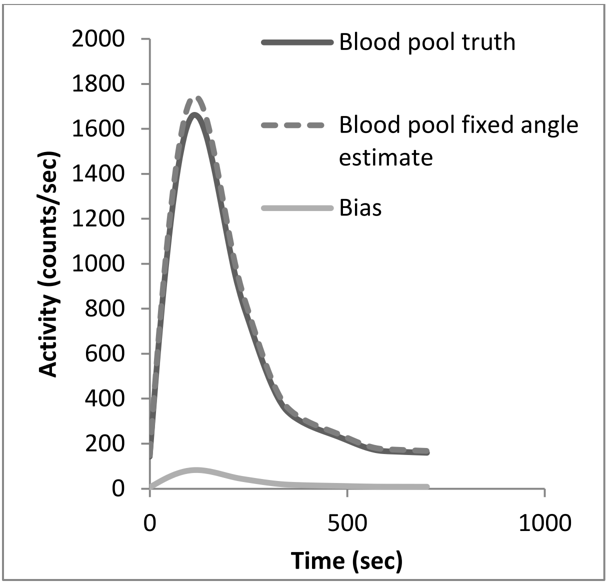

Figure 5- 13: Plots (left side) of the estimated and true TACs of the myocardium from noise-free data with static data acquisition of the dilated myocardium in the case of 75% inclusion.

Figure 5- 14: Plots (right side) of the estimated and true TACs of the blood pool from noise-free data with static data acquisition of the dilated blood pool in the case of 75% inclusion.

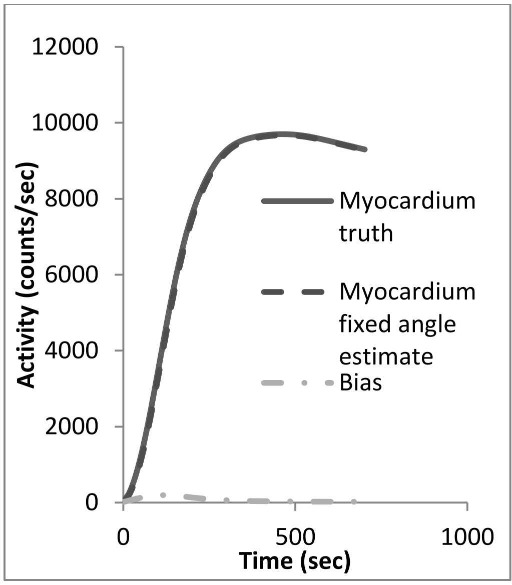

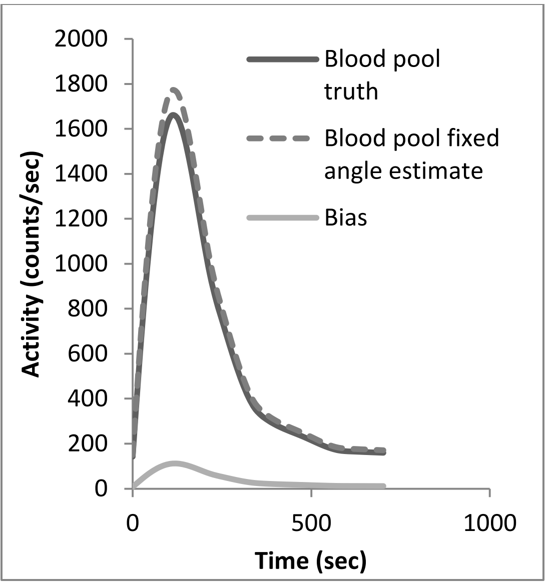

Figure 5- 15: Plots (left side) of the estimated and true TACs of the myocardium from noise-free data with static data acquisition of the dilated myocardium in the case of 100% inclusion.

Figure 5- 16: Plots (right side) of the estimated and true TACs of the blood pool from noise-free data with static data acquisition of the dilated blood pool in the case of 100% inclusion.

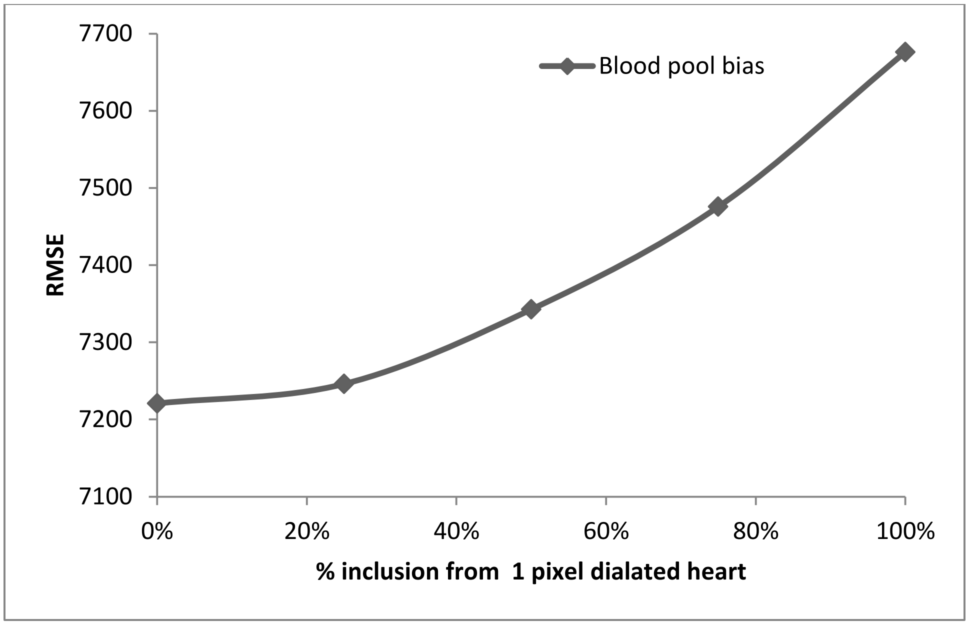

Figure 5- 17: Plots of the RMSE of the blood over all time points with static data acquisition at the optimal angle with varying dilated myocardium.

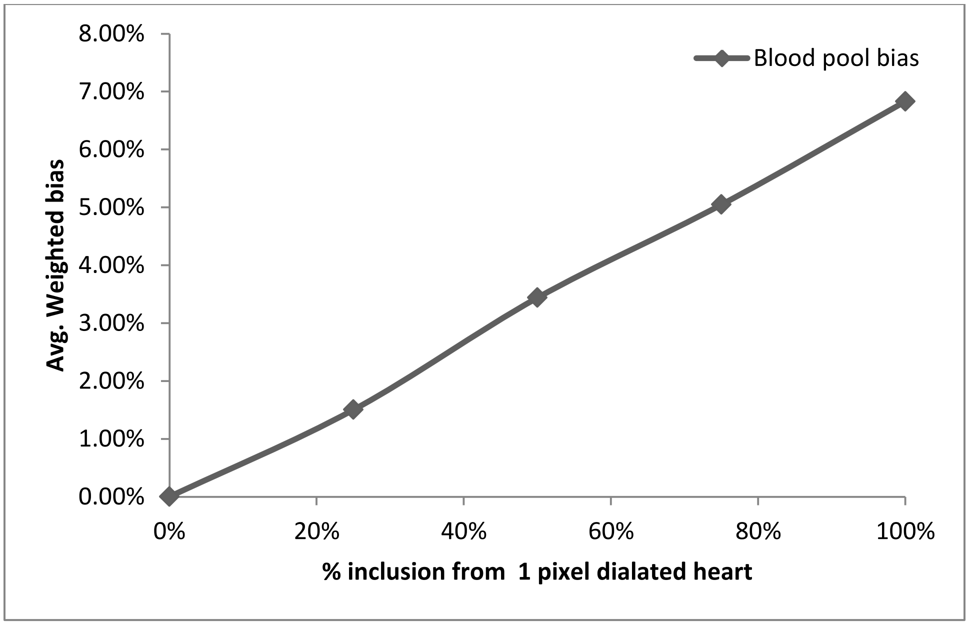

Figure 5- 18: Plots of average weighed bias of blood pool with static data acquisition at the optimal angle with varying dilated myocardium.

5.3.2 Estimation of global parameters

Tables 5-2 and -3 summarize k_{21} and k_{12} estimates of the myocardial VOI for noise-free cases using static data acquisition with RV VOI mismatch. We estimated the % bias of k_{21} to be <2%, k_{12} to be <76.4% and the myocardial blood flow (MBF) to <2%. Again, a large bias in k_{12} could be explained by failure to find the global minimum during parameter estimation. Table 5-2 summarizes the k_{21}, k_{12} and MBF estimates of the myocardial VOI for noise-free cases of RV VOI mismatch.

Table 5-2: Values of estimated noise-free kinetic parameters and MBF for the case of static data acquisition where the myocardial VOI used in estimation did not include the right ventricle.

Parameters	Gold	Estimated	% bias	Units
k_{21}	.5538	0.5437	1.8	ml/min/gm
k_{12}	.1265	0.2232	76.4	ml/min
MBF	.7162	.7036	1.7	ml/min/gm

Table 5-3 summarizes the k_{21} and k_{12} estimates of the myocardial VOI for the noise-free case using static data acquisition with Random Error DLV VOI model mismatch. Note that the % bias of k_{21} was <9% and k_{12} was <7 %.

Table 5- 3: Estimated noise-free kinetic parameter of static data acquisition with object model-mismatch where the dilated left ventricle of the myocardium VOI was included the right ventricle which was not accounted for in the model.

Parameters	Gold	Estimated	% bias	Units	% inclusion
k_{21}	.5538	.5538	0	ml/min/gm	0
K_{21}	.5538	.5435	1.8	ml/min/gm	25
k_{21}	.5538	.5307	4.1	ml/min/gm	50
K_{21}	.5538	.5204	6	ml/min/gm	75
k_{21}	.5538	.5093	8	ml/min/gm	100
k_{12}	.1265	.1266	0	ml/min	0
K_{12}	.1265	.1248	1.3	ml/min	25
k_{12}	.1265	.1226	3	ml/min	50
K_{12}	.1265	.1207	4.5	ml/min	75
k_{12}	.1265	.1187	6.1	ml/min	100

5.4 Discussion

In the previous chapters we explored estimating activities in VOIs using a continuous rotation acquisition protocol when we had knowledge of the true VOI. We found that this approach was unsuccessful when object model mismatch was present in the form of the RV being included as part of the background VOI. In continuous rotation, angle dependent biases result in time-varying bias, resulting in poor estimates of the kinetic parameters.

In contrast, when true VOIs are not exactly known, static acquisition at an optimal angle resulted in lower biases, and reduced variation in bias over time. We thus used static acquisition at a single optimal angle to investigate the impact of other forms of model mismatch. For each of the 3 cases of object model mismatch studied, the TACs agreed well with the true TACs (average percent bias <1% for the myocardium and <23% for the blood pool). For the myocardium, the bias was consistently low at all-time points. One possible explanation of larger bias in the blood pool later time points can be attributed to enforcement of non-negativity of ML algorithm (113).

These results of this work indicate that the proposed method results in a good estimate of wash-in kinetic parameter (k_{21}) and the global myocardial blood flow (MBF). Global flow was estimated to a bias of less than 2%. The wash-out kinetic parameter (k_{12}) had a bias of 76% due to large bias in the blood pool activity during much of the wash-out phase. This was due to the fact that, with static acquisition, the blood pool was obstructed by the myocardium and the high activity in the myocardium resulted in errors that were substantial compared to the low activity in the blood pool. However, because our main goal is to estimate the global myocardial blood flow, bias in the wash-out parameter is not as important as estimating k_{21} (wash-in). One side benefit is that the acquisition time could be shortened since data from the wash-out phase is not as important (114).

Table 5-4, below, depicts the value of MBF for the investigated cases of model-mismatch. In the case of RV VOI mismatch, the TACs estimated using the static acquisition method were in excellent agreement with the true TACs (average percent bias <3% for the myocardium and <7% for the blood pool). The extracted kinetic parameters from estimated TACs showed excellent agreement with the true kinetic parameters in all cases. In the case of Random Error DLV mismatch, when myocardial VOI was dilated by 1 voxel (inclusion fraction of 100%), the global flow estimate (k_{21}) had a bias of 9%. The wash-out flow parameter (k_{12}) was estimated to <7% bias. The k_{21} estimate was worse due to the fast changing tracer at the uptake phase.

Table 5- 4: MBF values for various types of investigated model mismatch.

Parameters	Gold	Estimated	% bias	Units	% inclusion
k_{21}	.5538	.5538	0	ml/min/gm	0
K_{21}	.5538	.5435	1.8	ml/min/gm	25
k_{21}	.5538	.5307	4.1	ml/min/gm	50
K_{21}	.5538	.5204	6	ml/min/gm	75
k_{21}	.5538	.5093	8	ml/min/gm	100
k_{12}	.1265	.1266	0	ml/min	0
K_{12}	.1265	.1248	1.3	ml/min	25
k_{12}	.1265	.1226	3	ml/min	50
K_{12}	.1265	.1207	4.5	ml/min	75
k_{12}	.1265	.1187	6.1	ml/min	100
MBF truth	.7162	NA	0	ml/min/gm	NA
RV VOI mismatch	.7162	.7036	1.8	ml/min/gm	NA
Random Error DLV 0%	.7162	.7162	0	ml/min/gm	NA
Random Error DLV 25%	.7162	.7038	1.7	ml/min/gm	NA
Random Error DLV 50%	.7162	.6874	4.0	ml/min/gm	NA
Random Error DLV 75%	.7162	.6746	5.8	ml/min/gm	NA
Random Error DLV 100%	.7162	.66	7.7	ml/min/gm	NA

6.0 Conclusion

This chapter first summarizes the results of this work, and subsequently discusses its contributions to the field and future directions of research.

6.1 Summary of results

Single-Photon Emission Computed Tomography (SPECT) has been widely used to assess myocardial perfusion status and to provide diagnostic information regarding coronary artery disease (CAD) status. A SPECT system consists of one or more gamma cameras that are rotated around the patient. The cameras acquire planar (projection) images of the three dimensional (3D) distribution of a radioactively labeled perfusion agent at different projection views. Transaxial reconstructed images are formed using tomographic image reconstruction methods from these projections. However, assessing myocardial perfusion from static activity distribution provides limited information for diagnosis. We were able to show through simulation studies, using two commonly used tracers including Tc-99m teboroxime and ^{201}Tl, that dynamic SPECT is feasible and provides quantitative information which may aid future diagnoses.

6.1.1 Feasibility study of estimation of dynamic time activity curve

In Chapter 3, we presented a new approach for estimating time-activity curves for the myocardium and blood pool, which are requisites for the kinetic analysis that is needed to calculate myocardial flow. The method is based on planar projections obtained from orthogonal projections that are acquired by conventional gamma cameras with a perpendicular configuration, often referred to as cardiac- or L-mode. The method uses 3D VOIs that could be obtained by segmenting static SPECT/CT acquisitions or registered contrast CT images, and it allows for realistic modeling of image-degrading effects, including scatter, attenuation, and the collimator-detector response and uses a maximum-likelihood estimation procedure. In a simulation study modeling the kinetics of Tc-99m teboroxime [104], we showed that it was possible to obtain good estimates of the myocardial (average weighted absolute bias of ~5%) and blood pool (average weighted absolute bias of ~10%) TACs when the true organ VOIs were known and the activity distributions in the organs were uniform, i.e., there was no object model mismatch. In the presence of unknown perfusion defects, the myocardial TAC was still estimated with good accuracy (average weighted absolute bias <10%) as long as the total reduction in myocardial activity was ≤5%. This indicates that the method is robust against modest model mismatch. In the case of larger defects where the defect VOI was included in the estimation procedure, the estimated normal myocardial and defect TACs were accurate (average weighted absolute bias ~ 5% for a defect with 25% extent and 100% severity). These data suggest that this is a promising method for obtaining dynamic information about the myocardium from relatively slow SPECT scans without the use of 4D dynamic SPECT reconstruction methods.

6.1.2 Estimation and evaluation of global kinetic parameters

In Chapter 4, we investigated the use of the method with ^{201}Tl, a commercially available tracer, and evaluated the method in terms of the accuracy and precision of the estimated myocardial and blood pool TACs, which are necessary inputs for estimation of the myocardial blood flow. We also studied the accuracy and precision of kinetic parameters estimated from these TACs. In the simulation, which used a continuous rotation acquisition protocol, we first showed that it was possible to obtain good estimates of the myocardial (average weighted absolute bias of ~1%) and blood pool (average weighted absolute bias of ~1%) TACs when the true organ VOIs were known and the activity distributions in the organ were uniform. The maximum percent biases at any time point for heart and blood were 2.8% and 1.3%, respectively. We extended the simulation study to show that estimates of k_{21} (wash-in), which is directly correlated to blood flow, had a bias of <5%. However, the results were obtained for the ideal case of no object model mismatch.

6.1.3 Effects of model mismatch

In Chapter 5 we examined the effects of object model mismatch, including structures, such as the right ventricle, that cannot easily be seen in the SPECT images and the presence of VOIs with non-uniform activity distributions, on kinetic estimations. We verified that these kinds of mismatch had an impact on accuracy that depended on the projection view. We found that continuous rotation acquisition gave poor estimates of kinetic parameters due to large and angular-dependent biases in the blood pool TAC estimates.

Based on the above observation, we investigated the pairs of projection views that gave the TACs with the smallest mean square error (MSE). Doing this using QPlanar would require estimating TACs for a large ensemble of noisy projection data, which was computationally challenging. We thus used Singular value decomposition (SVD) analysis to estimate directly the bias and variances at each time point. Using this SVD analysis, we found the pair of orthogonal projection views that gave the minimum MSE.

We thus investigated the use of static acquisition (i.e., acquisition without rotating the cameras) using the optimal projection views determined above. We showed that this static acquisition protocol gave good estimates of the myocardial (average weighted absolute bias of <5%) and blood pool (average weighted absolute bias of <5%) TACs, even when there were errors in specifying the organ VOIs. The value of k_{21} (wash-in) estimated from these TACs had a bias of <5% even in the presence of the 3 types of object model mismatch investigated.

6.2 Summary of technical and methodological contributions

This dissertation produced a number of results and methods that could have a significant clinical impact on myocardial perfusion imaging. In addition, the research presented in this dissertation makes a number of technical innovations that are summarized below. First, we demonstrated the feasibility of estimating organ or VOI activities from a single pair of projection views that are obtained simultaneously using a dual-camera system with the cameras in cardiac acquisition mode (i.e., with the cameras at right angles to each other in a perpendicular orientation). This method uses knowledge of the full 3D shape of the VOIs, an accurate model of the image formation process, and maximum-likelihood estimation techniques, allowing exact modeling of overlap of organs and compensation for physical image degrading factors.

In this method, we used a conventional slow-rotation SPECT/CT acquisition protocols; the requisite 3D VOIs could be estimated from conventional SPECT reconstructions or CT images. In principle, data could be acquired for all or part of the acquisition without rotation, and we determined that there was some advantage to acquiring data at a single pair of projection views in the case where there was mismatch between the true organ VOIs and the VOIs used in the estimation procedure. One advantage of rotating throughout the acquisition is that the data could also be used for 4D reconstruction, with the TACs estimated by this method serving as initial estimates. The QPlanar method also allows estimation of regional (e.g., of normal and ischemic myocardial) TACs that could be used as inputs to estimate kinetic parameters of physiological interest, such as blood flow.

The method does not require extremely fast camera rotation in order to obtain good time resolution, as the time resolution is equal to the acquisition time at each projection. Although this method does require modeling of the physics of the image detection system, the system matrix itself is very small. In particular, for each time point the projection matrix is has a size that is two times the number of projection bins by the number of VOIs, which would typically be less than ten. Computing this matrix, which includes models for attenuation, scatter, and the collimator-detector response, takes less than two seconds on current computers. Since the matrix is small, it can be stored in memory and the remainder of the calculations are extremely fast. The total time for estimating a typical TAC in this work was less than three minutes. Furthermore, because the operations at each time point are completely independent, the TAC estimation can be trivially parallelized, further reducing the computation time by a factor equal to the number of processor cores available.

We further demonstrated that the proposed QPlanar method is applicable even when there are unknown perfusion defects present. We applied the QPlanar method to cases where the activity distribution in the myocardial VOI was perturbed by perfusion defects with various extents and severities that were introduced into the left ventricular myocardium. In all cases, the activity concentration inside the perfusion defect was assumed constant. We investigated two scenarios. In the first scenario, it was assumed that the perfusion defect, though present in the data, was not known in the QPlanar process. In other words, a single myocardial VOI was used during QPlanar estimation with the assumption of uniform activity in the entire myocardial VOI.

In the second scenario, we assumed that the boundaries of the perfusion defect were known, and that the defect was treated as an additional VOI whose activity was estimated. This scenario modeled the case where the defect was large enough that it could be detected in conventional myocardial perfusion SPECT images and thus could be treated as a separate VOI in TAC estimation.

Our method lends itself to studying myocardial uptake in the presence of perfusion defect by treating the whole heart having uniform activity in one case and non-uniform activity in the leading to model mismatch in the other case. Our method demonstrates that we can perform an un-biased, noise free estimation of myocardium and blood pool TACs with either uniform or non-uniform perfusion defect.

Another important contribution of this work was to show that there are optimal projection views for the estimation of myocardial and blood pool TACS. The optimal angle was determined by finding the pair of orthogonal projection views that gave the minimum mean square error in the TACs. We then estimated kinetic parameters directly from the estimated time activity curve. Given an appropriate tracer, the activity values measured in a ROI is greatly influenced by the physiological characteristic of interest such as blood flow and receptor concentration. Therefore, an appropriate kinetic model can account for all the biological factors that contribute to the tissue radioactivity. The concentration of radioactivity in a given tissue region at a particular time primarily depends upon two factors; the local tissue physiology and the blood flow or metabolism in that region. We were able to demonstrate a two-compartment model that reliably predicts the global kinetic parameters in both noise-free and noisy cases.

6.3 Future work

While this work has proposed and demonstrated the feasibility of a new method for extracting flow information from myocardial perfusion imaging, there is substantial work left. In particular, the method can be improved by additional optimization of the acquisition protocol, including the acquisition duration per view and number of rotations. A second are requiring investigation is methods to obtain the required myocardial and blood pool VOIs. Further investigation of the effects of imperfect VOI definition and the bias and variance properties of kinetic parameters estimated from the TACs is needed. For some applications, it would be useful to obtain regional flow data. While we only examined the myocardium and an optimal defect region, the method could, in principle, be extended to multiple regions such as those corresponding to vascular territories. A final important area requiring future research is myocardial and patient motion on the accuracy of TACs and kinetic parameters.

In our current research we provided an estimate of the global blood flow in the heart. An important future goal is to analyze regional blood flow in different parts of the myocardium, i.e. regions corresponding to vascular territories. However, this would require the identification of regional sites in SPECT images, which remains a challenging task given the current spatial resolution of the SPECT system. Methods for defining these territories and the impact of errors in these territory definitions are needed.

Our robust estimation method could also be applied to evaluating a patient with unknown cardiac condition such as non-uniform uptake in the myocardium. In this case, defect VOIs would be estimated from conventional MPS studies performed after the acquisition of the dynamic data.

Thorough validation is essential prior to implementing the proposed method clinically. In this work we demonstrated the feasibility using simulation studies. The next steps include validation using phantom and by animal studies. Finally, a human study, with flow values compared to Ammonia PET, a gold standard for quantitative cardiac perfusion imaging would be needed to validate the method.

7. Table of Abbreviation

LV = Left Ventricle
RV = Right Ventricle
MBF = Myocardial Blood Flow
MPS=Myocardial Perfusion SPECT
QPlanar = Quantitative Planner
VOI = Volume of interest
ROI = Region of interest
ABS = Absolute
NA= Not Applicable
DLV = Dilated Left Ventricle
IF = inclusion fraction
PET=Positron Emission Tomography

8.0 References

1. Uren, N.G., et al., *Relation between Myocardial Blood-Flow and the Severity of Coronary-Artery Stenosis.* New England Journal of Medicine, 1994. **330**(25): p. 1782-1788.
2. Camici PG, C.F., *Coronary microvascular dysfunction.* N Engl. J. Med. 2007, 2007. **356**: p. 830-840.
3. De Silva R, C.P., *Role of positron emission tomography in the investigation of human coronary circulatory function.* Cardiovasc Res, 1994. **28:**: p. 1595-612.
4. Renaud, J.M., et al., *Quantification of the normal range of myocardial blood flow and flow reserve with (82)rubidium versus N-13-ammonia PET.* 2007 Ieee Nuclear Science Symposium Conference Record, Vols 1-11, 2007: p. 3141-3145.
5. Lortie, M., et al., *Quantification of myocardial blood flow with 82Rb dynamic PET imaging.* Eur J Nucl Med Mol Imaging, 2007. **34**(11): p. 1765-74.
6. Kailasnath, P. and A.J. Sinusas, *Technetium-99m-labeled myocardial perfusion agents: Are they better than thallium-201?* Cardiol Rev, 2001. **9**(3): p. 160-72.
7. Chiao, P.C., et al., *Compartmental Analysis of Technetium-99m-Teboroxime Kinetics Employing Fast Dynamic Spect at Rest and Stress.* Journal of Nuclear Medicine, 1994. **35**(8): p. 1265-1273.
8. Farncombe, T., et al., *Dynamic SPECT imaging using a single camera rotation (dSPECT).* Ieee Transactions on Nuclear Science, 1999. **46**(4): p. 1055-1061.
9. Smith, A.M. and G.T. Gullberg, *Dynamic Cardiac Spect Computer-Simulations for Teboroxime Kinetics.* Ieee Transactions on Nuclear Science, 1994. **41**(4): p. 1626-1633.
10. Gullberg, G.T., et al., *Dynamic single photon emission computed tomography--basic principles and cardiac applications.* Physics in Medicine and Biology, 2010. **55**(20): p. R111-91.
11. Winant, C.D., et al., *Analysis of Dynamic SPECT/CT Measurements of the Arterial Input Function in Human Subjects.* 2009 Ieee Nuclear Science Symposium Conference Record, Vols 1-5, 2009: p. 3404-3408.
12. Sitek, A., et al., *Removal of liver activity contamination in teboroxime dynamic cardiac SPECT imaging with the use of factor analysis.* Journal of Nuclear Cardiology, 2002. **9**(2): p. 197-205.
13. Farncombe, T., et al., *The incorporation of organ uptake into dynamic SPECT (dSPECT) image reconstruction.* Ieee Transactions on Nuclear Science, 2001. **48**(1): p. 3-9.
14. Humphries, T., A. Celler, and M. Trummer, *Slow-rotation dynamic SPECT with a temporal second derivative constraint.* Med Phys, 2011. **38**(8): p. 4489-97.
15. Zan, Y., et al., *Fast direct estimation of the blood input function and myocardial time activity curve from dynamic SPECT projections via reduction in spatial and temporal dimensions.* Med Phys, 2013. **40**(9): p. 092503.
16. Madsen, M.T., *Recent advances in SPECT imaging.* Journal of Nuclear Medicine, 2007. **48**(4): p. 661-673.
17. Roger VL, L.-J.D., *Heart disease and stroke statistics - 2011 update: a report from the American Heart Association.* Circulation 2011. **123**: p. 933-44.

18. Mozaffarian, D., *Heart disease and stroke statistics—2015 update: a report from the American Heart Association. .* Circulation, 2015(131).
19. Gould, K.L. and K. Lipscomb, *Effects of Coronary Stenoses on Coronary Flow Reserve and Resistance.* American Journal of Cardiology, 1974. **34**(1): p. 48-55.

20. Yoshinaga, K., et al., *Reduction of coronary flow reserve in the area without ischemia on stress perfusion SPECT in patients with coronary artery disease.* Journal of Nuclear Medicine, 2003. **44**(5): p. 90p-90p.
21. Yoshinaga, K., et al., *Reduction of coronary flow reserve in the area with and without ischemia on stress perfusion spect in patients with coronary artery disease.* Journal of Nuclear Medicine, 2001. **42**(5): p. 179p-179p.
22. Heller, L.I., et al., *Intracoronary Doppler assessment of moderate coronary artery disease - Comparison with Tl-201 imaging and coronary angiography.* Circulation, 1997. **96**(2): p. 484-490.
23. Gullberg, G.T., E.V.R. Di Bella, and A.J. Sinusas, *Estimation of coronary flow reserve: Can SPECT compete with other modalities?* Journal of Nuclear Cardiology, 2001. **8**(5): p. 620-625.
24. Jaarsma, C., et al., *Diagnostic Performance of Noninvasive Myocardial Perfusion Imaging Using Single-Photon Emission Computed Tomography, Cardiac Magnetic Resonance, and Positron Emission Tomography Imaging for the Detection of Obstructive Coronary Artery Disease A Meta-Analysis.* Journal of the American College of Cardiology, 2012. **59**(19): p. 1719-1728.
25. Patterson, R.E., R.L. Eisner, and S.F. Horowitz, *Comparison of Cost-Effectiveness and Utility of Exercise Ecg, Single-Photon Emission Computed-Tomography, Positron Emission Tomography, and Coronary Angiography for Diagnosis of Coronary-Artery Disease.* Circulation, 1995. **91**(1): p. 54-65.
26. Khare, H.S., et al., *Comparison of Static and Dynamic Cardiac Perfusion Thallium-201 SPECT.* IEEE Trans Nucl Sci, 2001. **48**(3): p. 774.
27. Smith, A.M., et al., *Kinetic modeling of teboroxime using dynamic SPECT imaging of a canine model.* Journal of Nuclear Medicine, 1994. **35**(3): p. 484-95.
28. Zierler, K.L., *Equations for Measuring Blood Flow by External Monitoring of Radioisotopes.* Circ Res, 1965. **16**: p. 309-21.
29. DiStefano, J.J., 3rd, *Noncompartmental vs. compartmental analysis: some bases for choice.* Am J Physiol, 1982. **243**(1): p. R1-6.
30. Carson, R., *Tracer Kinetic Modeling in PET*, in *Positron Emission Tomography Basic Sciences*2003, Springer. p. 127-160.
31. Kety, S.S., *The theory and applications of the exchange of inert gas at the lungs and tissues.* Pharmacol Rev, 1951. **3**(1): p. 1-41.
32. Renkin, E.M., *Transport of potassium-42 from blood to tissue in isolated mammalian skeletal muscles.* Am J Physiol, 1959. **197**: p. 1205-10.
33. Crone, C., *"Permeability of capillaries in various organs as determined by use of the indicator diffusion method.* Acta Physiol Scand, 1964. **58**: p. 292-305.
34. Huesman, R.H., *A New Fast Algorithm for the Evaluation of Regions of Interest and Statistical Uncertainty in Computed-Tomography.* Journal of Nuclear Medicine, 1984. **25**(5): p. P89-P89.
35. Hughes, G.H., T., *Least-squares fitting of complex functions*, in *Measurements and their uncertainties A practical guide to modern error analysis*2010, Oxford Univ. press. p. 69-80.
36. Marquardt, D., *An algorithm for least-squares estimation of nonlinear parameters.* SIAM journal applied math, 1963. **11**: p. 431-441.
37. Levenberg, K., *A method for the solution of certain problems in least-squares.* Quarterly Applied Math, 1944. **2**: p. 164-168.

38. Berman, D.S., et al., *SPECT/PET myocardial perfusion imaging versus coronary CT angiography in patients with known or suspected CAD.* Q J Nucl Med Mol Imaging, 2010. **54**(2): p. 177-200.
39. Cherry R. S., S., JA, Phelps, ME., *Physics in Nulcear Medicine.*, 2003, Oxford, England: W. B. Saunders Company.
40. Frey, E., Tsui, BM, Zaidi H, , *Collimator detector response compensation in SPECT.* Quantitative Analysis in Nuclear Medicine Imaging,New York, NY: Springer., 2006.
41. Sorenson, J., *Quantitative measurement of radioactivity in vivo by whole-body counting.* Instrumentation of Nuclear Medicine, 1974. **2**: p. 311-348.
42. Jaszczak, R.J., et al., *Improved Spect Quantification Using Compensation for Scattered Photons.* Journal of Nuclear Medicine, 1984. **25**(8): p. 893-900.
43. King, M.A., G.J. Hademenos, and S.J. Glick, *A dual-photopeak window method for scatter correction.* Journal of Nuclear Medicine, 1992. **33**(4): p. 605-12.
44. Vanreenen, O., et al., *Quantification of the Distribution of in-111-Labeled Platelets in Organs.* European Journal of Nuclear Medicine, 1982. **7**(2): p. 80-84.
45. Sjogreen, K., M. Ljungberg, and S.E. Strand, *An activity quantification method based on registration of CT and whole-body scintillation camera images, with application to I-131.* Journal of Nuclear Medicine, 2002. **43**(7): p. 972-982.
46. Tang, H.R., et al., *Implementation of a combined X-ray CT-scintillation camera imaging system for localizing and measuring radionuclide uptake: Experiments in phantoms and patients.* Ieee Transactions on Nuclear Science, 1999. **46**(3): p. 551-557.
47. He, B. and E.C. Frey, *Comparison of conventional, model-based quantitative planar, and quantitative SPECT image processing methods for organ activity estimation using In-111 agents.* Physics in Medicine and Biology, 2006. **51**(16): p. 3967-3981.
48. He, B. and E.C. Frey, *Effects of shortened acquisition time on accuracy and precision of quantitative estimates of organ activity.* Medical Physics, 2010. **37**(4): p. 1807-1815.
49. He, X., et al., *Comparison of 180 degrees and 360 degrees acquisition for myocardial perfusion SPECT with compensation for attenuation, detector response, and scatter: Monte Carlo and mathematical observer results.* Journal of Nuclear Cardiology, 2006. **13**(3): p. 345-53.
50. Carson, R., *A maximum likelihood method for region-of-intcrest evaluation in emission tomography.* J Comput Assist Tomogr, 1986. **4**: p. 654-663.
51. Bal, G., et al., *Analytical reconstruction for multi-segment slant hole SPECT.* 2002 Ieee Nuclear Science Symposium, Conference Record, Vols 1-3, 2003: p. 1236-1240.
52. Gordan R, *A tutorial on algebriac reconsruction techniques.* IEEE Trans Nucl Sci, 1974. **21**: p. 78-93.
53. Hudson H. M, L.R.S., *Accelerated image reconstruction using ordered subsets of projection data.* IEEE Trans Med Imaging, 1994. **13**: p. 601-609.
54. Shepp L.A., V.Y., *Maximum likelihood reconstruction for emission tomography.* IEEE Trans Med Imaging, vol. 1, pp. 113-122, 1982, 1982. **1**: p. 113-122.
55. Bellini, S., et al., *Compensation of Tissue Absorption in Emission Tomography.* Ieee Transactions on Acoustics Speech and Signal Processing, 1979. **27**(3): p. 213-218.
56. Chang, L.T., *Method for Attenuation Correction in Radionuclide Computed Tomography.* Ieee Transactions on Nuclear Science, 1978. **25**(1): p. 638-643.
57. Gullberg, G.T. and T.F. Budinger, *The Use of Filtering Methods to Compensate for Constant Attenuation in Single-Photon Emission Computed-Tomography.* Ieee Transactions on Biomedical Engineering, 1981. **28**(2): p. 142-157.

58. Inouye, T., K. Kose, and A. Hasegawa, *Image-Reconstruction Algorithm for Single-Photon-Emission Computed-Tomography with Uniform Attenuation.* Physics in Medicine and Biology, 1989. **34**(3): p. 299-304.
59. Glick, S.J., et al., *An analytical approach for compensation of non-uniform attenuation in cardiac SPECT imaging.* 1995 Ieee Nuclear Science Symposium and Medical Imaging Conference Record, Vols 1-3, 1996: p. 1713-1717.
60. Kunyansky, L.A., *A new SPECT reconstruction algorithm based on the Novikov explicit inversion formula.* Inverse Problems, 2001. **17**(2): p. 293-306.
61. Natterer, P., *Inversion of the attenuated Radon transform.* Inverse Problems, 2001. **17**(1): p. 113-119.
62. Novikov, R.G., *An inversion formula for the attenuated X-ray transformation.* Arkiv for Matematik, 2002. **40**(1): p. 145-167.
63. Censor, Y., et al., *New Approach to the Emission Computerized Tomography Problem - Simultaneous Calculation of Attenuation and Activity-Coefficients.* Ieee Transactions on Nuclear Science, 1979. **26**(2): p. 2775-2779.
64. Bocher, M., et al., *Gamma camera-mounted anatomical X-ray tomography: technology, system characteristics and first images.* European Journal of Nuclear Medicine, 2000. **27**(6): p. 619-627.
65. Patton, J.A., D. Delbeke, and M.P. Sandler, *Image fusion using an integrated, dual-head coincidence camera with x-ray tube-based attenuation maps.* Journal of Nuclear Medicine, 2000. **41**(8): p. 1364-1368.
66. Floyd, C.E., et al., *Deconvolution of Compton Scatter in Spect.* Journal of Nuclear Medicine, 1985. **26**(4): p. 403-408.
67. Gilland, D.R., et al., *Determination of the Optimum Filter Function for Spect Imaging.* Journal of Nuclear Medicine, 1988. **29**(5): p. 643-650.
68. Yanch, J.C., M.A. Flower, and S. Webb, *A Comparison of Deconvolution and Windowed Subtraction Techniques for Scatter Compensation in Spect.* Ieee Transactions on Medical Imaging, 1988. **7**(1): p. 13-20.
69. Msaki, P., B. Axelsson, and S.A. Larsson, *Some Physical Factors Influencing the Accuracy of Convolution Scatter Correction in Spect.* Physics in Medicine and Biology, 1989. **34**(3): p. 283-298.
70. King, M.A., B.C. Penney, and S.J. Glick, *An Image-Dependent Metz Filter for Nuclear-Medicine Images.* Journal of Nuclear Medicine, 1988. **29**(12): p. 1980-1989.
71. Riauka, T.A. and Z.W. Gortel, *Photon Propagation and Detection in Single-Photon Emission Computed-Tomography - an Analytical Approach.* Medical Physics, 1994. **21**(8): p. 1311-1321.
72. Cao, Z.J., E.C. Frey, and B.M.W. Tsui, *A Scatter Model for Parallel and Converging Beam Spect Based on the Klein-Nishina Formula.* Ieee Transactions on Nuclear Science, 1994. **41**(4): p. 1594-1600.
73. Beekman, F.J., H.W.A.M. de Jong, and S. van Geloven, *Efficient fully 3-D iterative SPECT reconstruction with Monte Carlo-based scatter compensation.* Ieee Transactions on Medical Imaging, 2002. **21**(8): p. 867-877.
74. Floyd, C.E., et al., *Inverse Monte-Carlo as a Unified Reconstruction Algorithm for Ect.* Journal of Nuclear Medicine, 1986. **27**(10): p. 1577-1585.
75. Frey, E.C. and B.M.W. Tsui, *A Practical Method for Incorporating Scatter in a Projector-Backprojector for Accurate Scatter Compensation in Spect.* Ieee Transactions on Nuclear Science, 1993. **40**(4): p. 1107-1116.

76. Frey, E.C. and B.M.W. Tsui, *A new method for modeling the spatially-variant, object-dependent scatter response function in SPECT.* 1996 Ieee Nuclear Science Symposium - Conference Record, Vols 1-3, 1997: p. 1082-1086.
77. Jonsson, C. and S.A. Larsson, *A spatially varying Compton scatter correction for SPECT utilizing the integral Klein-Nishina cross section.* Physics in Medicine and Biology, 2001. **46**(7): p. 1767-1783.
78. Riauka, T.A., H.R. Hooper, and Z.W. Gortel, *Experimental and numerical investigation of the 3D SPECT photon detection kernel for non-uniform attenuating media.* Physics in Medicine and Biology, 1996. **41**(7): p. 1167-1189.
79. Watson, C.C., et al., *Evaluation of simulation-based scatter correction for 3D PET cardiac imaging.* 1995 Ieee Nuclear Science Symposium and Medical Imaging Conference Record, Vols 1-3, 1996: p. 1373-1377.
80. Yanch, J.C., M.A. Flower, and S. Webb, *Improved quantification of radionuclide uptake using deconvolution and windowed subtraction techniques for scatter compensation in single photon emission computed tomography.* Medical Physics, 1990. **17**(6): p. 1011-22.
81. Tsui, B.M., et al., *The importance and implementation of accurate 3D compensation methods for quantitative SPECT.* Physics in Medicine and Biology, 1994. **39**(3): p. 509-30.
82. Song, X., et al., *Fast modelling of the collimator-detector response in Monte Carlo simulation of SPECT imaging using the angular response function.* Physics in Medicine and Biology, 2005. **50**(8): p. 1791-804.
83. Hoffman, E.J., S.C. Huang, and M.E. Phelps, *Quantitation in positron emission computed tomography: 1. Effect of object size.* J Comput Assist Tomogr, 1979. **3**(3): p. 299-308.
84. Mazziotta, J.C., et al., *Quantitation in positron emission computed tomography: 5. Physical--anatomical effects.* J Comput Assist Tomogr, 1981. **5**(5): p. 734-43.
85. Rousset, O.G., Y. Ma, and A.C. Evans, *Correction for partial volume effects in PET: principle and validation.* Journal of Nuclear Medicine, 1998. **39**(5): p. 904-11.
86. Da Silva, A., Tang, HR, Wong, KH, Wu, MC, Dae, MW, Hasegawa, BH., *Absolute quantification of regional myocardial uptake of Tc-99m-Sestamibi with SPECT: Experimental validation in a porcine model.* Journal of Nuclear Medicine, 2001. **42**: p. 772-779.
87. Du, Y., He, B, Frey, EC., *Iterative Reconstruction of Combined Voxelized Images and Volume-of-Interest for Quantitative SPECT Imaging.* Transactions on Medical Imaging, IEEE 2010.
88. Tsui, B., Hu, HB, Gilland, DR, Gullberg, GT., *Implementation of Simultaneous Attenuation and Detector Response Correction in Spect.* Ieee Transactions on Nuclear Science, 1988. **35**: p. 778-783.
89. Zeng, G., Gullberg, GT, Bai, CY, et al., *Iterative reconstruction of fluorine-18 SPECT using geometric point response correction.* 1998. **39**: p. 124-130.
90. Lim, C.B., et al., *Triangular Spect System for 3-D Total Organ Volume Imaging - Performance Results and Dynamic Imaging Capability.* Ieee Transactions on Nuclear Science, 1986. **33**(1): p. 501-504.
91. Nakajima, K., et al., *[A three-headed SPECT system with high resolution and high sensitivity: application to myocardial imaging].* Kaku Igaku, 1990. **27**(5): p. 493-7.
92. Iida, H. and S. Eberl, *Quantitative assessment of regional myocardial blood flow with thallium-201 and SPECT.* Journal of Nuclear Cardiology, 1998. **5**(3): p. 313-31.
93. Di Bella, E.V., et al., *Compartmental modeling of technetium-99m-labeled teboroxime with dynamic single-photon emission computed tomography: comparison with static thallium-201 in a canine model.* Invest Radiol, 2001. **36**(3): p. 178-85.

94. Segars, W.T., BM; Lalush, DS; Frey, EC; King, MA; Manocha, D., *Development and appkication of the new dynamic Nurbs-based Cardiac-Torso (NCAT) phantom.* Journal of Nuclear Medicine, 2001. **42**.
95. Frey, E.C. and B.M.W. Tsui, *An investigation of combined attenuation and scatter compensation for Tl-201 cardiac SPECT.* Journal of Nuclear Medicine, 1996. **37**(5): p. 111-111.
96. Frey, E.C., Z.W. Ju, and B.M.W. Tsui, *A Fast Projector-Backprojector Pair Modeling the Asymmetric, Spatially Varying Scatter Response Function for Scatter Compensation in Spect Imaging.* IEEE Transactions on Nuclear Science, 1993. **40**(4): p. 1192-1197.
97. Kadrmas, D.J., E.C. Frey, and B.M. Tsui, *An SVD Investigation of Modeling Scatter in Multiple Energy Windows for Improved SPECT Images.* IEEE Trans Nucl Sci, 1996. **43**(3): p. 2275-2284.
98. Song, N., et al., *EQPlanar: a maximum-likelihood method for accurate organ activity estimation from whole body planar projections.* Phys Med Biol, 2011. **56**(17): p. 5503-24.
99. He, B. and E.C. Frey, *The impact of 3D volume of interest definition on accuracy and precision of activity estimation in quantitative SPECT and planar processing methods.* Physics in Medicine and Biology, 2010. **55**(12): p. 3535-3544.
100. Dariush Mozaffarian, E.J.B., Alan S. Go, *Heart disease and stroke statistics-2016 update, a report from American Heart Association.* Circulation, 2016. **133**(4).
101. Iida, H., et al., *Absolute quantitation of myocardial blood flow with Tl-201 and dynamic SPECT in canine: optimisation and validation of kinetic modelling.* European Journal of Nuclear Medicine and Molecular Imaging, 2008. **35**(5): p. 896-905.
102. Carli, M.D., *Assessment of myocardial viability after myocardial infraction.* J Nucl Med, 2002. **36**: p. 2138-2147.
103. Sugihara, H., et al., *Estimation of coronary flow reserve with the use of dynamic planar and SPECT images of Tc-99m tetrofosmin.* Journal of Nuclear Cardiology, 2001. **8**(5): p. 575-579.
104. Hossain, J.Y., Du; Eric Frey *Investigation of the feasibility of dynamic cardiac imaging with a dual detector gamma camera (DDGC).* Journal of Nuclear Medicine, 2011. **52**.
105. Piwnica-Worms, D., *Divergent kinetics of Tl-201 and 99m-Tc-sestamibi in cultured chick ventricular myocytes during ATP depletion.* Circulation, 1992. **85**(1531-1534).
106. Song, N., et al., *EQPlanar: a maximum-likelihood method for accurate organ activity estimation from whole body planar projections.* Physics in Medicine and Biology, 2011. **56**(17): p. 5503-5524.
107. E. C. Frey, B.T., *A new method for modeling the spatially-variant, object-dependent scatter response function in SPECT.* IEEE Nucl. Sci. Symp., 1996: p. pp 1082–6.
108. Kadrmas, D.J., E.C. Frey, and B.M. Tsui, *Analysis of the reconstructibility and noise properties of scattered photons in 99mTc SPECT.* Physics in Medicine and Biology, 1997. **42**(12): p. 2493-516.
109. Myers, B.H.a.K.J., *Foundations o f Image Science*2004: John Wiley & Sons, Inc.
110. Rong, X., Y. Du, and E.C. Frey, *A method for energy window optimization for quantitative tasks that includes the effects of model-mismatch on bias: application to Y-90 bremsstrahlung SPECT imaging.* Physics in Medicine and Biology, 2012. **57**(12): p. 3711-25.
111. Xing, R., *Development and evaluation of quantitative Y-90 Bremsstrahlung SPECT methods* in *Electrical and Computer Eng.*2013, Johns Hopkins: Johns Hopkins.
112. Golub, G.H., Van Loan C.F., *Matrix Computation*. 3rd ed1996: Johns Hopkins Univ. Press.

113. Van Slambrouck, K., et al., *Bias reduction for low-statistics PET: maximum likelihood reconstruction with a modified Poisson distribution.* IEEE Trans Med Imaging, 2015. 34(1): p. 126-36.

114. Tang Jing, A.R., Riikka Lautamaki, Martin A Lodge, Frank M Bengel and Benjamin M W Tsui, *Optimization of Rb-82 PET acquisition and reconstruction protocols for myocardial perfusion defect detection.* Physics in Medicine and Biology, 2009. 54: p. 3161–3171.

9.0 CURRICULUM VITAE

Jakir was born on March 5th, in Chittagong, Bangladesh. He completed his Bachelors of Science degree Electrical Engineering from Morgan State University in United States. He then received a full time Masters of Science in Electrical Engineering from Whiting School of Engineering. He worked in Radar system design in Northrop Grumman corp. prior to starting Whiting School of Engineering and a Research Assistant appointment from the Division of Medical Imaging Physics, to start a Ph.D. in Electrical and Computer Engineering. He joined the Division of Medical imaging Physics under the supervision of Professor Eric Frey in September 2011. He received the degree of Doctor of Philosophy in Electrical and Computer Engineering in December 2017, with a dissertation focused on the whole-heart dynamics of blood-flow using perfusion tracers and a dual camera SPECT system.

Research patent: Breast compression device, **US Patent No. 8,380,281 B2**

Publications:

Conference Papers

SPECT:

1. **Jakir Hossain**, D. Yong, F. Eric; Johns Hopkins University, Baltimore, MD "Quantitative Estimation of Organ Time-Activity Curves from SPECT Data using a Two-Camera System", American Society of Nuclear Cardiology (ASNC), 2011.

2. **Jakir Hossain**, Yong Du, Na Song, Mickel Ghaly, George Fung, Eric Frey "Investigation of the feasibility of dynamic Cardiac Imaging with a dual detector Gamma Camera" Society of Nuclear Medicine (SNM), San Antonio, TX 20011

3. D. Lamba, M. Ghaly, P. Greene, **J. Hossain**, E.C. Frey "Efficient Estimation of Cardiac Time-Activity Curves from a Two-Camera SPECT System using Compressed Sensing with Projective Subspace Denoising" Hopkins Imaging Initiative conference, November, 2012

4. Zohreh Shahpouri, Ahmad Bitarafan-Rajabi, Alireza Kamali Asl, **Jakir Hossain**, Arman Rahmim, Seyed Mohammad Entezarmahdi, Samane Mohseni, Nahid Yaghoobi "Investigation of Accuracy of Dynamic Myocardial Perfusion 201-Thallium SPECT in comparison to Conventional Static Imaging", Iranian Congress of Nuclear Medicine, Shiraz, Iran, May 1-3, 2013

MRI:

1. **Jakir Hossain**, T.A. Yousef, Michael Jacobs, N.F. Osman, "Increasing Strain accuracy in Strain Encoded (SENC) imaging using Center-of-mass method" The International Society for Magnetic Resonance in Medicine (ISMRM), 2009

2. Ahmed A. Harouni, **Jakir Hossain**, Michael A. Jacobs, and Nael F. Osman. "Improving Spatial Resolution of Strain-Encoded (SENC) Magnetic Resonance Elastography (MRE) for Enhancing Stiff-Mass Detection". ISMRM, 2010.

3. Ahmed A. Harouni, Riham H. El Khouli, **Jakir Hossain**, David A. Bluemke, Nael Osman, and Michael A. Jacobs, "Enhancing Mass Detection and Classification In Breast Tissue Using Strain-Encoded (SENC) MRI". E-poster, Montreal, Quebec, Canada 2011.

Peer Reviewed Journal papers:

SPECT:

1. **Jakir Hossain**, Yong Du, and Eric Frey. "Estimation of dynamic time activity curves from dynamic cardiac SPECT imaging". Physics of Medicine and Biology, (accepted March, 2015)

2. Zohreh Shahpouri, Alireza Kamali-Asl, Ahmad Bitarafan-Rajabi, **Jakir Hossain**, Seyed Mohammad Entezarmahdi, Samane Mohseni, Nahid Yaghoobi, Arman Rahmim "A Comparative Assessment of "Dynamic and Conventional Thallium-201 SPECT Myocardial Perfusion Imaging: Monte Carlo Simulations and Case Studies", Frontiers in Biomedical technologies, Accepted March 06, 2013

MRI:

1. Ahmed A. Harouni, **Jakir Hossain**, Michael A. Jacobs, and Nael F. Osman. "Improved Spatial Resolution for imaging stiffness using Strain-Encoded (SENC) MRI ". Accepted, Academic radiology 2011.

2. Ahmed A. Harouni, **Jakir Hossain**, Riham H. El Khouli, David A. Bluemke, Nael F. Osman, and Michael A. Jacobs, "Enhancing Mass Detection and Classification In Breast Tissue Using Strain-Encoded (SENC) MRI". June 2012 (accepted)